DDC

JUN 26 1963

TISIA D

RESEARCH INC.

SANTA BARBARA, CALIFORNIA

THE DYNAMICS AND AERODYNAMICS

OF SELF-SUSTAINED

LARGE ANGLE OF ATTACK

BODY SPINNING MOTIONS

by

James E. Brunk

Final Report
Contract No. AF 49(638)-1158
Project No. 7856
Task No. 7856-01

Prepared for

Air Force Office of Scientific Research
Office of Aerospace Research
United States Air Force

ALPHA RESEARCH, INC.
SANTA BARBARA, CALIFORNIA

Subcontractor to
Electronic Communications, Inc.

February 1963

FOREWARD

This report was prepared under Air Force contract AF 49 (638) - 1158, by Alpha Research, Inc. under sub-contract AD - 1001 with Electronic Communications, Inc. The contract was monitored by the Air Force Office of Scientific Research. The contract monitors were Dr. Harald A. Melkus and Major B. R. Agins.

The principal investigator for this contract was Mr. James E. Brunk. Computer program modifications and error analyses were accomplished by Mr. Joe Nolley.

Numerical integration of the equations of motion was accomplished on the UNIVAC 1103A digital computer located at the Air Force Missile Development Center, Holloman Air Force Base. The cooperation of Mrs. Elizabeth Lee, AFMDC, in obtaining the computer solutions was particularly helpful.

ABSTRACT

Several aerodynamic mechanisms, which will sustain large angle of attack body autorotative motions, are examined. It is shown that autorotative motion can result in a very large drag force, which may significantly aid missile and booster recovery.

A linear theory, which satisfactorily predicts the near-steady-state autorotative spin characteristics of quasi-axi-symmetric bodies, is presented. The initiation of body autorotative motions under both low altitude and re-entry environments is investigated by a special six-degrees-of-freedom trajectory program.

The aerodynamic characteristics of cylinder-shaped bodies at angles of attack near ninety degrees are discussed.

TABLE OF CONTENTS

LIST OF TABLES

LIST OF ILLUSTRATIONS

x

C_{DC}	cylinder section drag coefficient
$C_{N\vec{a}_0}$, $C_{N\vec{a}_2}$, $C_{N\vec{a}_4}$	derivative of complex normal force with respect to $\vec{a}$, $\vec{a}^3$, and $\vec{a}^5$, respectively
$C_{M\vec{a}_0}$, $C_{M\vec{a}_2}$, $C_{M\vec{a}_4}$	derivative of complex pitching moment with respect to $\vec{a}$, $\vec{a}^3$, and $\vec{a}^5$, respectively
$C_{N_p\vec{a}_0}$, $C_{N_p\vec{a}_2}$, $C_{N_p\vec{a}_4}$	derivative of Magnus force with respect to $pd/2V$ and $\vec{a}$, $\vec{a}^3$, and $\vec{a}^5$, respectively
$C_{M_p\vec{a}_0}$, $C_{M_p\vec{a}_2}$, $C_{M_p\vec{a}_4}$	derivative of Magnus moment with respect to $pd/2V$ and $\vec{a}$, $\vec{a}^3$, and $\vec{a}^5$, respectively
$C_{N_p} = \dfrac{\text{Magnus force}}{q\,s\,d\,(pd/2V)}$	Magnus force coefficient
$C_{F_p\pi/2}$	section Magnus force coefficient at $\vec{a} = \pi/2$
$C_{n_{r_0}}$, $C_{n_{r_2}}$	derivative of yawing moment with respect to $rd/2V$ and $(rd/2V)^3$, respectively
C_{m_q}	derivative of pitching moment with respect to $qd/2V$
C_{x_0}, C_{x_2}	axial force coefficient for $\vec{a} =$ zero and derivative of axial force coefficient with respect to $\vec{a}^2$, respectively
$C_{M_{z_0}}$	yawing moment coefficient due to aerodynamic asymmetry
C_{M_r}	derivative of pitching moment with respect to $rd/2V$

$C_{M_{pr}}$	derivative of pitching moment with respect to pd/2V and rd/2V
$C_{M\pi/2}$	pitching moment coefficient at $\vec{\alpha} = \pi/2$
$C_{M_p\pi/2}$	Magnus moment derivative with respect to pd/2V evaluated at $\vec{\alpha} = \pi/2$
C_{ℓ_p}	derivative of rolling moment with respect to pd/2V
d	body diameter
F	aerodynamic force
g	acceleration due to gravity
$\vec{i}, \vec{j}, \vec{k}$	unit vectors
$I = I_y = I_z$	body transverse moment of inertia
I_x	body moment of inertia with respect to x-axis
k	body radius of gyration about axis of symmetry
K	body transverse radius of gyration
K	$\left(\dfrac{1}{2}\right)\left(\dfrac{\rho V^2 S d}{I}\right)$
ℓ	body length
ℓ_F	flap length
L	d/2V
m	body mass
M	Mach number, based on V
M	aerodynamic moment

p, q, r	body angular velocity components with respect to the x, y, z fixed-plane axes
p, $\widetilde{q}$, $\widetilde{r}$	body angular velocity components with respect to the $\widetilde{x}$, $\widetilde{y}$, $\widetilde{z}$ body-fixed axes
q	dynamic pressure, $1/2 \rho V^2$
R	Reynolds number, based on d and V
S	body reference area, $\pi d^2/4$, unless otherwise noted
u, v, w	body linear velocity components with respect to the x, y, z fixed-plane axes
u, $\widetilde{v}$, $\widetilde{w}$	body linear velocity components with respect to the $\widetilde{x}$, $\widetilde{y}$, $\widetilde{z}$ body-fixed axes
V	total velocity
W	body weight
α	angle of attack
β	angle of sideslip
$\vec{a}$	vector angle of attack
δ	flap angular position
ψ, θ, ϕ	Eulerian reference angles
ρ, ρ_A	air density
ρ_B	body density
μ	derivative with respect to Mach number
λ	quaternion
Δ	denotes small increment

subscripts

ss	steady-state
o	initial conditions unless otherwise specified
M	refers to Magnus effect

I. INTRODUCTION

There exists a need for an inexpensive and reliable technique which will restrict or control the descent velocity of missile payloads, air-droppable stores, and expended boosters. One means by which the descent velocity of a body may be reduced is by initiation of a flat spinning motion such that the body continuously presents a large fraction of its maximum projected area to the free airstream. Because of the large increase in both the drag area and the drag coefficient as the angle of attack is increased to near 90 degrees, the deceleration at very large angle of attack can be many times greater than that of the same body in normal stable flight at small angle of attack. Autorotative spinning (or yawing) motion is one means by which a large angle of attack can be developed and sustained.

An initial analytical investigation of body autorotative motions at large angle of attack was accomplished in 1961 by the Advanced Technology Division of Electronic Communications, Inc. under Air Force contract AF 29(600)-2936. The most significant accomplishment of this initial work was the development of a six-degrees-of-freedom trajectory program for the UNIVAC 1103A digital computer at Holloman Air Force Base. By use of the computer program, the autorotative motion of a small, rapidly rolling cone-cylinder body was investigated for a wide range of conditions including variations in center of mass, initial roll and yaw spin rates, and initial velocity and altitude. These studies are summarized in Reference 1.

The principal tasks specified for the present contract were:

1)   Investigations concerned with assessment of
        characteristic effects encountered during the
        transient and equilibrium phases of an auto-
        rotative motion.

2)   Parametric studies of body configurations
        exhibiting a self-sustained motion in a variety
        of environmental conditions.

3)   Extraction of significant parameters favorably
        affecting the recovery phase and the stability
        regions of pertinent shapes.

4)   Examination of computational procedures and
        computer sub-routines for increased efficiency
        in large-scale computations and accuracy
        improvements.

        To effectively accomplish objectives (1), (2), and (3), it was at
once recognized that a simplified theory for the autorotative motion of
bodies at large angle of attack would be required. Previous work had
illustrated an effective approach to this problem by application of the
small perturbation theory. By establishing theoretical relationships
between desired autorotative motions and body physical and aerodynamic
characteristics and flight environments, it would be possible to provide
the required understanding of body autorotative motion.

        The principal results of the work on the outlined tasks, including
the development of the new theory for autorotative motion, are described
in this report. The material has been organized such that the reader is

first acquainted with the aerodynamic problems associated with bodies at large angle of attack. Several aerodynamic mechanisms capable of sustaining large angle of attack autorotative motion are also described, along with the problem of incorporating these effects into the equations of motion. This material constitutes Section II of the report.

Because of the enormity of the aerodynamic data which must be provided for each body configuration, the more extensive investigations in this program have been limited to two basic bodies: 1) a fineness-ratio-eight cone-cylinder representative of a small missile, and 2) a body representative of a large liquid propellant booster of the Saturn class. Complete geometric, inertial, and aerodynamic data for the two body configurations have been presented in Section III for easy reference.

Section IV is devoted to the changes which have been made in the six-degrees-of-freedom trajectory program. Results obtained from the numerical integration of the complete equations are presented in subsequent sections.

The new autorotative motion theory is summarized in Section V, and the detailed development of the equations is presented in Appendix III. The steady-state solutions as obtained from the linear theory are interpreted, and both the static and dynamic stability of near steady-state motions are discussed. Finally the linear theory is compared with numerical results obtained from the complete equations of motion.

Quantitative results from a number of specific trajectory and motion studies are presented in Section VI. The results are based on both the newly derived equations for steady-state autorotation rate and attitude, and numerically integrated motion histories and trajectories. The various parameters affecting autorotation development are investigated for both low altitude and re-entry flight conditions. The differences between Magnus and

3

non-Magnus spins are clearly illustrated, and the effects of variation in center of gravity, roll spin rate, and spin propelling moment are indicated from parametric studies. The effectiveness of an autorotative motion in limiting the dynamic pressure and aerodynamic heating environments during re-entry is shown by comparisons with both tail-first and tumbling re-entry trajectories.

II. GENERAL AERODYNAMIC CHARACTERISTICS OF BODIES
AT LARGE ANGLE OF ATTACK

The study of large angle of attack autorotative motions for missile recovery is impossible without a detailed knowledge of:

1) The autorotative moment, and its dependence upon the body attitude and motion.

2) The aerodynamic stability derivatives, which represent the response of a given body to its angle of attack, flight velocity, Mach number, and angular motion.

3) The body retardation force, and its variation with angle of attack, Mach number, Reynolds number, and body geometry.

These considerations will be discussed in the following paragraphs.

A. AUTOROTATIVE YAWING MOMENTS

It was shown in Reference 2 that a large angle of attack cannot be sustained without yawing (spinning) motion unless the aerodynamic center of pressure is nearly coincident with the center of gravity. For this study,

the most general case of an untrimmed aerodynamic overturning moment
is considered, and we will examine several aerodynamic systems for
generation of pro-spinning moments, such that the inertial forces will
stabilize the unbalanced overturning moment. If the body has some yaw
angular velocity, then the local velocity vector at body sections displaced
from the center of rotation will be canted to one side as illustrated in the
following sketch
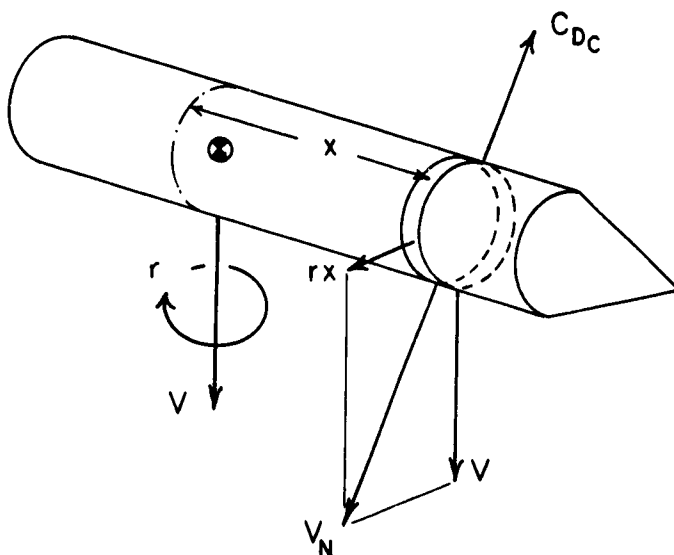
If the body has an aerodynamic force system in which the local cross
forces are in line with the local velocity vector, then the yaw component
of the local force will resist the yaw angular velocity. This is the normal
or anti-spinning condition as illustrated in Figure 1.

Non-Circular Cross Section. In the case of a non-circular body
cross section, Polhamus, Reference 3, has shown that the direction of
the cross force is strongly dependent upon both the Reynolds number and

the direction of the cross velocity vector relative to the body cross section as illustrated in Figure 1. A typical variation of side force coefficient with flow angle, ϕ, for a modified-square cylinder is illustrated in Figure 2. As ϕ becomes greater about 8 degrees, it will be noted that the side force and spin propelling moment decrease, and at about 14 degrees, the side force begins to resist the angular motion. Because of this characteristic, the maximum tip speed ratio is limited to about $r\,l\,/2V \approx 0.3$ with this force mechanism. It will also be shown, subsequently, that much greater side force coefficients for a wider range of tip speeds can be obtained from either the Magnus effect or from a small flap on a circular cylinder. For these reasons, the non-circular cross section will not be discussed further.

Magnus Force. The aerodynamic Magnus effect is the most natural phenomenon for development of an autorotative moment because it is inherently oriented normal to the flight velocity vector. Therefore, as long as some angle of attack exists, and the Magnus center of pressure and the body center of mass are not coincident, an autorotative moment will exist.

The aerodynamic Magnus force on bodies of revolution, including the effects of Reynolds number and surface speed, has been investigated extensively by H. Kelly of the Naval Ordnance Test Station, Reference 4. The aerodynamic Magnus force on finite length cone-cylinders for angles of attack from zero to 90 degrees has also been measured experimentally in the WADD 20-foot subsonic wind tunnel as part of the original Air Force investigation of autorotative recovery, Reference 5.

The accumulated subsonic experimental Magnus force data show a large dependence of the Magnus force on the cylinder cross flow Reynolds

7

number, especially in the subcritical and critical Reynolds number ranges. However, at large supercritical Reynolds number, the Magnus force becomes a nearly constant linear function of surface speed ratio and the two-dimensional Magnus lift coefficient C_{N_p} has a value of about 4 per radian at small values of pd/2V.

The effect of fineness ratio on the aerodynamic Magnus force at subsonic velocity is small, and available data indicate that the two-dimensional Magnus force coefficient will be reduced less than about 10 per cent for fineness ratios greater than 5. There is also a decrease in the Magnus force derivative C_{N_p} with increasing surface speed ratio, but this effect is also small for smooth bodies with values of pd/2V less than about 0.4.

There is also a question as to the effect of protuberances on the Magnus force at large angle of attack. For example, in practical application of a Magnus-type autorotation it would be desirable to initiate and sustain the roll rate through the use of aerodynamic vanes or rotors. Tests of a rib-type rotor similar to that depicted in the sketch below were made in the University of Maryland subsonic wind tunnel, Reference 6, and surface speed ratios as large as 0.39 were obtained with this type of rotor on a fineness-ratio-four cylinder at an angle of attack of 90 degrees.

Wind
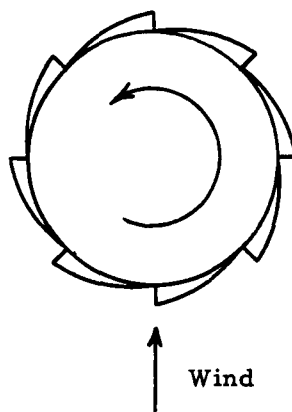
RIB-TYPE ROTOR

A correlation of subsonic Magnus force data at 90 degrees angle
of attack from References 4, 6, 7, and 8 is presented in Figure 3. The
effects of low aspect ratio fins and the rib-type rotor are depicted, in
addition to the effect of body fineness ratio. All of the data are for super-
critical cross flow Reynolds numbers. At surface speed ratios greater
than about 0.3, the Magnus force is seen to decrease rapidly when the
protuberances are present. However, at lower surface speed ratios
the protuberances do not appear to reduce the Magnus force.

The effects of angle of attack and Mach number on the Magnus force
are illustrated in Figure 4. All of the data are for smooth cylinders. The
increase in the Magnus force coefficient at angles of attack between approxi-
mately 40 and 60 degrees is not fully understood, although this phenomenon
has been noted in other data not shown. Since the cross flow Reynolds
number decreases at angles of attack less than 90 degrees, it would be
anticipated from cross flow theory that the Magnus force would also decrease,
since Kelly has shown that the Magnus force coefficient decreases with
decreasing Reynolds number in the supercritical Reynolds number range.
It must therefore be concluded that the axial flow and boundary displacement
effect play an important role in the intermediate angle of attack range.

The data presented in Figure 4 for Mach numbers above the cylinder
critical Mach number have been obtained from References 9 and 10, which
were not available for the earlier investigations reported in Reference 1.
Unfortunately, the Magnus effect is seen to decrease very rapidly for Mach
numbers above the cylinder critical Mach number, and at Mach numbers
above unity, the two-dimensional Magnus force coefficient is reported to
be less than 0.05. This rapid decrease in the Magnus force with increasing
Mach number is primarily a result of the circulation being restricted to
the subsonic portion of the boundary layer and the wake. Because of the

9

extremely thin boundary layer on the forward portion of the cylinder, it is reasonable to assume that nearly all of the circulation is confined to the wake and the aft portions of the boundary layer where separation occurs.

So far as is known, Magnus force data on inclined spinning bodies at transonic velocities have been measured only at angles of attack less than about 40 degrees. As can be seen from Figure 4, the Magnus force can exceed the two-dimensional value in this intermediate angle of attack range. At transonic velocities, this characteristic would be expected if the Magnus force were primarily dependent upon the cross flow Mach number. In Reference 10, Magnus force data on inclined bodies were plotted versus the cross flow Mach number, and a rough correlation was found to exist, thus supporting the observed increase in Magnus force at intermediate angles of attack.

Effect of Flaps on a Circular Cylinder. Recent experiments by Lockwood, et al, of NASA, References 11 and 12, have shown that a small flap can generate a significant amount of circulation and lift on a circular cylinder with large cross flow. Although most of the tests have been two-dimensional, the data should be approximately applicable to finite length cylinders. Both single and double flap arrangements have been investigated, as well as the effect of flap angular position and chord length. The lift generated by a longitudinal flap or strake can be used for producing an autorotative moment by placing the center of lift well forward or aft of the center of mass.

Two-dimensional subsonic lift and drag data for a circular cylinder with various flap arrangements are presented in Figure 5. These data were taken from Reference 11, and in all cases, the flap chord to body diameter ratio c/d is only 0.06.

10

Of particular interest is the large lift which can be obtained at
Reynolds numbers greater than 3.6×10^5, and the large drag increase
which occurs with addition of flaps at large Reynolds numbers. The
smooth cylinder drag coefficient at large Reynolds numbers is seen to
be increased by a factor of about 6 by the addition of the double flaps
180 degrees apart. The effect of flap angular position is also shown
in Figure 5. These data indicate that the lift of a fixed flap will stay
positive even though the local cross flow is rotated as much as ± 50
degrees. This is in great contrast to the results which were described
earlier for the non-circular cylinders.

The effects of flap chord and Mach number on the lift character-
istics of a circular cylinder are illustrated in Figure 6. The data are
taken from Reference 12. For low subsonic Mach numbers, it is evident
that a flap chord to body diameter ratio, c/d, of only about 0.02 is required
for a lift coefficient of 1.0. With increasing Mach number, the flap chord
must be increased to maintain lift effectiveness, and at Mach numbers of
0.5 and greater, the maximum lift is attained at a c/d of about 0.25. For
flaps of constant chord, a large reduction in lift will occur at transonic and
supersonic Mach numbers, but the reduction will be considerably less than
that which has previously been described for the Magnus force. At the
highest Mach number tested, M = 1.9, a straight flap of chord ratio
c/d = 0.1 produced a C_L of 0.3. At higher Mach numbers the flap
could be canted with the trailing edge downstream; for example, with
45 degrees deflection, a Newtonian section lift coefficient of 0.1 would
be obtained for a projected flap chord to diameter ratio of 0.1.

Several cylinder body configurations have been devised which can
effectively utilize the lift and drag characteristics of flaps. The most
effective combination is shown in the following sketch.

11
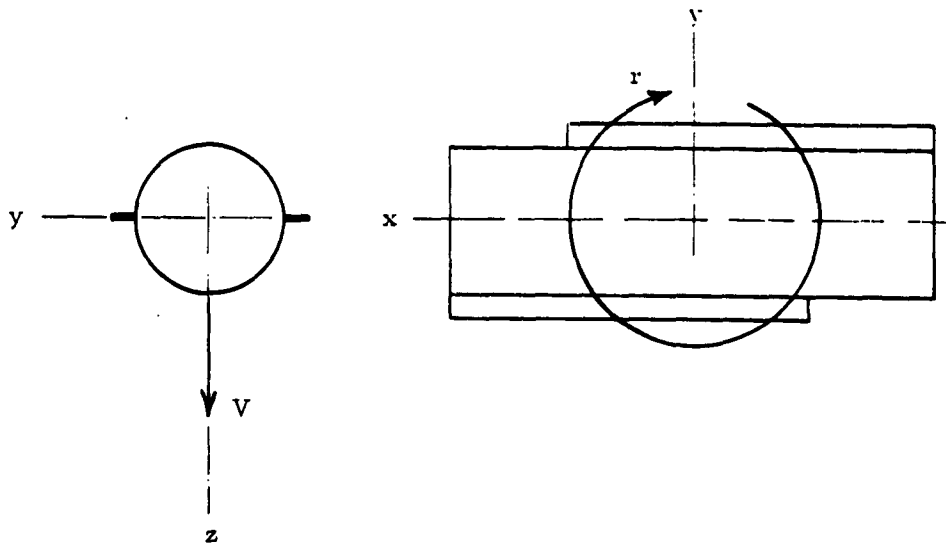
The single flaps at the end of the body provide the yawing or spin propelling moment, and the double flaps in the center provide additional drag. Because of the symmetrical arrangement of the flaps, a rolling moment due to flaps is eliminated. The autorotative and spinning character-istics of this type of configuration will be discussed in a later section.

B.   AERODYNAMIC STABILITY DERIVATIVES

In addition to the aerodynamic spin propelling moments described heretofore, the static aerodynamic overturning moment in the plane of the total angle of attack, and the moments due to body angular velocity are important quantities which will be found represented in both the exact and approximate equations of motion. Fortunately, Murphy and Nicolaides, Reference 13, have shown that the aeroballistic derivatives for symmetrical bodies are idencial for both missile-fixed and fixed-plane coordinates, if

the body accelerations are neglected. Consequently, in the exact equations of motion, Appendix II, the aerodynamic contribution will be seen to be the same for both coordinate systems. In the following discussion we also treat the dependence of the aerodynamic force system on the angle of attack in generality, and the results are applicable to either coordinate system.

Aerodynamic derivatives for bodies at large angle of attack are strongly influenced by the body end configuration. In the previous contract, Reference 1, aerodynamic data were examined only for the case of cone-cylinder bodies. However, many configurations which might be considered for autorotative large angle of attack recovery, such as booster rockets, are typically blunt-ended. Consequently, the aerodynamic characteristics of flat-ended cylinders have been examined in some detail during the course of the present contract.

Static Pitching Moment. The variation of the static overturning moment with angle of attack can best be characterized by considering the normal force and the center of pressure separately. A correlation of center-of-pressure data for flat-ended cylinder bodies is presented in Figure 7. Both subsonic and supersonic Mach numbers are represented. The data are from References 6 and 14. For subsonic Mach numbers, the center-of-pressure variation with angle of attack is nearly defined by a single curve. At supersonic Mach numbers the center of pressure approaches the centroid of the cylinder for all angles of attack greater than about 20 degrees.

A correlation of the normal force coefficient with angle of attack has been made for both subsonic and supersonic Mach numbers. For large angles of attack (i. e., near 90 degrees), no consistent trend is

13

observed in the subsonic normal force data, Figure 8, even though all of the data are at supercritical Reynolds numbers. However, in all cases, the values of $C_N / C_{N\pi/2}$ for large angle of attack exceed the $\sin^2 \alpha$ variation representative of sweep or cross flow theory.

For supersonic Mach numbers, the normal force coefficients closely follow the Newtonian theory, as can be seen from Figure 9.

Aerodynamic Derivatives Dependent Upon Angular Velocity.

The aerodynamic response to body angular motion is extremely important in the analysis of autorotative yawing motion. In particular, the effect of p, q, and r on the moments about the y and z axes must be known. Because the body configurations considered in this report are essentially axi-symmetric, it suffices to investigate only the effects of p and r, if we consider all of the velocity components u, v, and w independently.

For large angle of attack, the body aerodynamic force distribution can be assumed to depend almost entirely upon the local cross flow. Based on this assumption, a complete analysis of the aerodynamic moments due to transverse angular velocity and roll spin at large angle of attack has been accomplished, and the details are presented in Appendix I.

The analysis indicates that, to the first order, only the derivatives C_{n_r}, C_{M_q}, and $C_{M_{pr}}$ need be considered for large angle of attack motions. Integral expressions for these derivatives are then derived. It must be pointed out that C_{n_r}, C_{M_q}, and $C_{M_{pr}}$ are not aeroballistic (i. e. , they are not related to the complex cross angular velocity, q + i r), and they must be interpreted in light of the coordinate system which is used. Also, they are not constants, but have a functional dependence upon the magnitude of the angular velocity components, as well as the linear velocity components, u, v, and w.

The only known experimental data available to substantiate the theoretical angular velocity derivatives are the measurements of Reference 5. This reference confirms the estimated value of C_{n_r} obtained from equation (15) of Appendix I within about 20 per cent, when the estimated derivative is based on an equivalent C_{D_C} adjusted for body end effect as suggested in Appendix I. The data in Reference 5 were obtained for tip speed ratios, $r\,\ell/2V$, less than 0.45. Consequently, the predicted non-linearity of C_{n_r} at large tip speed ratios (i.e. $r\,\ell/2V$ in excess of 1.0) was not observed.

The derivative $C_{M_{pr}}$ qualitatively describes the results in Reference 5, which show a significant variation of the pitching moment with combined roll and yaw rates. Quantitatively, the theory of Appendix I was found to overestimate the value of $C_{M_{pr}}$. However, it is not known whether this one case is representative. It is, however, quite possible that the local Magnus force is smaller near the ends of the body. In this case, the magnitude of $C_{M_{pr}}$ would be considerably reduced.

A serious problem arises when it is attempted to apply the theoretical values of the angular velocity derivatives to a rolling body-axis system, because, in this case, the derivatives C_{n_r}, C_{M_q}, and $C_{M_{pr}}$ become periodic with the rolling motion. Since it is impracticable to account for such periodic behavior, it is necessary to assume in this case that $C_{n_r} = C_{M_q}$ and $C_{M_{pr}} = 0$.

When fixed-plane axes are utilized and the angle of attack is near 90 degrees, C_{n_r}, C_{M_q}, and $C_{M_{pr}}$ can be introduced independently into the equations of motion without complication. The further assumption of $V = w$ allows these derivatives to be evaluated in closed form, although they are still non-linear.

C.   BODY DRAG

The drag of a cylinder body is influenced by angle of attack, Mach number, Reynolds number, fineness ratio, and protuberances such as flaps and rotors. An understanding of these effects is obviously a necessary part of any study dealing with aerodynamic deceleration of bodies.

Since much of the more recent experimental data have not been adequately correlated for the purposes of this program, an effort has been made to determine the salient features of the aerodynamic drag force.

The effects of fineness ratio and Reynolds number on the low-speed crosswind drag characteristics of cylinder bodies are adequately described in Reference 15, and the more recent data examined are in agreement. The most significant aspect of the low-speed data is the fact that the drag does not decrease with decreasing fineness ratio in the supercritical Reynolds number range, contrary to the results for low Reynolds numbers.

At transonic Mach numbers, the effect of fineness ratio is illustrated by the use of the parameter, η , which is the ratio of the drag coefficient of a circular cylinder of finite length to that of a cylinder of infinite length. Figure 10 presents the variation of η with fineness ratio for Mach numbers of 0. 6 and 1. 2. For comparison, the curve for R_N = 88, 000 is reproduced from Reference 15. It is of interest that the η values at 0. 6 Mach number, which average about η = 0. 6 for fineness ratio less than 8, are in general less than the value of η at low Reynolds number. At Mach number 1. 2, the drag proportionality factor, η , approaches unity at a fineness ratio of about 20.

Until recently, the transonic cross flow drag of finite length cylinders had not been measured accurately. Now, free-flight tests have been reported, Reference 16, which show the drag of a fineness-ratio-3. 5 cylinder for

Mach numbers ranging from 0.4 to 3.0. These data are represented here as Figure 11. For comparison, the infinite cylinder drag curve, obtained from the correlated data in Reference 10, is illustrated. Since the drag peak for the fineness-ratio-3.5 cylinder is very flat, it is clear why η does not increase until the Mach number exceeds the Mach number at the infinite cylinder drag peak. For Mach numbers above 2.0, it can be seen that $\eta = 1$ even for the 3.5 fineness ratio cylinder.

The relatively small cross flow drag coefficient of the smooth circular cylinder at low subsonic velocity and at supercritical Reynolds numbers, which are the conditions under which most bodies will impact with the earth, has been of concern because it diminishes the recovery effectiveness of a large angle of attack descent. Consequently, the effects of protuberances on cylinder cross flow drag have been investigated, since flaps and rotors are being considered as possible mechanisms for achieving autorotation moments. It is found that the smooth cylinder drag coefficients are increased by a factor of about 2.5 in the supercritical Reynolds number range if either a single flap is placed normal to the flow, or a cylinder with several fin-like appendages is rotated. Thus, single flap or rotor-type appendages on a given fineness ratio body result in cross flow drag coefficients very near those at subcritical Reynolds numbers. Even further drag increases are indicated for double flaps, as was illustrated in Figure 5.

There has also been the question of the angle of attack for maximum drag, particularly at terminal descent conditions. Examination of data from References 6 and 7 for flat-ended cylinders shows that the maximum drag coefficient is obtained at an angle of attack of about 70 degrees (or 110 degrees) at low subsonic velocities.

III. BODY CONFIGURATIONS AND BASIC DATA

To make the results of the theoretical and analytical investigations as realistic as possible, two general body configurations have been selected for study. One body is a fineness-ratio-eight cone-cylinder, representative of a small missile payload; the other body is a fineness-ratio-3.97 circular cylinder representative of a Saturn class liquid propellant booster. The physical characteristics of these bodies are presented in Tables I and II, and the data are typical of existing or proposed vehicles. The weight and inertia data for the large booster are representative of the empty configuration which would exist after payload separation and prior to re-entry.

Aerodynamic data for the two configurations have been estimated from the references which are described in Section II. Unfortunately, the estimated variations of the aerodynamic coefficients with angle of attack cannot be re-constructed exactly from the stability derivatives which are included in the six-degrees-of-freedom equations of motion (see Section IV). This is a result of the fact that the power series expansions for C_N, C_{N_p}, C_M, and C_{M_p}, include coefficients for only $\vec{a}$, $\vec{a}^3$, and $\vec{a}^5$, and the expansion for C_x includes only C_{x_0} and a coefficient dependent upon $\vec{a}^2$. Although the above expansions are quite adequate when all of the aerodynamic force and moment variations are symmetrical about $\pi/2$ radians angle of attack, the axial force and the moments are typically non-symmetrical, and this makes the fitting process more difficult, especially for the complete angle of attack range $0 - \pi$ radians. The derivatives which have been used in the six-degrees-of-freedom numerical solutions are tabulated in Tables I and II.

In the linearized two-moment equations of motion, extensive use is made of the coefficients $C_{M_{\pi/2}}$ and $C_{M_{p\pi/2}}$, which are the pitching moment and Magnus moment coefficients, respectively, at 90 degrees angle of attack. Consequently, these coefficients have also been tabulated for the basic centers of gravity.

In the case of the large booster, two separate concepts have been investigated for generation of the autorotation moment. For some studies the booster is assumed to be rolling with a small surface speed ratio, pd/2V. The surface speed ratios considered have been small enough such that they could be produced by very small axial ribs, such as those shown in the sketch on page 8. The details of the rotor have not been considered in this report, but the following assumptions have been made relative to its effect on the body:

1) The rotor does not change the vehicle mass or moments of inertia.

2) The rotor causes sufficient separation of the cross flow that a cross flow drag coefficient of $C_D = 1.15$ is obtained at low subsonic velocities.

3) The rotor will be able to develop a surface speed ratio of at least 0.3, at 90 degrees angle of attack.

4) For a given rotor, the body roll angular velocity is constant at all angles of attack.

For other studies, the large-booster spin propelling moment has been assumed to be produced by a flap system such as that described in Section II. In general, the flap geometry has not been specified in detail, but rather, constant values of the spin propelling moment have been

19

selected for the various flight regimes. All of the spin propelling moments considered could be obtained with flaps of no greater chord than 0.2 body diameters.

The problem of providing the correct roll orientation of the flaps has not been considered, as this is a mechanical detail. From a practicable point of view, the booster roll control system could satisfy this requirement. The cross flow drag coefficient of the booster with flaps was taken to be identical to the value used for the rolling booster.

The aerodynamic derivatives and coefficients for the small fineness-ratio-eight cone-cylinder body are based on the data of Reference 1, and are for a smooth surface. For this body, the roll rate is assumed to be generated by non-aerodynamic means and for each trajectory, the roll rate is constant.

IV. SIX-DEGREES-OF-FREEDOM TRAJECTORY PROGRAM
FOR UNIVAC 1103A DIGITAL COMPUTER

Equations of Motion. Six-degrees-of-freedom equations of motion for rolling and spinning axi-symmetric bodies were developed during a previous contract, Reference 1, and programmed for numerical solution on the UNIVAC 1103A digital computer at Holloman Air Force Base, New Mexico. The program allows for optimal use of the body-fixed or fixed-plane axes, as depicted in Figure 12.

An angular orientation scheme based on quaternions is incorporated, which permits motions to be computed for all possible body attitudes, without angular rate discontinuities, when the body-fixed axes are selected. The fixed-plane axes have a singularity at $\theta = \pi/2$, which precludes this axis system being used for motions with very large pitch amplitude.

The basic equations of motion for the computer program are presented in Appendix II. The equations are identical to those used in Reference 1, except that the linear aeroballistic damping derivative C_{M_q} has been replaced by the non-linear aerodynamic damping derivatives $C_{n_{r_0}}$, $C_{n_{r_2}}$, $C_{M_{q_0}}$, and $C_{M_{q_2}}$, and the new derivative $C_{M_{pr}}$ has been added to account for the distortion of the Magnus moment at large tip speeds. The numerical integration is accomplished using Milne's four-point method of prediction, and Simpson's rule for correction.

21

Integration Error. The basic equations of motion do not include the quaternions in their normalized form, so that after many integration intervals, small errors develop. Although a method for quaternion normalization is readily available, Reference 19, it could not be incorporated in the UNIVAC 1103A computer program because of the limited data storage capacity. To prevent the integration from continuing after appreciable error had developed, the stop condition

$$2(\lambda_o \lambda_2 - \lambda_1 \lambda_3) \geq 1.05$$

was made a basic part of the program. Examination of the trajectory data shows that the test criteria was usually satisfied when the average error of the quaternions, as calculated by the error equations of Reference 1, exceeded about 1×10^{-3}. It was further observed that one or more of the body attitude or angular rate variables became erratic when the quaternion error reached a magnitude of about 1×10^{-5}.

Consequently, it became necessary to predict the number of integrations which could be accomplished without exceeding an average quaternion error of about 1×10^{-5}. For better visualization of the quaternion error build-up, one trajectory was repeated with different time intervals, and the average quaternion error (order of magnitude) plotted versus time. These results are shown in Figure 13. It can be seen that not only the initial error, but also the rate of increase of quaternion error, is influenced by the integration time interval. For a fixed quaternion error limit, the duration of integration is approximately proportional to the inverse of the integration time interval.

The rate of increase of quaternion error also depends upon the oscillatory motion of the body. For steady motions, a correlation was

established between the system angular rates, the integration time interval, and the time required for the quaternion error to reach a magnitude of 1×10^{-5}. The maximum integration time was found to be given approximately by the empirical equation

$$t_{max} = \frac{\pi}{\omega \, \Delta t} - 5$$

where the angular rate ω is usually the yaw rate.

For trajectories of relatively long duration, such as during re-entry, where the angular rates are not constant, it was found expedient to break the trajectories into two or more segments, each with an appropriate integration time interval. The second and subsequent segments were re-initialized using the output data from the last interval of the previous segment.

V. A SIMPLIFIED THEORY FOR THE AUTOROTATIVE MOTION
OF BODIES AT LARGE ANGLE OF ATTACK

Of great interest in the general study of unstable motion is the steady, nearly-flat, autorotative spin. Analytical solutions for the motion of fully developed autorotations can provide the means for rapid assessment of the effects of the basic body and flight parameters on the spin characteristics. In addition, analytical solutions for the motion permit a much more comprehensive stability analysis to be accomplished.

The only previous comprehensive linear theory for the flat spin, which has been found in the literature, is an investigation of aircraft flat spins, accomplished by linearization of the three-moment equations of motion in body axis form. This work was reported by Klinar and Grantham, Reference 20. The three variables selected for their system of linearized equations were $\Delta\theta$, Δr, and $\Delta\beta$. The stability of the aircraft flat spin was subsequently investigated in terms of the initial yaw rate and the aerodynamic derivatives C_{l_β} and C_{n_β}.

If the autorotative motion of a simple cylinder body is treated in a similar manner, several complications develop. First, we would want to consider large roll rates so that the Magnus force could be included. Second, in the airplane, strong aerodynamic couplings exist between the rolling and yawing degrees of freedom which can be used to determine the sideslip angle β. However, for a simple cylinder body, the rolling degree of freedom does not provide relationships between $\Delta\theta$, Δr, and $\Delta\beta$. Third, Klinar and Grantham considered only the normal linear aerodynamic derivatives. Such derivatives do not adequately describe the aerodynamic characteristics of a simple cylinder or cone-cylinder body at large angle of attack.

24

An initial analysis of the body spin problem, using the same three variables, $\Delta\theta$, Δr, and $\Delta\beta$, was undertaken by the author in 1961 and is summarized in Reference 1. An important factor in the initial analysis was the use of a fixed-plane coordinate system, such that a steady roll rate could be considered without the addition of the rolling degree of freedom. For evaluation of the sideslip angle, β, the equation for lateral translation was added. The equation for lateral translation contained both θ and β as variables, and the coupling was due to the y component of the Magnus force. The introduction of lateral translation into the system of equations was equivalent to assuming that the body would descend along a helix, rather than along a straight-line type of trajectory. The resulting system of equations was of fourth order, and no simple analytic solutions for the steady-state motion were derived. In addition, the stability analysis became quite complex, and results could only be obtained by numerical evaluation of the roots and stability boundaries.

During the course of the present program, an investigation was made of the relationship between the yawing motion and the lateral translation to determine the desirability of using the translatory degree of freedom. A review of the available six-degrees-of-freedom trajectory data showed that the translatory motion was almost totally independent of the yawing motion. The six-degrees-of-freedom data showed that the β oscillations are due almost entirely to the translatory motion which develops during the first fractional cycle of yawing motion. Thus in actuality, the β and θ motions are unrelated, and the assumptions made in the previous linear equations regarding the Magnus force coupling are not valid. Because of this, only the pitching and yawing degrees of freedom have been considered in the present analysis.

The detailed development of the two-moment equations of motion for a spinning body at large angle of attack is presented in Appendix III. Appendix III contains, in addition, the equations for the steady-state motion

and also the equations describing the system stability, and approximations of the roots of the characteristic equation. A very important aspect of the new theory is the inclusion of more realistic variations of the aerodynamic moments with angle of attack, wherein the coefficient variations are assumed to vary as the product of the sine of the angle of attack and the magnitude of the coefficients at 90 degrees angle of attack.

In the new theory, the steady-state solutions for the autorotation rate and spin attitude are obtained in a very useful form. Also, because of the use of the fixed-plane coordinates, the steady-state solutions can be presented in terms of the Eulerian quantities, θ and ψ, thereby permitting a direct physical interpretation of the motion of bodies in vertical descent.

A.   STEADY-STATE SOLUTIONS

For Magnus-type autorotations where the roll rate is large, the steady-state yaw rate and autorotation attitude are found to be (see Appendix III)

$$r_{ss} = \frac{C_{M_p \pi/2}\, p\, \cos \theta_{ss}}{C_{n_r}}$$

or   (1)

$$\dot{\psi}_{ss} = \frac{C_{M_p \pi/2}\, p}{C_{n_r}}$$

and

$$\sin \theta_{ss} = \frac{K\, C_{M_{\pi/2}} - \dfrac{p^2\, C_{M_p \pi/2}}{C_{n_r}} \left[\dfrac{I_x}{I} - KL^2\, C_{M_{pr}} \right]}{\left[\dfrac{C_{M_p \pi/2}\, p}{C_{n_r}} \right]^2}$$ (2)

The new linear theory also describes slowly rolling spins in which the spin propelling moment is provided by a body-fixed flap or strake. In this case we obtain for the steady-state yaw rate and autorotation attitude

$$r_{ss} = \frac{C_{M_{z_0}}}{L\, C_{n_r}} \tag{3}$$

or

$$\dot{\psi}_{ss} = \frac{C_{M_{z_0}}}{L\, C_{n_r} \cos \theta_{ss}}$$

and

$$\sin \theta_{ss} = -\frac{A}{2} + \sqrt{\left(\frac{A}{2}\right)^2 + 1} \tag{4}$$

where

$$A = \frac{\left(\dfrac{C_{M_{z_0}}}{L\, C_{n_r}}\right)^2 \left(1 - \dfrac{I_x}{I}\right)}{K\, C_{M_{\pi/2}}}$$

For very flat spins, we have even more simply

$$\tan \theta_{ss} = \frac{1}{A} \tag{5}$$

Interpretation of the Steady-State Solutions. It is interesting that equations (1) and (3) give a result which would almost intuitively be expected, that is, that the steady yaw rate would be the forcing moment divided by the damping moment. The results for the steady-state autorotation attitude would be more difficult to surmise, although it will be noted that in both equations (2) and (5), the denominators contain the yaw rate squared. This might have been expected, since part of the inertial force, the centrifugal effect, is dependent upon r^2.

27

In regard to the autorotation attitude, the following generalizations can be made. First, it can be seen that the autorotation attitude will be increased positively for a positive pitching moment at $\alpha = \pi/2$. This would also be intuitively expected.

For Magnus-type autorotations, the second term in equation (2) can play a dominant role. The sign of this term also depends upon the sign of the Magnus moment coefficient. Since C_{n_r} is typically negative, we can see that autorotation will occur at a smaller θ when $C_{M_p \pi/2}$ is negative. The derivative $C_{M_{pr}}$ is also typically negative, and thus tends to increase the effective value of the inertia ratio, I_x/I in equation (2). When the Magnus moment has a very large negative value, it is possible for the body to autorotate in a nose-down attitude, even though the pitching moment is nose-up. Contrary to what might be expected, the roll spin direction does not affect the direction in which the autorotation attitude changes, because p appears only as p^2.

If the body center of gravity is near the midpoint, such that the aerodynamic pitching moment, $C_{M_{\pi/2}}$, is zero, we obtain the interesting result that the autorotation attitude, θ, is independent of the roll spin rate, inversely proportional to the Magnus moment, and directly proportional to the yaw damping. Thus, for configurations with small overturning moment, increasing roll spin rate is not an effective way to make the autorotation flatter.

Another interesting point which can be made is relative to the possibility for an autorotation where the body roll rate is only the component of the azimuth spin rate, i.e., $p = -\dot{\psi} \sin \theta$. This occurs when the total angular velocity vector is aligned with the velocity vector. This is also the manner in which the spin tests of Reference 5 were conducted.

Substituting $p = -\dot{\psi} \sin \theta$ into equation (1), we can see that

$$\frac{C_{M_{p\pi/2}} \sin \theta}{C_{n_r}} = -1$$

Since C_{n_r} is typically negative, the equation is only satisfied for $C_{M_{p\pi/2}}$ positive. For bodies with aft centers of gravity, $C_{N_{p\pi/2}}$ would also have to be positive, thus implying that this type of spin can be self-sustaining only at subcritical or supercritical Reynolds numbers, where $C_{N_{p\pi/2}}$ is always positive.

Similarity Parameters. To more clearly illustrate the effects of body geometry, inertial characteristics, and the air density on the steady-state autorotation characteristics, equations (1) through (5) can be trans-formed into new variables, which can subsequently be combined into similarity parameters. Configurations or flight conditions leading to the same similarity parameters will then have identical autorotative characteristics.

If the equilibrium descent velocity is assumed to exist at all altitudes, and if further, the descent velocity can be assumed to be independent of the body pitch attitude for reasonably flat autorotations, then we can introduce

$$V = \sqrt{\frac{2 W}{\rho_A S C_{D_C}}}$$

This, together with the following expressions for

29

$$S = \ell d$$

$$W = \frac{\pi}{4} \rho_B g d^2 \ell$$

$$I = \frac{\pi}{4} \rho_B d^2 \ell K^2$$

$$I_x = \frac{\pi}{4} \rho_B d^2 \ell k^2$$

$$C_{M \pi/2} = C_{D_C} \frac{4}{\pi} \frac{\ell}{d^2} \Delta x_{c.p.}$$

$$p = \frac{J_1}{L} \qquad\qquad J_1 = constant$$

$$C_{n_r} = J_2 \left(\frac{\ell}{d}\right)^3 C_{D_C} \qquad\qquad J_2 = constant$$

permit the steady-state solutions to be expressed in terms of new variables. The above equation for p assumes a constant surface speed ratio, $pd/2V$ for the Magnus spins, and is consistent with the use of an aerodynamic roll vane system for generation of the roll rate. The yaw damping relationship is derived in Appendix I. Substituting the above relationships into equations (1), (2), (3), and (5), results in the following new expressions for the steady-state variables:

$$r_{ss} = \frac{J_1}{J_2} \; C_{M_{p\pi/2}} \; \cos\theta_{ss} \; \frac{1}{\left(\frac{\ell}{d}\right)^3} \sqrt{\frac{2\pi g}{C_{D_C}{}^3 \, d} \; \frac{\rho_B}{\rho_A}}$$

$$\sin\theta_{ss} = \frac{\dfrac{8 J_2{}^2}{\pi^3} \; \dfrac{\rho_B}{\rho_A} \; C_{D_C}{}^3 \left(\dfrac{\ell}{d}\right)^6 \; \dfrac{d\,\Delta x_{c.p.}}{K^2}}{C_{M_{p\pi/2}}{}^2 \; J_1{}^2}$$

$$- \frac{J_2 J_1{}^2 \; C_{M_{p\pi/2}} \left(\dfrac{\ell}{d}\right)^3 C_{D_C} \left[\dfrac{k^2}{K^2} - \dfrac{C_{D_C}\,d}{2\,\pi g} \; \dfrac{\rho_B}{\rho_A} \; C_{M_{pr}}\right]}{C_{M_{p\pi/2}}{}^2 \; J_1{}^2}$$

(Magnus Autorotation)

$$r_{ss} = - \frac{C_{M_{z_0}}}{J_2 \left(\dfrac{\ell}{d}\right)^3} \sqrt{\frac{2\pi g}{C_{D_C}{}^3 \, d} \; -\frac{\rho_B}{\rho_A}}$$

$$\tan\theta_{ss} = \frac{8 J_2{}^2}{\pi^3} \; \frac{C_{D_C}{}^3}{C_{M_{z_0}}{}^2} \; \frac{\ell\,\Delta x_{c.p.}}{K^2} \left(\frac{\ell}{d}\right)^5 \; \frac{\rho_A}{\rho_B} \; \frac{1}{1 - \dfrac{k^2}{K^2}}$$

(Non-Magnus Autorotation)

31

It can be seen from the above equations that the autorotation characteristics are determined by the body length, diameter, radii of gyration, the relative density of the body with respect to air density, and the distance from the body center of gravity to the body center of pressure, as well as by the aerodynamic derivatives.

Unfortunately, a single set of similarity parameters cannot be established for both the steady-state yaw spin rate and the autorotation attitude, θ. However, the similarity parameters for either r or θ alone are obvious, except for the case of the equation for $\sin \theta$ (Magnus autorotation), where the numerator consists of two terms. In this case the dependence of the autorotation attitude on (ρ_B / ρ_A), (ℓ/d), d, etc. is different for each term, and no singular dependence can be established with the geometric, inertial, and atmospheric parameters.

It is interesting to note that increasing air density will in general result in reduced yaw spin rate and increased autorotation attitude. Consequently, in designing an autorotative recovery system, the maximum autorotation attitude can be selected for impact conditions and at altitude the autorotation attitude will be smaller.

To illustrate the effect of body size on the autorotation attitude, calculations have been made for two geometrically similar but different size bodies with the same aerodynamic characteristics. The relative density of the two bodies, of course, must be different since larger bodies tend to have a lower relative density. The larger body is assumed to be the large booster, Table II, and the small body is identical except that

$$d \quad = 0.5 \text{ ft}$$
$$\rho_B = 0.158 \text{ slugs/ft}^3$$
$$I \quad = .096 \text{ slug-ft}^2$$

The steady-state autorotation attitudes for both bodies are presented in Table III, based on both a Magnus spin propelling moment, and the use of a flap for generation of a spin propelling moment. In this comparison, the Magnus moment and the moment due to the flap have been made identical at 90 degrees angle of attack. For both of these examples, the center of gravity has been assumed to be 1.22 diameters from one end of the cylinder. We see from the results that the larger body tends to autorotate with a more nose-up attitude for both types of autorotations, and also that in this case, the non-Magnus autorotations are considerably flatter.

B.   STABILITY OF AUTOROTATIVE MOTIONS

The linear autorotative motion theory permits a classical evaluation of the static and dynamic stability of near steady-state large angle of attack spinning motions. The stability theory and the stability equations are presented in Appendix I.

In general, there is little indication of possible instability in fully developed flat spins, although configurations of interest should be investigated for various flight conditions.

The stability requirements for non-Magnus slowly rolling autorotative spins are the least stringent. Sufficient conditions for both static and dynamic stability, if the steady-state spin attitude, θ, is small, are that $C_{n_r} < 0$, $C_{M_q} < 0$, and $I_x/I < 1$. These requirements will be met for nearly all configurations of interest.

For Magnus-type autorotations with $C_{M_{\pi/2}}$ zero, the static stability criteria imply that the Magnus moment coefficient satisfy the inequality

$$\left| C_{M_{p\,\pi/2}} \right| > \left| C_{n_r} \left[\frac{I_x}{I} - KL^2 C_{M_{pr}} \right] \right| \qquad (6)$$

33

in addition to the requirement as above that $C_{n_r} < 0$. It is interesting that the $C_{M_{p\pi/2}}$ requirement is equivalent to $\sin \theta_{ss} < 1$; therefore, for flat autorotative spins the requirement that $C_{n_r} < 0$ is sufficient. For $C_{M_{\pi/2}}$ not equal to zero, the stability must be evaluated numerically.

The dynamic stability of the Magnus-type autorotations, as evaluated by the Routh criterion, is not insured by either θ being small or C_{n_r} and C_{M_q} being negative. However, all configurations investigated in the present program have been found to be dynamically stable at the steady-state values of autorotation attitude and yaw rate.

Additional insight into the system stability can be achieved by direct approximation of the roots of the characteristic equation, assuming θ_{ss}, KL, and I_x/I to be small and r_{ss} large. The analysis is shown in Appendix I. The roots of the characteristic third-degree polynomial were found to be, approximately

$$\lambda_1 = KL\, C_{n_r} \tag{7}$$

and

$$\lambda_{2,3} = \frac{KL\, C_{M_q}}{2} \pm ir \tag{8}$$

Thus, by this analysis $C_{n_r} < 0$ and $C_{M_q} < 0$ are sufficient conditions for stability.

Comparison of the Approximate Motion Theory with Six-Degrees-of-Freedom Motion Histories. The accuracy of the approximate motion theory has been investigated by comparison of the steady-state solutions as given by equations (1) and (2) with exact six-degrees-of-freedom motion histories.

For these comparisons a cone-cylinder body configuration was utilized. Table I contains the physical characteristics of the body as well as the aerodynamic derivatives for the six-degrees-of-freedom motion calculations and the coefficients $C_{M_{\pi/2}}$, $C_{M_p \pi/2}$, and C_{n_r}, which are used in the steady-state solutions.

Both the sub-critical and critical Reynolds number flight conditions were evaluated such that the effect of both positive and negative Magnus forces could be determined. The variations of C_M and C_{M_p} with angle of attack were assumed to be directly proportional to $\sin \alpha$ for the six-degrees-of-freedom trajectories to agree with the assumptions of the approximate motion theory (see Appendix I for a discussion of the aerodynamic considerations in the approximate theory). The power series expansions used in the six-degrees-of-freedom calculations provide a very good fit to $\sin \alpha$ in the vicinity of $\alpha = \pi/2$, as can be seen from Figure 14. Thus the principal effects to be observed in the comparison are

1) the effect of neglecting second-order
    terms in the approximate equations
2) the effect of neglecting the translational
    degrees of freedom

The initial conditions used for this comparison (corresponding to equilibrium descent) are summarized in Table IV. Except for case 2, which was initiated at zero yaw spin rate to observe the effect of yaw rate build-up, all runs were initiated at the approximate calculated steady-state autorotation conditions.

Time histories of θ and r from the six-degrees-of-freedom computer runs are illustrated in Figure 15, along with the computed

steady-state values of θ and r. The agreement of the average six-degrees-of-freedom motion amplitudes with the calculated steady-state solutions is very good, and in most all instances the difference is less than one per cent.

A second comparison can be made between the actual frequency and damping of the six-degrees-of-freedom motion histories and the roots of the characteristic equation describing the linear system. Both the approximate roots of the characteristic equation as given by equations (7) and (8), and the exact roots, as evaluated numerically, have been determined. These results are presented in Table V. From this comparison it is evident that the approximate roots agree quite closely with the exact roots, thus substantiating the assumptions made in the analysis.

The damping exponents shown in Table V were calculated from the six-degrees-of-freedom time histories. Since the essentially non-oscillatory yaw rate represents the real root, the root λ_1 was determined from an exponential approximation of the yaw rate time history. Likewise, the decay of the θ oscillations was used to calculate the real part of $\lambda_{2,3}$. The frequency data presented in the last column of Table IV represent the frequency of the θ oscillations.

For case 3, it is particularly noteworthy that the θ damping, as determined from the motion histories at $r/r_{\text{steady-state}} \approx 0.6$, is much greater than at near steady-state, whereas only a small difference exists in the exponent for the yaw rate. This shows that the variation in yaw rate has an effect on the θ oscillations, which is equivalent to an increased damping. An analogy can be made between the effect of a slowly changing yaw rate on autorotation attitude and the heteroparametric damping of re-entry angle of attack oscillations resulting from an increase in the air density with time.

VI.   TRAJECTORY AND MOTION STUDIES

The purpose of this section is twofold: first, to present the results of investigations of the body transient spin dynamics during autorotation development, which was accomplished by numerical integration of the complete equations of motion, and second, to show, quantitatively, the autorotative motions of the two body configurations for the several flight regimes of interest. The second objective has been accomplished by numerical integration of the complete equations of motion, and also by numerical computations based on the linear solutions for the steady-state motion.

A.   TRANSIENT SPINNING MOTION OF THE FINENESS-RATIO-EIGHT CONE-CYLINDER BODY

Perhaps the most important aspect of an autorotative motion is its initiation. Because in the present study we are dealing with bodies which have unstable aerodynamic pitching moments at least from 0 to 90 degrees angle of attack, we have a natural mechanism for initiating a large angle of attack motion. The roll rates which are considered are sufficient to generate a Magnus force, but insufficient to provide gyroscopic stability at small angle of attack.

One of the important deficiencies of the linear theory is its inability to predict accurately the stability of spinning motions at yaw rates much less than the steady-state yaw rates. If we examine the pitching moments

for a spinning body in vertical descent, as illustrated in Figure 16, we see
that the gyroscopic pitching moment, $I \dot{\psi}^2 \cos \theta \sin \theta$, which balances
the unstable aerodynamic pitching moment, M_y, will be greatly reduced
for small spin rates. As a result, we find that the pitching oscillations
are quite large at small yaw spin rates. When the angle of attack departs
greatly from 90 degrees during these oscillations, the body also experiences
a reduction in the spin propelling moment. Thus in the small yaw-spin rate
regime, there is a very complex balance of moments. To determine if the
motion will progress toward the steady-state solution under these conditions,
we must solve the equations of motion in their exact, non-linear form.

To investigate this problem, six-degrees-of-freedom motion histories
have been computed for the cone-cylinder body in vertical descent, assuming
various initial values of the ratio $r_{initial} / r_{steady-state}$. In general, the
initial attitude, θ, was taken to be small, such that the model motion begins
in an approximately horizontal plane. Various roll rates are also considered.
Although the roll rate has only a very small effect on the steady-state solution,
as given by the linear theory, the effect of roll rate on the transient spin
characteristics was unknown.

Typical transient motion histories for various initial yaw rates are
presented in Figure 17. A supercritical Reynolds number flight condition
($R = 5 \times 10^5$), corresponding to a descent velocity of 229 ft/sec at 15,200
feet, has been used such that the results will be applicable to other full-
scale configurations. The aerodynamic data for this Reynolds number are
presented in Table I as case 4. Examination of the motion histories in
Figure 17 shows that the initial pitching oscillations increase with decreasing
initial yaw rate. Although the pitch amplitude becomes larger with decreasing
yaw rate, the initial damping of the θ oscillations increases with decreasing
yaw rate.

One means of correlating these data is to establish a relationship between the maximum value of θ during the first pitch oscillation and the initial value of the yaw rate.

A correlation of the maximum amplitude during the first pitch cycle with the initial yaw rate is shown in Figure 18. The correlated data are presented for three values of the roll rate. It will be observed that for constant values of the ratio $r_{initial}/r_{steady-state}$, the value of θ_{max} will be nearly independent of the roll rate. For example, at initial yaw rates of about .1 $r_{steady-state}$, the maximum amplitude varies only from about 33 to 41 degrees; and at values of $r_o/r_{steady-state} = .5$, the variation in θ_{max} is only from 5 to 7 degrees. This investigation shows that for initial yaw rates greater than about .1 $r_{steady-state}$, we can develop the Magnus-type autorotation for surface speed ratios as low as .025.

B.   STEADY-STATE AUTOROTATION CHARACTERISTICS OF LARGE
        BOOSTER CONFIGURATIONS AT SEA LEVEL

For recovery of a large booster, it is conceivable that either a Magnus-type autorotation or an autorotation by the use of aerodynamic strakes or flaps could be employed for terminal deceleration and recovery. The purpose here is to show the salient differences between rapidly rolling (Magnus) and slowly rolling (propelling moment by use of flaps) spins for equilibrium vertical descent at sea level. The effects of center-of-gravity location on both types of autorotation will also be discussed. All of the comparisons have been made on the basis of the same descent velocity, 228 ft/sec.

Figure 19 shows the steady-state autorotation attitude as a function of the steady-state yaw rate, r, for the basic center-of-gravity position. The

data were computed using equations (1) through (4). The various yaw rates were obtained by making the autorotative moment a parameter. For the Magnus spins, the parameter was the roll rate, and for the non-Magnus autorotations the parameter was the flap length, l_F. The variations of p and l_F with r are also illustrated in Figure 19.

At constant yaw rate the non-Magnus autorotations are seen to be flatter, and the difference becomes greater as the yaw rate increases. This latter effect is a result of the Magnus autorotation attitude increasing at large yaw rate due to the unfavorable effect of the derivative, $C_{M_{pr}}$.

Effect of Center of Gravity. The previous comparison between Magnus and non-Magnus autorotations was for the basic center-of-gravity position, which is 1.22 diameters from the base. It is also worthwhile to examine the effect of the center-of-gravity location along the axis of symmetry. The analysis requires that the aerodynamic yaw damping derivative, C_{n_r}, be re-evaluated for each center of gravity as well as the aerodynamic overturning and Magnus moments. Again using equations (1) through (4), we can plot the steady state yaw rate, r_{ss}, and the steady-state autorotation attitude, θ_{ss}, versus center-of-gravity location. The results are presented in Figure 20.

This calculation reveals a very interesting fact about the Magnus-type autorotations, which is that the minimum autorotation attitude and maximum yaw rate are obtained at a center-of-gravity position about 0.3 body lengths from the end of the cylinder. This is very close to the basic center-of-gravity location for the large booster configuration.

For large aerodynamic drag, we can conclude that the slowly rolling, non-Magnus autorotations will be more suitable when the body center of gravity is near the geometric center of the body, and the Magnus autorotations will be more suitable when the center of gravity is near the ends of the body.

40

C. TRANSIENT MOTION CHARACTERISTICS OF THE LARGE BOOSTER
CONFIGURATION (LOW ALTITUDE)

In the previous paragraph, it was shown that for steady vertical descent, autorotation attitudes less than about 30 degrees from horizontal are possible for the large booster configuration with either Magnus or flap-generated autorotative moments. It is also necessary to examine the detailed dynamics during autorotation initiation, using the exact six-degrees-of-freedom equations of motion. For this analysis an initial altitude of 20,000 feet and an equilibrium vertical descent velocity of 313 ft/sec, corresponding to an angle of attack of ninety degrees, was selected. The first problem was to determine the initial stability of the motion, that is, the conditions under which the motion would progress towards the steady-state solution. The second problem was to examine the descent trajectory and motion over a longer period of time to ascertain if the actual motion, as calculated by the six-degrees-of-freedom equations of motion, approaches the steady-state autorotation attitude and yaw rate as given by the simplified equations of motion.

Some of the conditions investigated, the results of which will be described in this report, are indicated in Table VI. In all cases, the body had an initial aerodynamic instability in pitch, i.e., a positive pitching moment coefficient.

For investigation of the initial stability of an autorotative motion, the variations in the linear velocity component are not of great consequence; consequently, for preliminary analysis attention was restricted to the angular motions of the body. Plots of the Euler angles θ and ψ versus time, for the conditions in Table VI, are shown in Figures 21 through 26. The spin rate, $\dot{\psi}$, can be closely approximated from the ψ time histories by inspection. Since preliminary calculations indicated that stable autorotations

41

could be developed for quite small initial yaw rates, the time histories illustrated are for an initial yaw rate of zero.

For the 90-degree initial angle of attack conditions, the motion resulting from a Magnus autorotative moment becomes unstable in θ for the smallest surface speed ratio, pd/2V = 0.1. The instability appears to correspond to a real root, since the oscillatory motion is well damped. The spin rate, $\dot{\psi}$, approaches - p as θ increases to near $\pi/2$, in accordance with conservation of the roll angular momentum.

For roll surface speed ratios of 0.2 and 0.3, Figures 22 and 23, the motions with Magnus autorotative moments are both statically and dynamically stable, and θ is seen to be approaching the steady-state solution as given by equation (2).

The non-Magnus autorotation initiated at α = 90 degrees and r_o = 0 is also stable, and both the θ and ψ motions rapidly approach the steady-state conditions. The apparent θ damping in the case of the non-Magnus autorotation, however, is less than in the Magnus-type autorotation, even though the damping derivatives C_{n_r} and C_{M_q} are identical in both cases. This can be explained by the coupling which exists between the rolling motion and the pitch and yaw rates in the Magnus autorotations. Although the gyroscopic pitching moment resulting from the coupling has about a 90-degree phase angle with respect to the pitch rate, the effective damping is still very great.

Another characteristic difference between the transient motion of Magnus-type autorotations, (where the Magnus force is positive), and the very slowly rolling non-Magnus autorotations, is that the initial direction of yaw rotation of the Magnus autorotation is always reversed from the steady-state direction when the spin is initiated at small or zero yaw rate. This can also be explained by the gyroscopic moments. As the body begins to pitch nose-up, due to the positive aerodynamic overturning moment, the positive q and the positive p result in a positive r and $\dot{\psi}$. This gyroscopic

effect overpowers the Magnus moment, which is in the opposite direction. When the body nose begins to pitch down, the gyroscopic moment and the Magnus moment are in the same direction, and from this point on the autorotation develops rapidly in the direction of the Magnus moment. For example, in Figure 22, we see the nose of the body moving to a positive ψ of 140 degrees before the yawing motion starts in the opposite or steady-state direction.

The transient motion of the large booster starting from an initial angle of attack of 5 degrees is shown in Figures 25 and 26. The initial body attitude is illustrated in the sketch below.
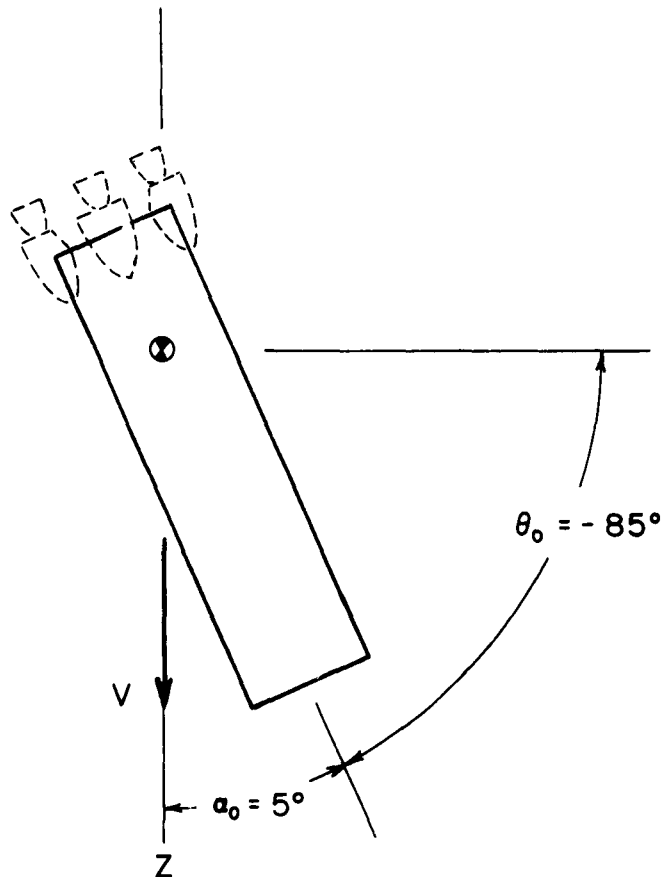
This case is somewhat more critical, since when the nose rises to $\theta = 0$, there will exist a positive $\dot{\theta}$ in addition to the aerodynamic overturning moment. This type of initiation would occur if the booster had originally been aerodynamically stable (for example, by use of stabilizing fins) and then the stabilizing fins were suddenly removed.

For autorotation initiation at $\alpha = 5$ degrees, the amplitudes of the pitch oscillations are substantially increased for both the Magnus and non-Magnus spins. However, for both types of autorotative moment the motion is found to be stable for the magnitudes of the autorotative moments investigated. A word of caution is necessary in regard to interpretation of the results for the non-Magnus autorotation. Since the fixed-plane autorotative moment, $C_{M_{z_0}}$, is assumed to be constant (a limitation which is imposed by the present six-degrees-of-freedom equations of motion), it does not represent a realistic flap system at angles of attack which are near $\alpha = 0, \pi$. Consequently, the pitch oscillations would tend to be greater for an actual flap system. In contrast, the Magnus autorotations are conservative, since the Magnus autorotative moment drops to zero at $\alpha = 0, \pi$, and at intermediate angles of attack the Magnus moment as used in the computer solutions is less than the experimental data.

Vertical Descent Trajectory and Motion at Low Altitude. The transient motion of the large booster for periods of long duration (from 20,000 feet altitude to near sea level) is illustrated in Figures 27 and 28. These figures show not only the pitching and yawing motion, but also the altitude and velocity variation with time for vertical descent. Both of the cases shown are Magnus-type autorotations and they differ in the magnitude of the initial yaw rate; the one trajectory having an initial yaw rate approximately equal to the calculated steady-state yaw rate, and the other having an initial yaw rate of only about 10 per cent of the calculated steady-state yaw rate.

Using the six-degrees-of-freedom values for velocity and altitude, the steady-state values of spin attitude, θ, and yaw rate, r, were computed from equations (1) and (2). These approximate solutions are shown in Figures 27 and 28 for comparison.

For the case of the initial yaw rate, r_o, approximately equal to the steady-state yaw rate, Figure 27, we see that the actual variation of yaw rate with time closely follows the calculated steady-state solution, but that the actual yaw rate is slightly greater in magnitude. The actual spin attitude, θ, is over-predicted by the steady-state approximation. This is due in part to the very slow response of the θ motion to the changes in velocity and air density. For example, the exact solution approaches the steady-state solution after a time lapse of about 70 seconds. The variation of descent velocity with altitude, for this case, closely follows a predicted curve for α = 90 degrees. The actual descent velocity is greater by about 10 - 15 ft/sec at all attitudes, because of the reduced drag associated with the actual spin attitude.

For the second case, where the initial yaw rate, r_o, is small, we observe overshoots in both the yaw rate and spin attitude with respect to the calculated steady-state values. The spin attitude, θ, following the overshoot, decreases to a level less than the steady-state approximation, as in the case for r_o large.

We conclude from these examples that for near equilibrium vertical descent at subsonic velocity, the linear theory provides a conservative prediction of the actual spin attitude, i. e., actual spins will tend to be flatter than estimated from the steady-state equations.

D.   RE-ENTRY STUDIES FOR LARGE BOOSTER CONFIGURATION

A booster or other vehicle re-entering the earth's atmosphere can experience several types of re-entry motion, depending upon the initial attitude and angular rates of the body. The re-entry attitude and angular rates for uncontrolled vehicles can have a large variation because at very high altitude, the aerodynamic damping is small and disturbances created earlier in the flight history, such as at separation, continue to influence the motion until re-entry. The purpose of this portion of the investigation was to compare the several types of re-entry motion and to determine, in particular, the relative effectiveness of an autorotative-type re-entry motion for mitigating the re-entry environment.

For this study, the following typical re-entry conditions were assumed for the large booster configuration:

initial velocity, V	6910 ft/sec
initial altitude	191,000 ft
initial flight path angle, γ	30 degrees below horizontal

In addition, a vertical re-entry case was considered, wherein the initial velocity was selected such that the maximum deceleration would be, theoretically, identical to the 30-degree re-entry angle case. The requirement is stated by the relationship

$$\left(\frac{\frac{dV}{dt}}{g} \right)_{max} \propto V^2 \sin \gamma$$

46

Thus for the vertical re-entry case we used

flight path angle, γ	vertical
initial altitude	191,000 ft
initial velocity, V	4875 ft/sec

Re-Entry Motions. Attention in this part of the study was devoted primarily to re-entries at large initial angle of attack, and to cases where yawing moments and yawing angular velocity exist to sustain a large angle of attack motion. Other modes of re-entry were also considered for comparison with the sustained large angle of attack motions.

If the typical large booster (Table II) re-enters in a tail-first attitude, it will stay at an angle of attack of π radians, because this is a stable trim angle for the basic center of gravity. Because at this angle of attack the booster drag is minimum, the $\alpha = \pi$ re-entry trajectory will result in the largest values of the maximum dynamic pressure, $\rho/2 \ V^2$, and the stagnation heating rate parameter $\rho^{1/2} V^3$.

If the booster re-enters at an angle of attack of 90 degrees and without roll spin or yaw rate, a tumbling motion will begin, due to the aerodynamic overturning moment. The tumbling motion will persist until an oscillation peak is attained. The body will then oscillate with decreasing amplitude, due to both the aerodynamic damping and hetero-parametric damping associated with increasing dynamic pressure. The motion will eventually damp to the stable trim point at 180 degrees angle of attack. If the booster also has a small axial spin, then the oscillations will be smaller in amplitude, but the booster will still turn around and eventually reach the 180-degrees-angle-of-attack condition. Since these tumbling re-entries, as well as the tail-first re-entry, are possible for

passive type re-entry, the motion and trajectories have been computed for comparison with autorotative-type motions, using the non-linear body-fixed six-degrees-of-freedom equations of motion.

For the development of the autorotative-type motions at supersonic velocity, it was assumed that specific values of the fixed-plane moment coefficient, $C_{M_{z_0}}$, would be attainable from a flap configuration as described in Section II. However, the use of the moment coefficient, $C_{M_{z_0}}$, for re-entry angles other than vertical does not permit an exact simulation of either a body-fixed moment, or a moment about the velocity vector. To be precise, the moment about the velocity vector for $\vec{\alpha} = 90$ degrees varies between $C_{M_{z_0}}$ and $C_{M_{z_0}} \sin \vec{\alpha}$. The same variation also occurs when a constant yaw rate about the velocity vector is transformed into the fixed-plane axes system. The primary effect of this error is to reduce the effective spin propelling moment, so that from a practical point of view, the expediency is justified from a conservative point of view. To eliminate this method of expressing the aerodynamic spin propelling moment would have required a transformation of coordinates or other program modifications which were beyond the computer capabilities.

For vertical descent, $C_{M_{z_0}}$ actually represents a body-fixed moment if we satisfy the relationship $p = -\dot{\psi} \sin \theta$. Results for this case will also be shown in a subsequent paragraph.

Re-Entry at $\gamma = 30$ Degrees. A large number of autorotative re-entry trajectories were computed for the 30-degree re-entry angle case to determine appropriate values for the initial yaw spin rate and the moment coefficient, $C_{M_{z_0}}$, and also to ascertain the effect of the overturning moment coefficient, $C_{M_{\pi/2}}$. Because the time duration

of these preliminary trajectories was restricted to about 20 seconds due to build-up of integration error (see Section IV), most of the trajectories covered only the initial phase of re-entry. However, two typical autorotative re-entry trajectories were re-initialized and extended to low supersonic and transonic velocities. These data are presented in Figures 29 and 30.

Figure 29 illustrates the variations of angle of attack, yaw rate, velocity, and altitude with time for an autorotative re-entry starting from an initial re-entry angle of attack of 90 degrees. In addition, data for the corresponding tumbling re-entry (r_o = 0 and no autorotative moment) are plotted. For both trajectories in Figure 29, the booster aerodynamic center of pressure has been moved aft such that the overturning moment is smaller than the basic value. The initial yaw spin rate is 1 rad/sec, and the autorotative moment coefficient, $C_{M_{z_0}}$, is 0.2. The complete aerodynamic characteristics are presented in Table II. At t = 50 seconds, the trajectory was re-initialized and the aerodynamic characteristics were adjusted for the ensuing transonic flight conditions.

For comparison, calculated steady-state values of yaw spin rate, r, and angle of attack, based on both the supersonic and transonic values of the stability derivatives, are plotted. In this case, the steady-state angle of attack, $\overrightarrow{a}$, is obtained by adding $\pi/2$ to θ , as given by equation (4). The steady-state solutions are also based on the six-degrees-of-freedom values for velocity and altitude.

An important characteristic of the steady-state yaw rate, as derived from the linear equations for non-Magnus spins, is that the yaw rate is directly proportional to velocity if all the aerodynamic derivatives are constant. This explains the large values of steady-state yaw rate during the initial period of re-entry where the velocity is large. The actual yaw rate as computed from the exact equations of motion does not

approach the steady-state yaw rate until the booster has decelerated to a low supersonic velocity, because the initial yaw rate in this case is small. For example, at the beginning of re-entry, the initial yaw rate is 1 rad/sec, whereas the theoretical steady-state yaw rate is about 3.4 rad/sec. Therefore, in the initial period the body has a positive angular acceleration in yaw, and the yaw rate increases slightly with time.

In the transonic and subsonic velocity range, the aerodynamic autorotative moment, $C_{M_{z_O}}$, increases and the yaw damping derivative, C_{n_r}, decreases such that the steady-state yaw rate is much greater than at the low supersonic velocities. The computed yaw rate approaches the new subsonic steady-state curve after a period of about 50 seconds from the time at which the booster decelerates through Mach number 1.0.

The calculated angle of attack history in Figure 29 also approaches the steady-state solution as given by the linear theory at low supersonic and subsonic velocities. It will be observed that the autorotative motion is quite effective in keeping the angle of attack near 90 degrees. The maximum angle of attack for this autorotative re-entry is about 120 degrees, or 30 degrees nose-up with respect to a plane normal to the trajectory.

Comparison of the pitching motion of the autorotating booster with the tumbling booster, which has no yawing motion, shows that at every instant the angle of attack is closer to 90 degrees with the autorotative motion. There is also a noteworthy difference in the angle of attack envelopes. It will be noted that the finite yaw rate at re-entry greatly reduces the initially large pitching oscillation which characterizes the tumbling re-entry. Instead, the maximum envelope in angle of attack for this type of autorotative re-entry occurs near the point of maximum dynamic pressure. In the transonic velocity range, the angle of attack envelope is very similar to that which has previously been described for vertical descent near sea level, (Figure 27).

50

The autorotative re-entry motion of the large booster has also been computed through the supersonic range for the large overturning moment case (basic center of pressure data in Table II). Motion history and trajectory data are presented in Figure 30 for both the autorotative re-entry and the corresponding tumbling re-entry. It was thought that a larger initial yaw spin rate and autorotative moment would be required for the autorotative re-entry in this case. However, for an autorotative moment coefficient, $C_{M_{z_0}}$, of 0.4, the minimum yaw spin rate investigated, 2 rad/sec, was found to be sufficient for achieving an autorotation at an angle of attack near 90 degrees. For this large overturning moment case, it can be seen that a much greater difference exists between the autorotative pitching motion and the tumbling motion. In addition, the yaw rate reduces the maximum width of the angle of attack envelope, and the greatest angle of attack oscillation is only about 18 degrees. In this example, the fixed-plane yaw rate, r, becomes very irregular as the motion progresses. This is due, primarily, to the motion of the fixed-plane coordinate system, and is not representative of the motion as it would be observed in a fixed coordinate system oriented with respect to the flight path. The irregularity in yaw rate becomes more severe when the spinning motion departs from a single plane, that is, when the angle of attack becomes other than 90 degrees.

To further determine the nature of the irregular motion resulting from use of the fixed-plane yawing moment coefficient, $C_{M_{z_0}}$, for trajectories other than vertical, some additional trajectories were attempted with the body-fixed equations of motion, using a body-fixed yawing moment coefficient. Since there was no way of satisfying the relationship $p = -\dot{\psi} \sin \theta$ continuously, the best which could be done was to estimate an average value for the roll spin rate. Using this technique, it was found that a true autorotative motion could be simulated for about 30 seconds, after which time a rapid divergence would take place due to improper roll orientation of the

spin propelling moment. For the initial period, angle of attack and yaw rate variations very similar to those shown in Figures 29 and 30 for fixed-plane autorotative moments were obtained. Consequently, it was concluded that the variations in fixed-plane yaw rate shown in Figures 29 and 30 are in actuality merely the result of the transformation of the true motion into the fixed-plane coordinates.

Vertical Re-Entry. The autorotative motion of the large booster during vertical re-entry was computed for better visualization of the characteristic pitching and yawing motions. For vertical re-entry, both the fixed-plane variables and Euler angles permit a direct physical inter-pretation of the motion. The initial conditions assumed for the vertical re-entry trajectories have been previously described.

Trajectory data for the large booster with the basic aerodynamic center of pressure (large overturning moment) are presented in Figures 31 and 32. Figure 31 illustrates the re-entry motion for an initial yaw rate of 2 rad/sec, which is identical to the yaw rate used for the comparable re-entry at γ = 30 degrees.

In great contrast to the previously described motion histories for a re-entry angle of 30 degrees, the yawing and pitching motions for vertical re-entry, as described by the fixed-plane yaw rate, r, and the Euler attitude angle, θ, are smooth, and the long period effects are clearly seen. As would be expected, close inspection shows a great deal of similarity between the vertical and γ = 30 degrees re-entry motions, if the short period motions are averaged out.

In Figure 32, the re-entry motion is illustrated for zero initial yaw spin. This result is quite significant, since it clearly shows that the initial yaw spin rate is not a definite requirement for autorotation development

52

during re-entry. However, the angle of attack is not as close to 90 degrees in this case, and large angle of attack oscillations occur at the beginning of re-entry, similar to those computed for tumbling re-entry.

The steady-state yaw spin rate and spin attitude are also shown for comparison in Figure 32. Shortly after the time of maximum deceleration, it will be noted that the yaw rate in the exact solution exceeds the steady-state yaw rate. This is in contrast to the results for re-entry at γ = 30 degrees, Figure 29, where the calculated yaw rate was always less than the steady-state yaw rate.

The exact solution for spin attitude, θ , is also less than the steady-state values of θ after the time of maximum deceleration. The difference between the steady-state θ and the calculated θ in the low velocity range, near 1000 ft/sec, is due primarily to the difference in the yaw rate. It will be recalled that the steady-state solutions for θ are approximately inversely proportional to the yaw rate squared.

Comparison of Re-Entry Environments. From re-entry to subsonic terminal descent, the primary benefit to be derived from the large angle of attack motions is a reduction in the free-stream dynamic pressure $\rho/2\ V^2$, and the stagnation heating rate parameter, $\rho^{1/2}\ V^3$. No significant reduction in the maximum re-entry deceleration is possible, because, as Allen and Eggers have shown in their linear theory (Reference 21), the maximum deceleration is dependent only upon the properties of the atmosphere, the initial re-entry velocity, and the re-entry flight path angle.

Before discussing the dynamic pressure and aerodynamic heating results, it is interesting to observe the variation of velocity with altitude for the several types of re-entry motions which have previously been discussed. Figure 33 depicts these velocity profiles for the large booster configuration and the initial conditions corresponding to the 30-degree

re-entry angle. At a specific altitude, the profile with the largest velocity is the one corresponding to the stable tail-first re-entry, as would be expected. The profiles in the intermediate velocity range are associated with tumbling re-entry. The lowest velocities are those corresponding to the autorotative re-entry motions. For all altitudes below about 70,000 feet, the autorotative re-entry velocity is less than one-half the velocity corresponding to tail-first re-entry.

The maximum dynamic pressure for steep re-entries occurs at very nearly the point of maximum deceleration. Figure 24 shows the dynamic pressure profile from several of the computed trajectories in the region of the maximum dynamic pressure. For the tail-first re-entry, the maximum dynamic pressure is 1225 lb/ft^2 at an altitude of 65,000 feet. The tumbling re-entries experience a maximum dynamic pressure which is about 75 per cent of the tail-first re-entry, and the peak is at a higher altitude. The maximum dynamic pressure for autorotative re-entry is as small as 460 lb/ft^2 at an altitude of 90,000 feet, or only about 38 per cent of the maximum dynamic pressure for a tail-first re-entry.

The stagnation heating rate of a rounded body is very nearly proportional to $\rho^{1/2} V^3$. This parameter, calculated for ρ and V with units of lb-sec^2/ft^4 and ft/sec, respectively, is plotted in Figure 35 for several of the re-entry trajectories which were initiated at the 30-degree re-entry angle conditions. For tail-first re-entry, the parameter has a maximum value of 14.0×10^8, whereas for autorotative re-entry, a value of only 8.9×10^8 is indicated. Thus, a significant reduction in both the maximum stagnation heating rate and the total heat input is achieved with the large angle of attack re-entry.

The reader must be cautioned that the results which have just been discussed are applicable only to the particular booster which has been investigated. For example, the ratio of $C_D S$ at 90 degrees angle of

attack to the $C_D S$ at 180 degrees angle of attack is 6.2 for the large booster considered here. For other configurations, drag ratios, and re-entry conditions, different results could be expected. The objective here is only to present a typical example, and to show quantitatively the influence of large angle of attack motions on the descent trajectory and the vehicle environment.

VII. CONCLUSIONS AND RECOMMENDATIONS

A. CONCLUSIONS

1. The near steady-state autorotative motion of either rapidly or slowly rolling quasi-axi-symmetric bodies can be accurately predicted by the linear theory developed from the two-moment equations of motion in a fixed-plane coordinate system, provided that the aerodynamic moments at large angle of attack are correctly described. Linear solutions for θ and r have been found to agree within about one percent with exact motion histories computed by numerical integration of the six-degrees-of-freedom equations of motion, and the frequency and damping of the computed motion histories are in close agreement with the approximate roots of the characteristic equation of the linear system.

2. Autorotations which are sustained by the aerodynamic Magnus moment will be limited to subsonic descent velocities, because the aerodynamic Magnus force at transonic and supersonic Mach numbers is insufficient to satisfy the static stability requirements for a stable autorotation.

At subsonic velocities the roll surface speed ratio, pd/2V, required for a Magnus-type autorotation at near 90 degrees angle of attack, was found to be less than about 0.3 for all cases examined. Since roll surface speed ratios in excess of 0.3 have been achieved with aerodynamic rotor systems, it will be possible to develop Magnus-type autorotations by aerodynamic means alone.

3.   Autorotations can be achieved by the use of a body-fixed flap located approximately 90 degrees from the stagnation line, if the body rolls such that the same side of the body is always directed toward the airstream. The characteristics of this type autorotation can be approximated by introduction of a fixed-plane moment coefficient, $C_{M_{z_o}}$, into the linearized or six-degrees-of-freedom equations of motion. This concept can be applied to both supersonic and subsonic flight velocities because the yawing moment due to a flap can be appreciable, even at supersonic Mach numbers. The use of flap-type appendages for producing an autorotative moment has an additional advantage in that the cross drag coefficient can be greatly increased at the supercritical Reynolds numbers encountered at terminal descent velocities.

4.   The aerodynamic moment derivatives due to rolling and yawing motions are extremely significant in determining the steady-state auto-rotation rate and attitude, as well as the stability of the motion at angles of attack near 90 degrees. Strip theory can be used to evaluate the two most important derivatives, C_{n_r} and $C_{M_{pr}}$. These derivatives are non-linear, both with respect to the angle of attack, and the magnitude of the yaw rate.

5.   It is possible to develop large angle of attack autorotative motions even though the initial yaw rate and the autorotative moment are small and the overturning moment in the pitch plane is large. This para-doxial phenomena can be explained by the fact that only a small yawing moment is required to obtain a large $\dot{\psi}$, which in turn provides a large inertial pitching moment, $I \, \dot{\psi}^2 \cos \theta \sin \theta$, which opposes the aero-dynamic overturning moment.

It is possible to initiate autorotative motions at small angle of attack if the body has an unstable aerodynamic pitching moment which will rotate the body to large angle of attack. For rolling bodies (Magnus-type autorotations), the transient motion from small angle of attack is very complex, since it is possible for both the gyroscopic moment and Magnus moment to be either positive or negative.

6. The autorotative recovery of a large booster configuration is shown to be feasible. It is possible to initiate an autorotative yawing motion at re-entry if the initial angle of attack is near 90 degrees. In most instances no initial yaw spin rate will be required if the autorotative moment coefficient is at least one-tenth of the overturning moment coefficient. Both the maximum dynamic pressure and maximum stagnation heating rate are significantly reduced by a large angle of attack re-entry. The terminal descent velocity of the large booster configuration examined was sufficiently small that the residual energy could be absorbed efficiently for a body weight penalty of only about 5 percent of the vehicle basic weight.

B. RECOMMENDATIONS

1. The transient autorotative motion of aerodynamically unstable bodies with flap and roll vanes should be investigated further, because these configurations more nearly represent practicable recovery systems. These investigations will require expansion of the six-degrees-of-freedom equations of motion to include the aerodynamic stability derivatives in roll, yaw, and pitch, which result from the addition of appendages.

2.   The present six-degrees-of-freedom trajectory program should be re-programmed for a computer with larger data storage capacity.   This will allow the addition of new stability derivatives and will permit the inclusion of a quaternion normalization scheme, such that long duration trajectories and motion histories can be calculated more efficiently.

3.   Subsonic wind tunnel tests at large Reynolds numbers should be made to evaluate the drag, yawing moment, and Magnus moment of finite length cylinders with flaps and rotors.   Dynamic tests should be conducted with quasi-cylindrical-shaped models free to pitch, yaw, and roll, such that the damping derivatives at large angle of attack can be measured.

4.   Free-flight model tests should be made at large Reynolds numbers to allow comparison of model motions with the developed theory.

LIST OF REFERENCES

1. Brunk, J. E., W. L. Davidson, and R. W. Rakestraw, "The Dynamics of Spinning Bodies at Large Angle of Attack," AFOSR/DRA-62-3, January 1962.

2. Brunk, James E., "Autorotative Missile and Booster Recovery," Institute of Aerospace Sciences, S. M. F. Fund Paper No. FF-34, January 1963.

3. Polhamus, Edward C., "Effect of Flow Incidence and Reynolds Number on Low-Speed Aerodynamic Characteristics of Several Noncircular Cylinders with Applications to Directional Stability and Spinning," NACA TN 4176, January 1958.

4. Kelly, Howard R., and Ray W. Van Aken, "The Magnus Force on Spinning Cylinders," I. A. S. Preprint No. 712, January 1957.

5. Loptien, George W., "An Investigation of Cone-Cylinder Bodies in the Steady State Spin Mode and Magnus Force Effects on a Cone-Cylinder Body," WADD TN 60-76, August 1960.

6. Gross, Donald S., "Wind Tunnel Tests of Rotating Bodies, 5th Series," University of Maryland Wind Tunnel Report No. 116, May 1954.

7. Cook, Martin L., "Magnus Force and Moments on a Quasi-Cylindrical Rotating Body with the Axis of Rotation Perpendicular to the Airstream," David W. Taylor Model Basin Report, AERO 1006, August 1961, (Confidential).

8. Hauer, Herbert J., and Howard R. Kelly, "The Subsonic Aerodynamic Characteristics of Spinning Cone-Cylinders and Ogive-Cylinders at Large Angles of Attack," NAVORD Report 3529, July 1955.

9. Sieron, Thomas R., "On the 'Magnus Effects' of an Inclined Spinning Shell at Subsonic and Transonic Speeds," WADD Technical Report 60-212, April 1961.

10. Platou, A. S., "The Magnus Force on a Rotating Cylinder in Transonic Cross Flow," BRL Report 1150, September 1961.

11. Lockwood, Vernard E., and Linwood W. McKinney, "Effect of Reynolds Number on the Force and Pressure Distribution Characteristics of a Two-Dimensional Lifting Circular Cylinder," NASA TN D-455, September 1960.

12. Lockwood, Vernard E., and Linwood W. McKinney, "Lift and Drag Characteristics at Subsonic Speeds and at a Mach Number of 1.9 of a Lifting Circular Cylinder with a Fineness Ratio of 10," NASA TN D-170, December 1959.

13. Murphy, Charles H., and John D. Nicolaides, "A Generalized Ballistic Force System," BRL Report No. 933, May 1955.

14. Jorgensen, Leland H., and Stuart L. Treon, "Measured and Estimated Aerodynamic Characteristics for a Model of a Rocket Booster at Mach Numbers from 0.6 to 4 and at Angles of Attack from 0° to 180°," NASA TM X-580, September 1961, (Confidential).

15. McKinney, Linwood W., "Effect of Fineness Ratio and Reynolds Number on the Low-Speed Crosswind Drag Characteristics of Circular and Modified-Square Cylinders," NASA TN D-540, October 1960.

16. Crogan, Leonard E., "Drag and Stability Data Obtained from Free-Flight Range Firings Within the Mach Number Range of 0.4 to 3.0 for Several Cylindrical Configurations," NAVORD Report 6731, October 1960.

17. Gowen, Forrest E., and Edward W. Perkins, "Drag of Circular Cylinders for a Wide Range of Reynolds Numbers and Mach Numbers," NACA TN 2960, June 1953.

18. Allen, Julian H., and Edward W. Perkins, "A Study of Effects of Viscosity on Flow Over Slender Inclined Bodies of Revolution," NACA R-1048, 1951.

19. Robinson, Alfred C., and Corrado R. Poli, "Development of Normalized Six-Degree-of-Freedom Equations for Analog Simulation of Atmospheric Re-Entry," Aeronautical Systems Division Report ASD TR 61-448, November 1961.

20. Klinar, Walter J., and William D. Grantham, "Investigation of the Stability of Very Flat Spins and Analysis of Effects of Applying Various Moments Utilizing the Three Moment Equations of Motion," NASA MEMO 5-25-59L, June 1959.

21. Allen, Julian H., and A.J. Eggers, Jr., "A Study of the Motion and Aerodynamic Heating of Ballistic Missiles Entering the Earth's Atmosphere at High Supersonic Speeds," NACA Report 1381, 1958.

22. Nicolaides, John D., and Leonard C. MacAllister, "A Review of Aeroballistic Range Research on Winged and/or Finned Missiles," Ballistic Technical Note No. 5, 1955.

BODY CHARACTERISTICS
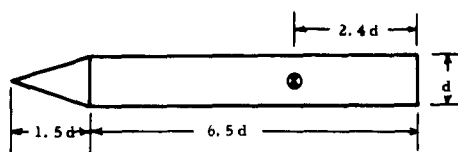
$$\text{mass} = 0.407 \text{ slugs} \qquad S_{ref} = 0.1963 \text{ ft}^2$$

$$I_x = 0.02115 \text{ slug-ft}^2 \qquad d_{ref} = 0.5 \text{ ft}$$

$$I = 0.5430 \text{ slug-ft}^2$$

AERODYNAMIC CHARACTERISTICS

	Case		
	1	2, 3	4
C_{x_0}	-0.67	-0.67	-0.67
C_{x_2}	0.54	0.54	0.54
$C_{N\vec{\alpha}_0}$	7.55	3.00	1.70
$C_{N\vec{\alpha}_2}$	-1.25	-0.50	-0.28
$C_{N\vec{\alpha}_4}$	0.057	0.023	0.013
$C_{Np\vec{\alpha}_0}$	13.87	-36.98	29.59
$C_{Np\vec{\alpha}_2}$	-2.30	6.13	-4.90
$C_{Np\vec{\alpha}_4}$	0.105	-0.279	0.223
$C_{n_r} = C_{M_q}$	-51.6	-38.6	-28.6
$C_{M\vec{\alpha}_0} = C_{M_{\pi/2}}$	9.42	3.75	2.12
$C_{M\vec{\alpha}_2}$	-1.56	-0.621	-0.351
$C_{M\vec{\alpha}_4}$	0.071	0.028	0.016
$C_{Mp\vec{\alpha}_0} = C_{Mp\frac{\pi}{2}}$	14.14	-37.5	30.1
$C_{Mp\vec{\alpha}_2}$	-2.34	6.21	-4.98
$C_{Mp\vec{\alpha}_4}$	0.107	-0.28	0.227
C_{Mpr}	0	0	0
R	1.2×10^5	4×10^5	5×10^5

TABLE I.   BODY PHYSICAL AND AERODYNAMIC CHARACTERISTICS, FINENESS-RATIO-EIGHT CONE-CYLINDER
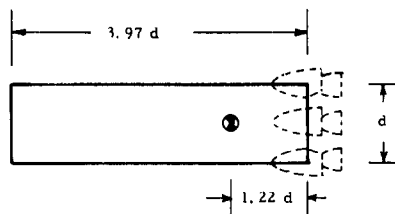
$mass = 9580$ slugs

$I_x = 1,700,000$ slug-ft^2

$I = 17,000,000$ slug-ft^2

$S_{ref} = 855.3$ ft^2

$d_{ref} = 33$ ft

AERODYNAMIC CHARACTERISTICS

	Subsonic Basic C. P.	Transonic Modified C. P.	Supersonic Basic C. P.	Supersonic Modified C. P.
C_{X_0}	- 0.64	- 1.085	- 1.06	- 1.06
C_{X_2}	0.259	0.304	0.418	0.418
$C_{N\vec{\alpha}_0}$	7.000	5.715	6.570	6.570
$C_{N\vec{\alpha}_2}$	- 1.145	- 0.935	- 1.075	- 1.075
$C_{N\vec{\alpha}_4}$	0.0471	0.0384	0.0442	0.0442
$\mu_{N\vec{\alpha}}, \mu_{M\vec{\alpha}}$	0	3.66	0	0
$C_{Np\vec{\alpha}_0}$	13.15	0	0.20	0.20
$C_{Np\vec{\alpha}_2}$	- 2.151	0	- 0.033	- 0.033
$C_{Np\vec{\alpha}_4}$	0.0884	0	0.0014	0.0014
$C_{M\vec{\alpha}_0}$	7.796	1.687	5.976	1.039
$C_{M\vec{\alpha}_2}$	- 2.024	- 0.633	- 1.297	- 0.302
$C_{M\vec{\alpha}_4}$	0.1375	0.0468	0.07	0.020
$C_{Mp\vec{\alpha}_0}$	10.06	0	0.155	0.155
$C_{Mp\vec{\alpha}_2}$	- 1.646	0	- 0.025	- 0.025
$C_{Mp\vec{\alpha}_4}$	0.0676	0	0.0010	0.0010
C_{M_q}	- 28.2	- 27.6	- 50.0	- 50.0
$C_{n_{r_0}}$	- 14.1	13.8	- 25.0	- 25.0
$C_{n_{r_2}}$	-150.5	-150.5	-266.0	-266.0
C_{Mpr}	- 15.0	0		
$C_{M_{z_0}}$	- 3.02 †	0.76	0.4	0.2
$C_{M_{\pi/2}}$	4.45, 5.35*	0.65	5.1	0.65
$C_{Mp_{\pi/2}}$	10.06			

† single flap length of 0.8 diameter
* used only for comparisons with the six-degrees-of-freedom trajectories

TABLE II. PHYSICAL AND AERODYNAMIC CHARACTERISTICS, TYPICAL LARGE BOOSTER

TYPE OF AUTOROTATION	AUTOROTATION ATTITUDE - DEG	
	Small Body	Large Body
Magnus	9. 5	20. 0
Slowly Rolling with Body-Fixed Strakes	0. 7	4. 9

TABLE III.

AUTOROTATION ATTITUDE FOR LARGE AND SMALL BODIES

	Case 1	Case 2	Case 3	Case 4
Altitude - ft	54, 800	S. L.	S. L.	15, 200
Vertical Velocity - ft/sec	246	126	126	229
Roll Rate, p - rad/sec	98. 3	50. 4	50. 4	91. 7
Surface Speed Ratio - pd/2V	0. 1	0. 1	0. 1	0. 1
Initial Yaw Rate, r - rad/sec	-26. 6	0	51. 0	-96. 25
Initial Attitude, θ - deg	9. 36	0	0	2. 00
Initial Pitch Rate, q - rad/sec	0	0	0	0

TABLE IV.   INITIAL CONDITIONS

FOR INVESTIGATION OF TRANSIENT MOTION

OF CONE-CYLINDER BODY

Case	$r/r_{\text{steady-state}}$	Roots	Exact	Approximation Equations	Damping & Frequency Calculated From Motion Histories
1	1.0	λ_1	-0.0842	-0.0840	not measurable
		$\lambda_{2,3}$	-0.0434 ± i27.06	-0.0420 ± i26.60	-0.042 ± i26.9
2	0.6	λ_1			-0.264
		$\lambda_{2,3}$			-0.263 ± i31.2
3	1.0	λ_1	-0.2933	-0.2935	-0.24
		$\lambda_{2,3}$	-0.1469 ± i51.02	-0.1468 ± i51.00	-0.158 ± i51.0

TABLE V.   CHARACTERISTIC ROOTS FOR THE BASIC BODY CONFIGURATION FOR AUTOROTATION CONDITIONS, CASES 1, 2, AND 3

INVESTIGATIONS	INITIAL CONDITIONS	
	Magnus Autorotative Moment	Flap Autorotative Moment
Investigation of Initial Stability		
$r_o = 0$ $\qquad \alpha_o = 90°$	$pd/2V = .3$	$p_o = 0$ $\qquad C_{M_{z_o}} = -3.02$
	" .2	
	" .1	
$r_o = 0$ $\qquad \alpha_o = 5°$	$pd/2V = .3$	$p_o = 0$ $\qquad C_{M_{z_o}} = -3.02$
Investigation of Descent Trajectory		
$r_o = -.394$ rad/sec $\qquad \alpha_o = 90°$	$pd/2V = .3$	
$r_o = -3.15$ rad/sec $\qquad \alpha_o = 90°$	$pd/2V = .3$	

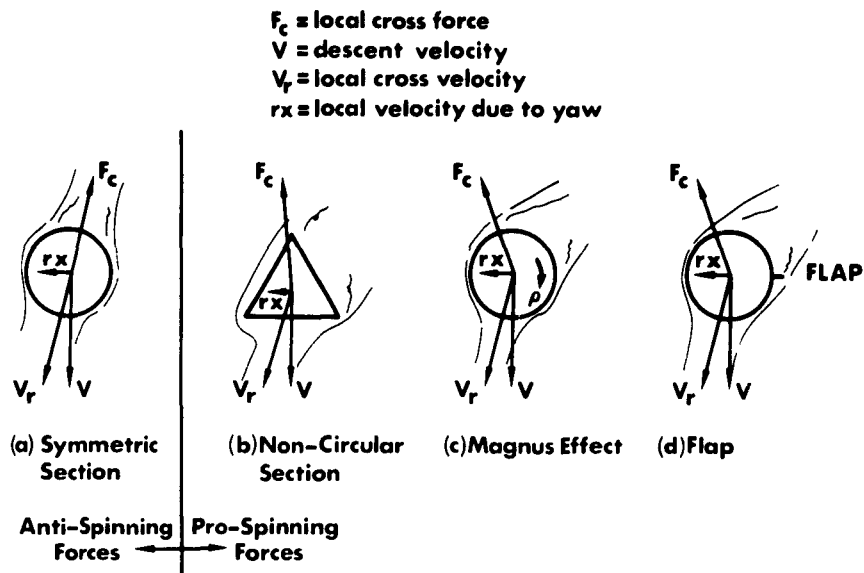**TABLE VI.   INITIAL CONDITIONS FOR INVESTIGATION OF TRANSIENT MOTION OF LARGE BOOSTER AT LOW ALTITUDE**

66

F_c = local cross force
V = descent velocity
V_r = local cross velocity
rx = local velocity due to yaw

(a) Symmetric Section

(b) Non-Circular Section

(c) Magnus Effect

(d) Flap

Anti-Spinning Forces ◄────────► Pro-Spinning Forces

Figure 1. Aerodynamic Force Mechanisms for Autorotative Moments

$R = 1,000,000$

C_y
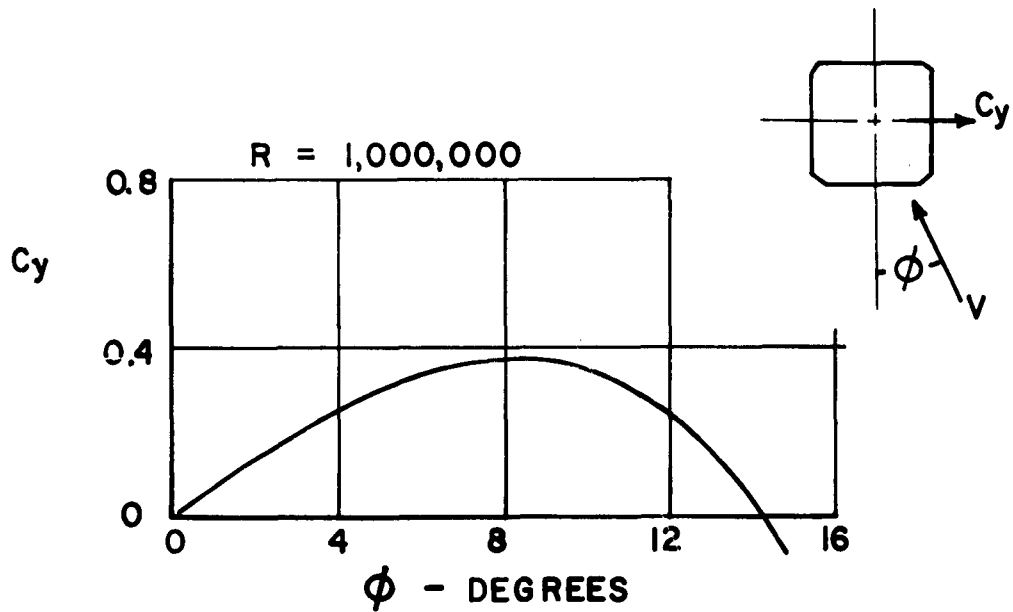
Figure 2. Effect of Flow Incidence on the Side Force of a Non-Circular Cylinder

67

	Fineness Ratio	R	Ref.
————	Two Dimensional	1,000,000	4
— —	7	770,000	8
—·—	4.8	650,000	7
- - - - - -	4.8 *	650,000	7
□	4.0 **	750,000	6

* with four low-aspect-ratio fins
** with nine-rib full-span rotor
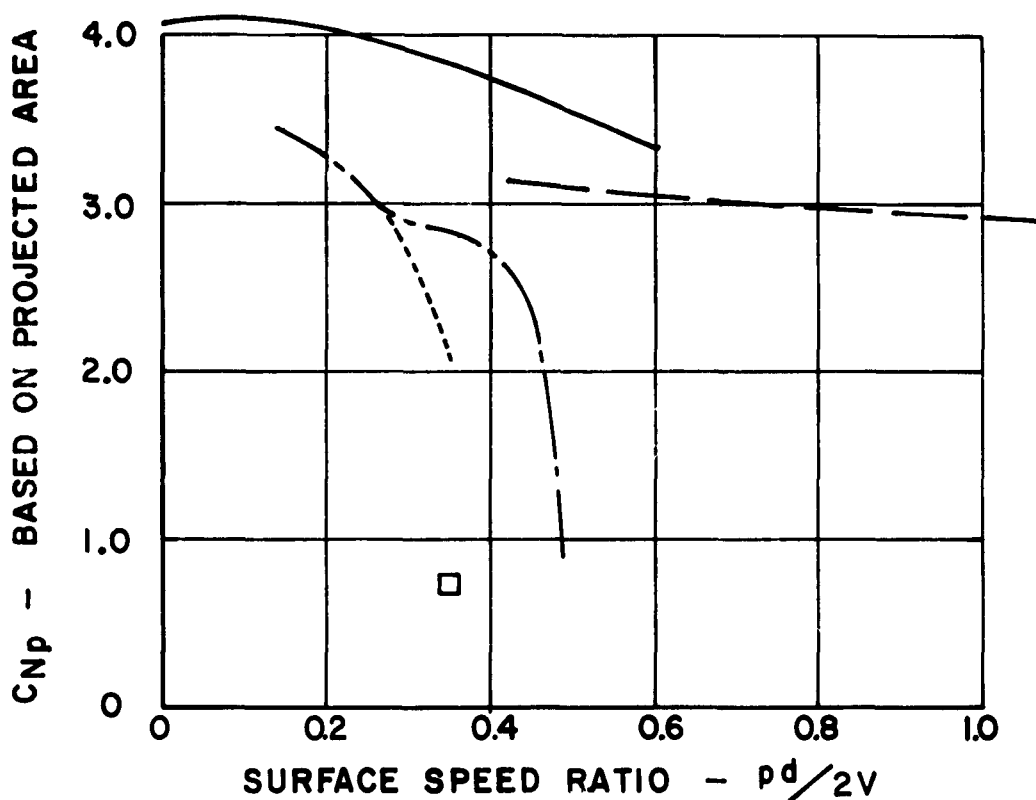
Figure 3.   Correlation of the Subsonic Magnus Force on Finite-Length
Cylinders with the Axis of Spin Normal to the Flow

68

Fineness Ratio	$R \times 10^{-5}$	Ref.
7	7.7	8
3.9	3.3	9
3.9	4.4	9
▢ Two Dimensional	6.0	4
○ Two Dimensional	0.7−1.85	10
△ Two Dimensional	1.0−2.5	10
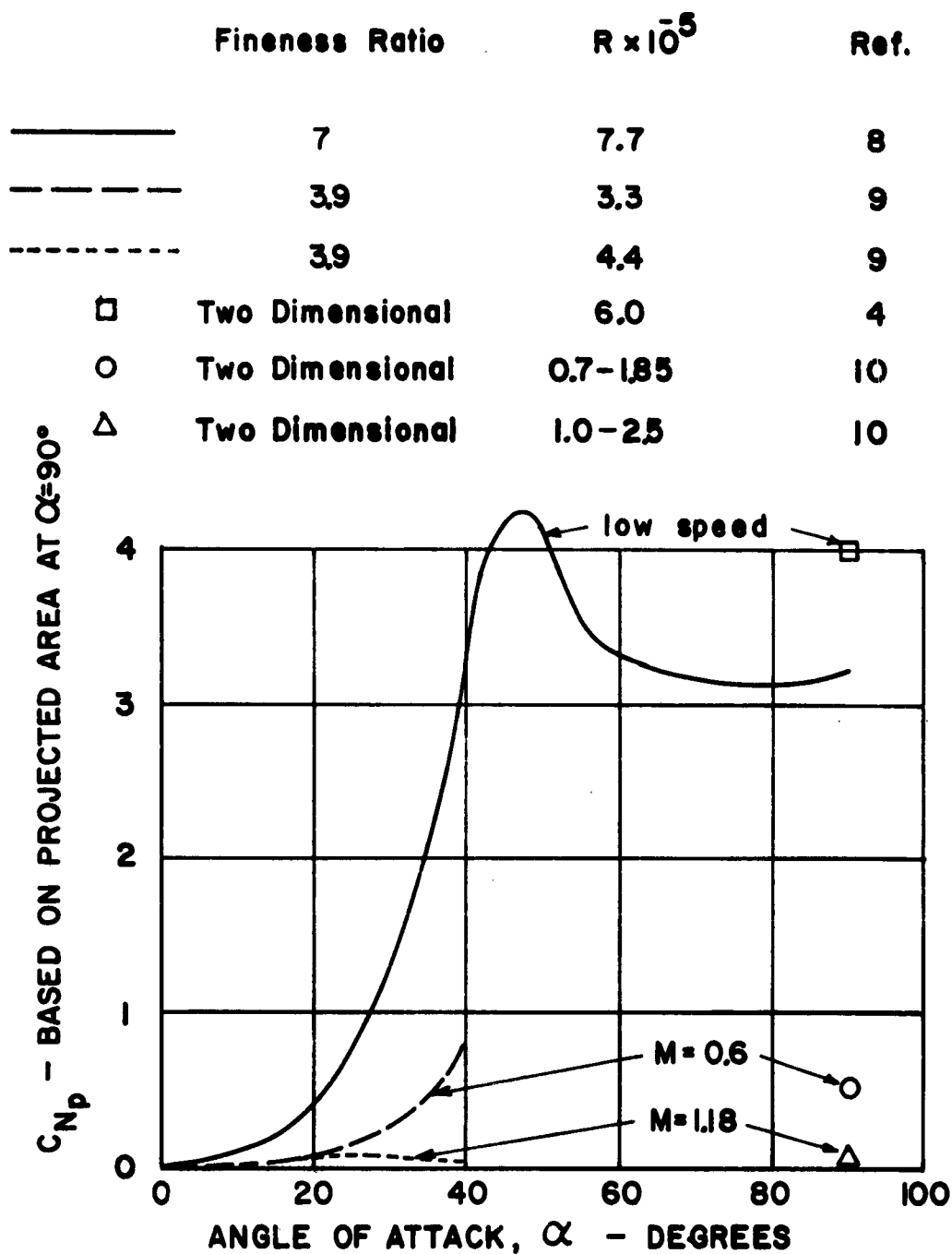
Figure 4.   Correlation of the Magnus Force on Inclined Spinning Cylinders at Subsonic and Transonic Mach Numbers

69
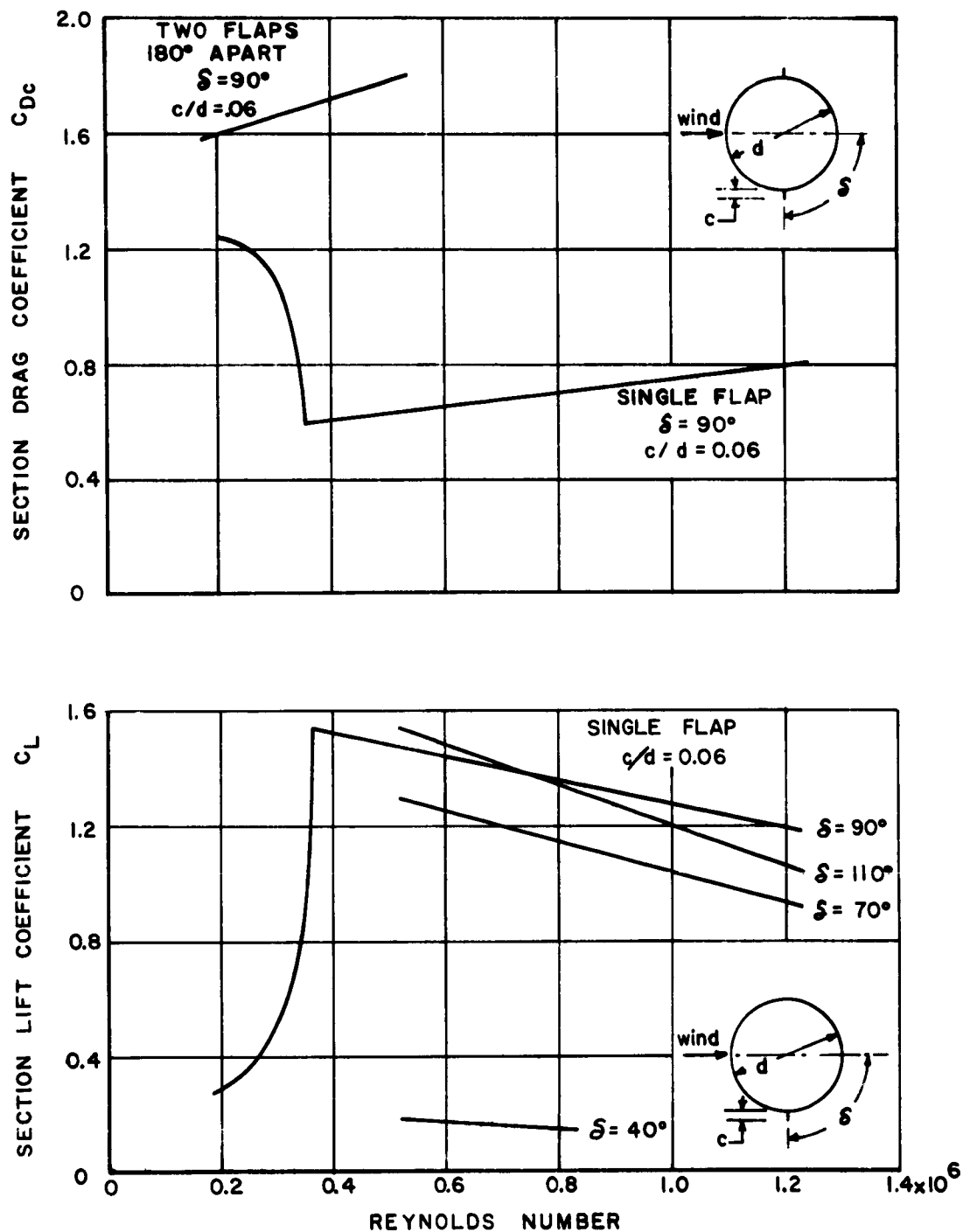
Figure 5.   Effect of Reynolds Number and Flap Position on the Aerodynamic
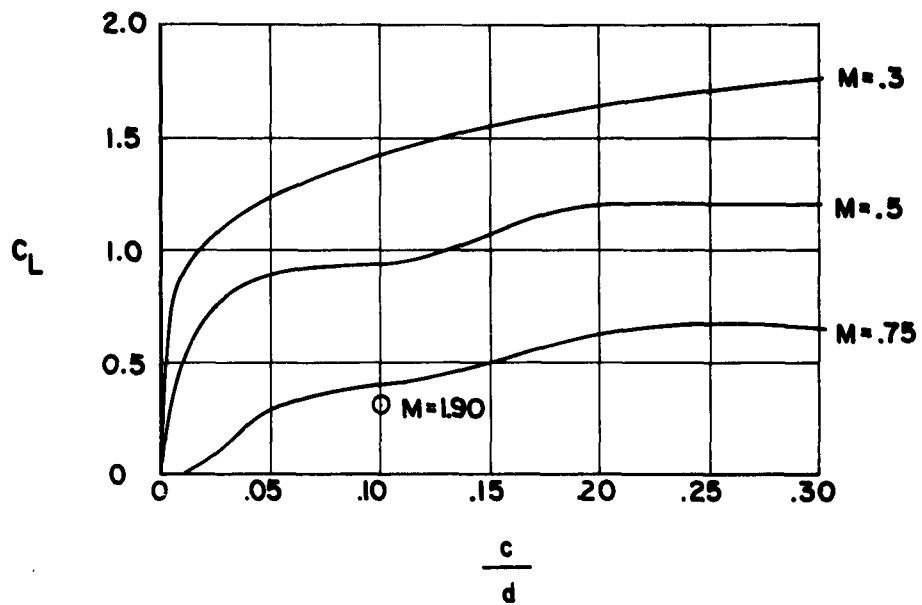Characteristics of a Two-Dimensional Lifting Cylinder

Figure 6. Effect of Flap Chord and Mach Number on the Lift
Characteristics of a Circular Cylinder, $\delta = 90°$
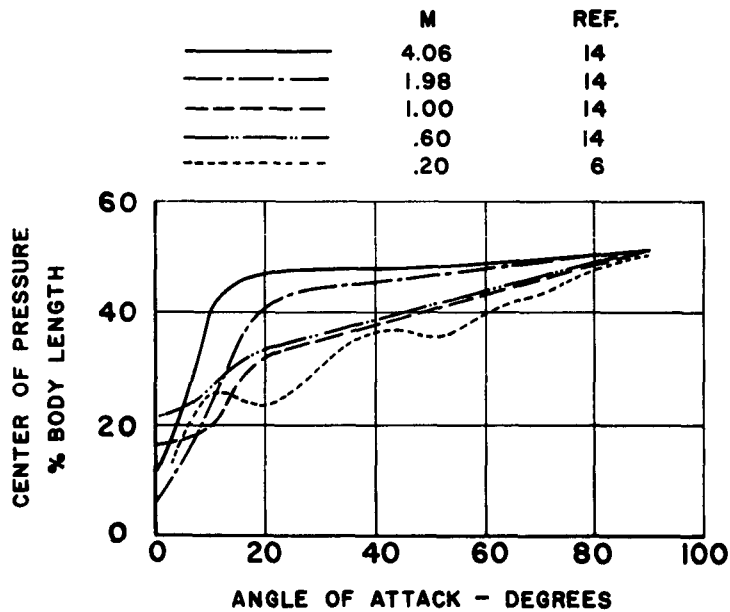
Figure 7. Effect of Angle of Attack and Mach Number on the Normal
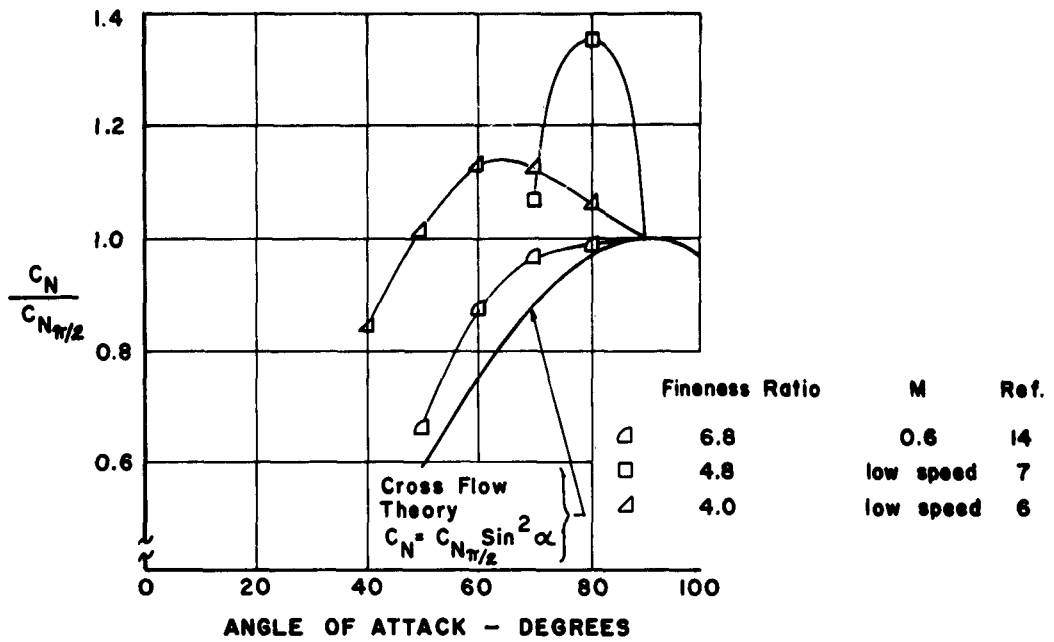Force Center of Pressure of Flat-Ended Cylinders

Figure 8.   Effect of Angle of Attack on the Subsonic
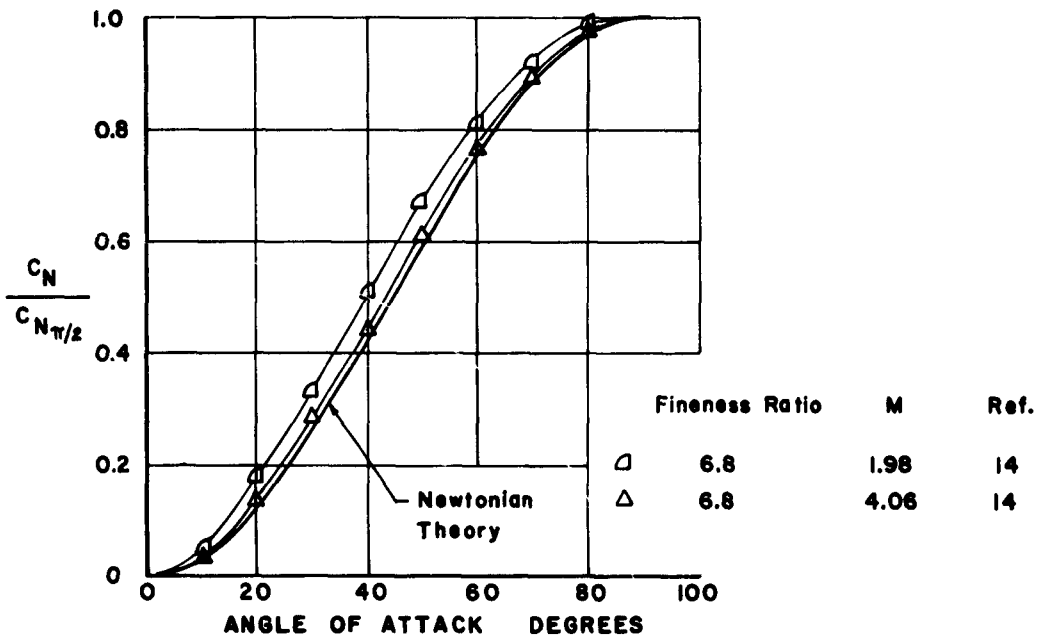   Normal Force of Flat-Ended Cylinders

Figure 9.   Effect of Angle of Attack on the Supersonic
             Normal Force of Flat-Ended Cylinders

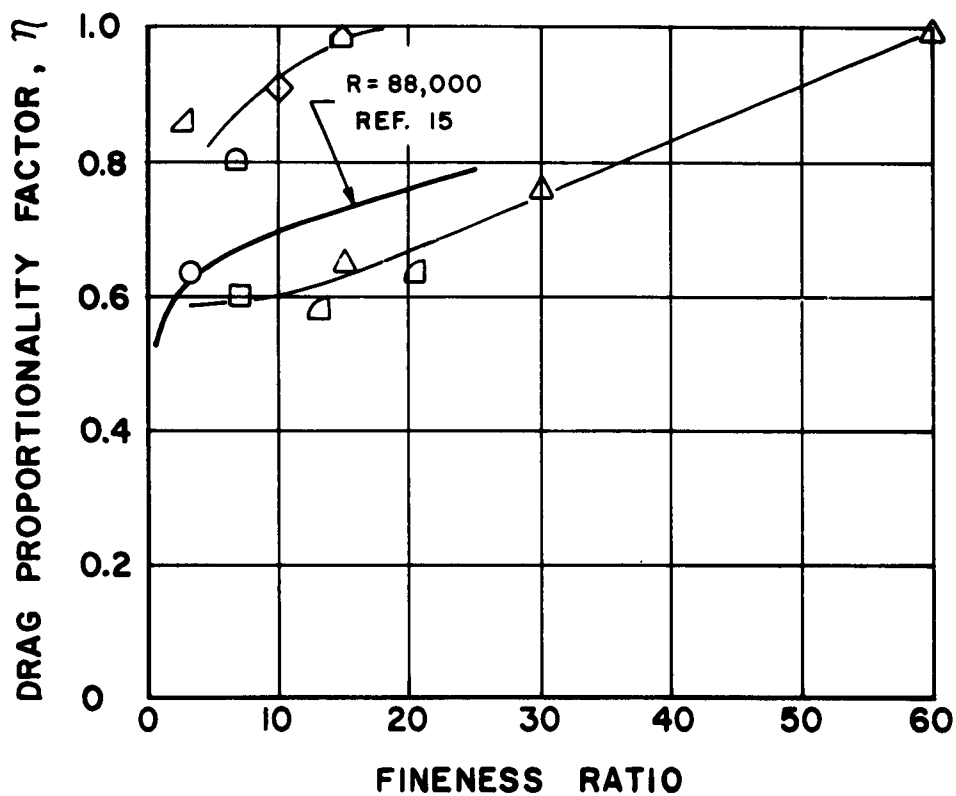|	M	REF.
O	0.6	16
□	0.6	14
◇	0.6	12
△	0.6	17
⌁	0.6	18
◿	1.2	16
◖	1.2	14
△	1.2	17

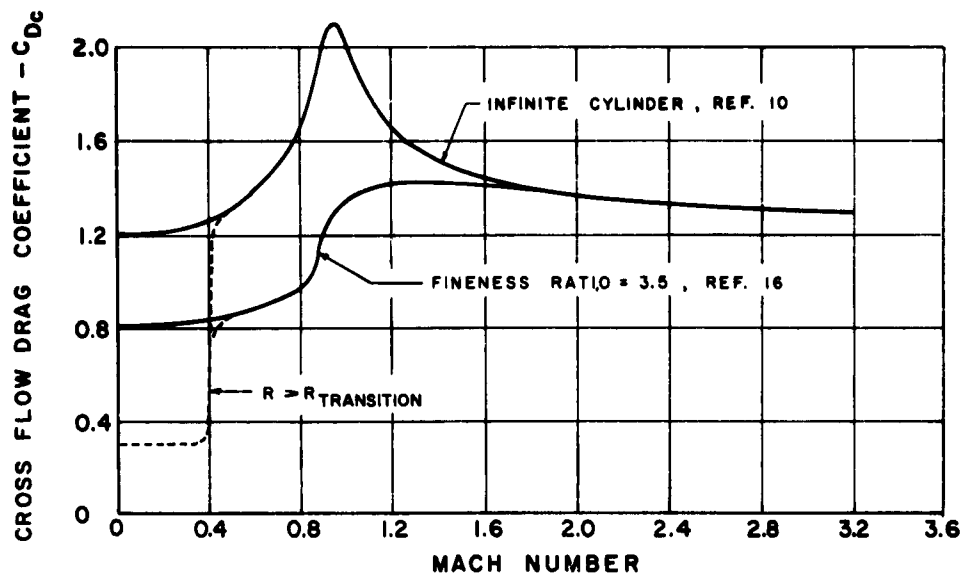Figure 10.   Effect of Fineness Ratio on the Finite-Length to Infinite-Length-Cylinder Drag Coefficient Ratios

Figure 11.   Cross Flow Drag Coefficients for Finite-Length
and Infinite-Length Circular Cylinders
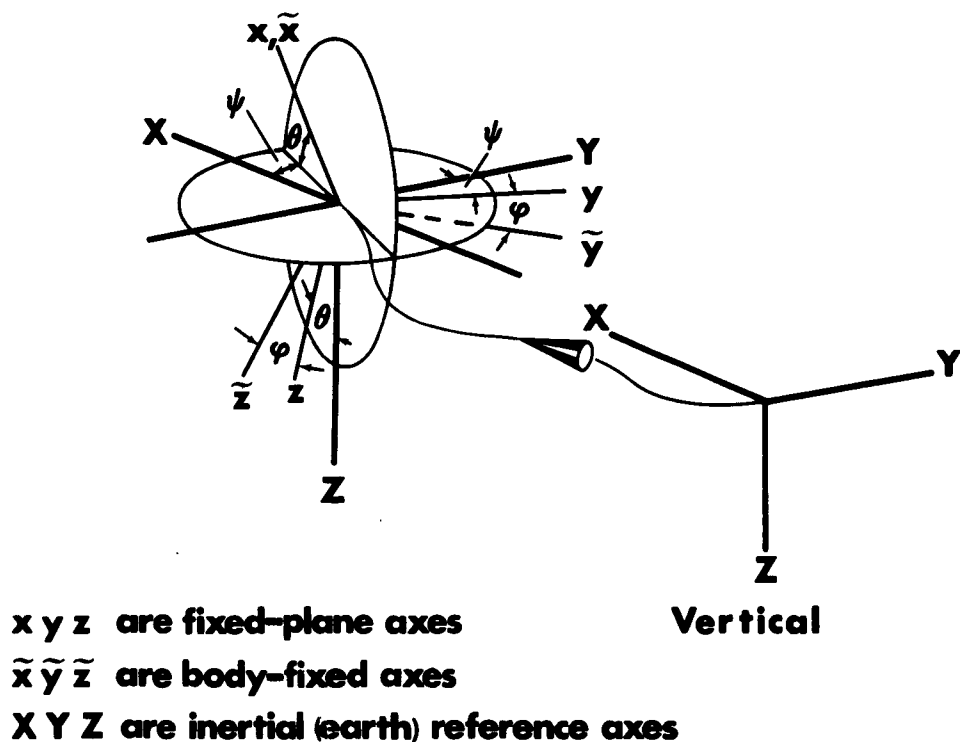as a Function of Mach Number

x y z are fixed-plane axes

x̃ ỹ z̃ are body-fixed axes

X Y Z are inertial (earth) reference axes

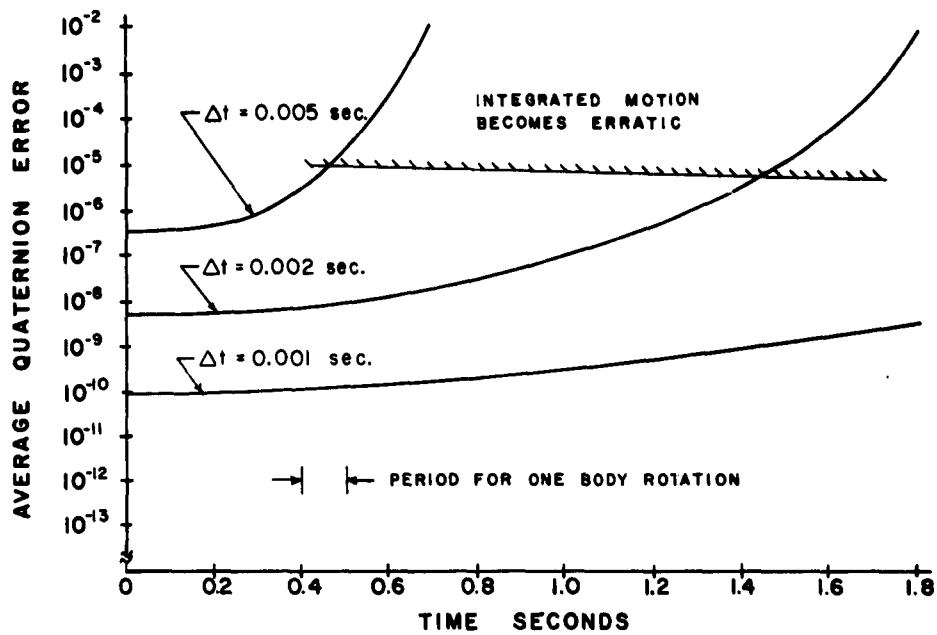Figure 12.   Coordinate Axes for Equations of Motion

74

Figure 13.   Effect of Integration Time and Integration Time Interval
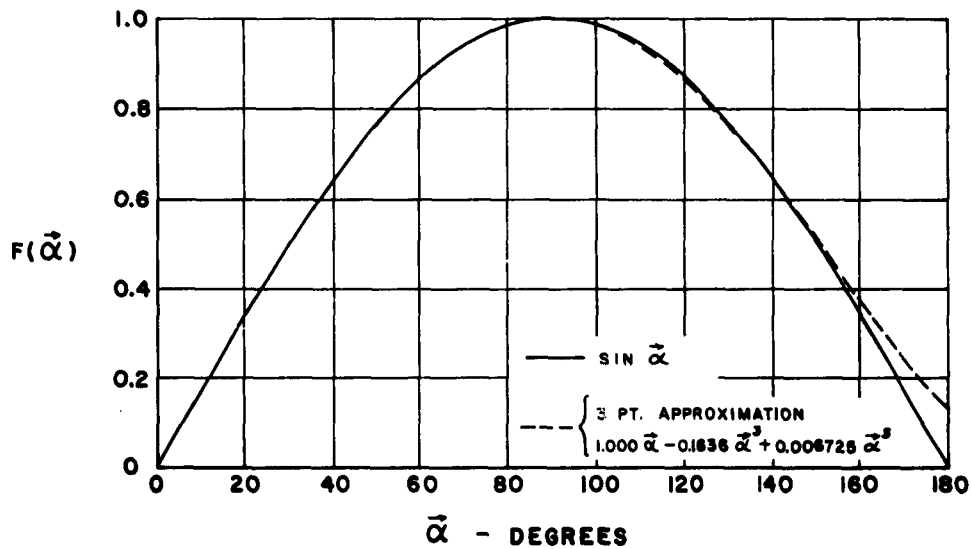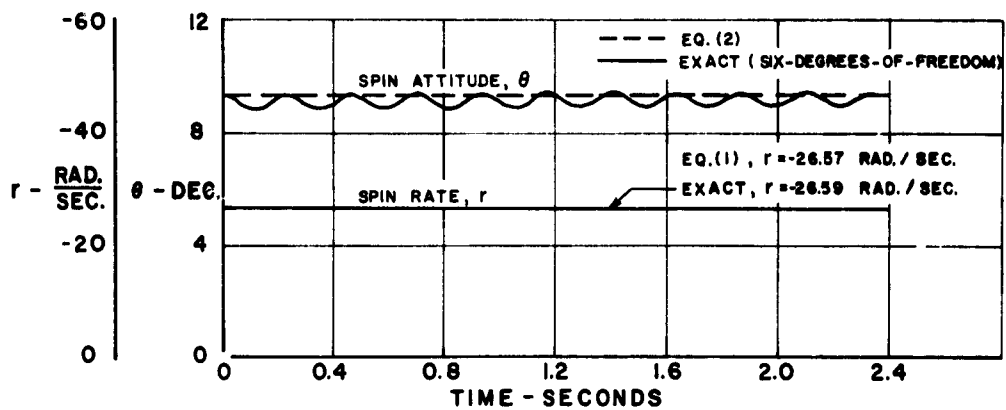on Average Quaternion Error for a Typical Trajectory
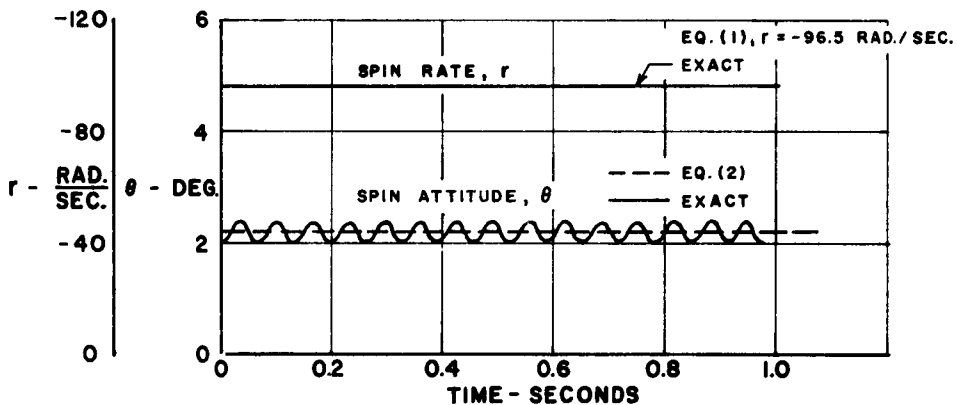

Figure 14.   Power Series Approximation of Sin $\vec{\alpha}$
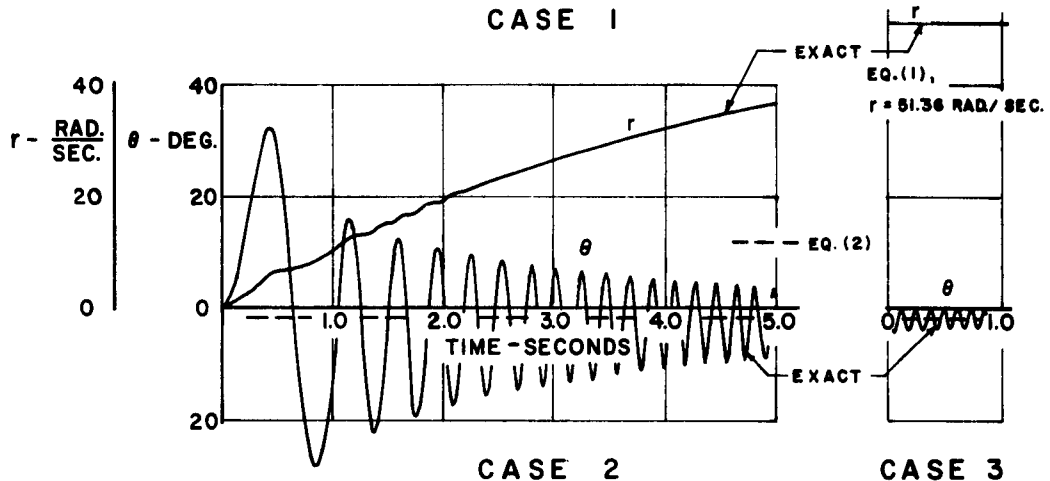
Figure 15. Approximate and Exact Six-Degrees-of-Freedom
Solutions for θ and r for a Cone-Cylinder Body
at Near-Steady-State Autorotation

76
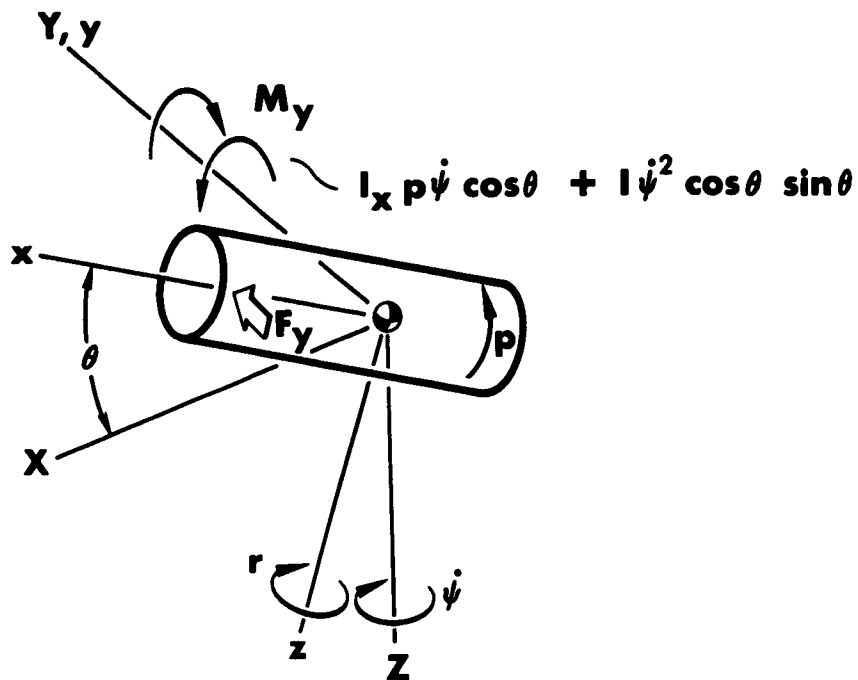
XY Plane Horizontal
y axis non-rolling, i.e., always horizontal

Figure 16.   Simplified Force Diagram for Autorotative
             Motion of a Rolling and Yawing Body
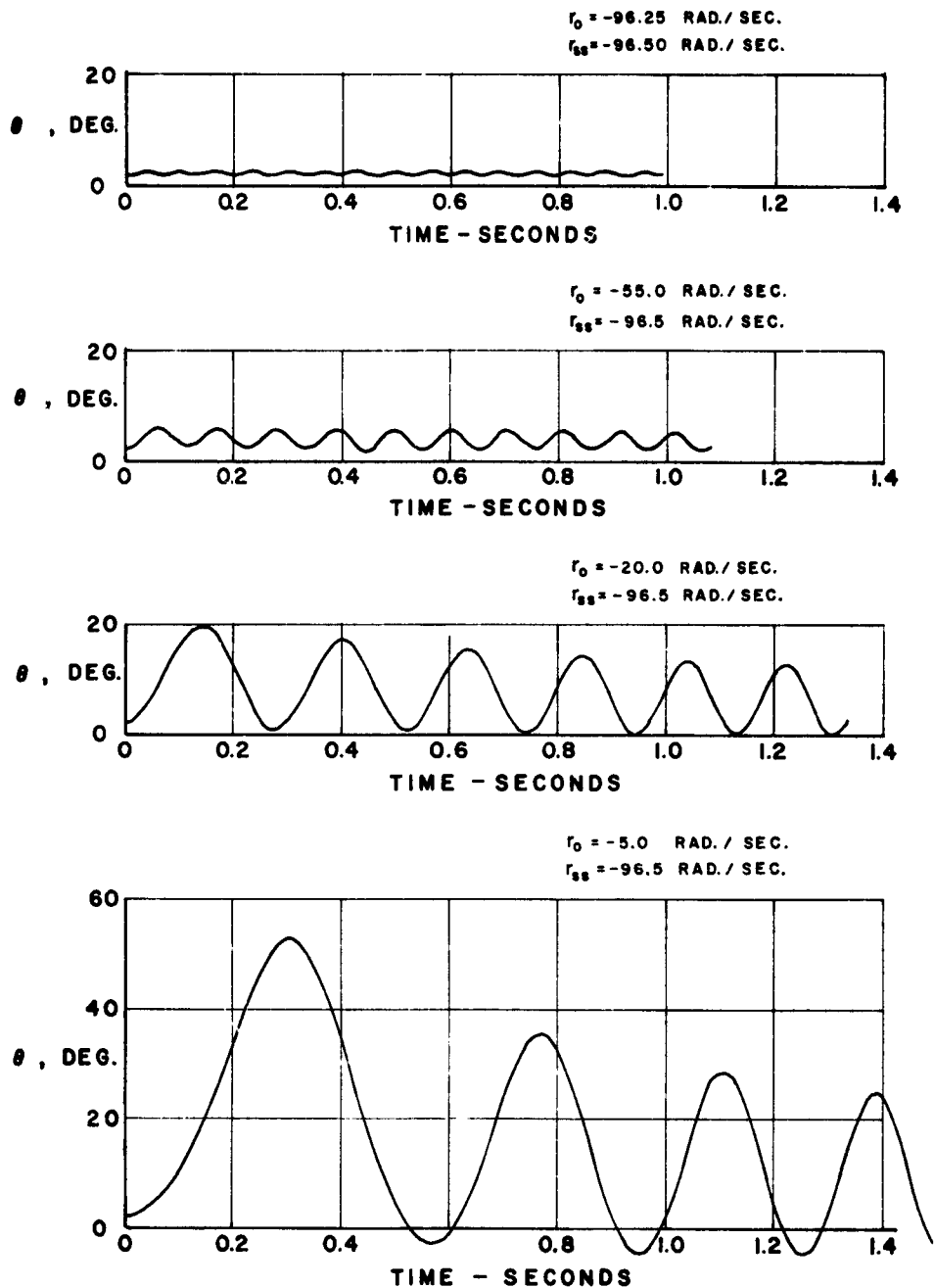
Figure 17.   Transient Pitching Motion of a Cone-Cylinder Body in Vertical
Descent for Various Initial Fixed-Plane Yaw Rates

78

VELOCITY   229 FT. / SEC.

ALTITUDE   15,200 FT.

Body Physical & Aerodynamic
Characteristics —Table I , Case 4

ROLL RATE , p   RAD. / SEC.

91.8   (p d / 2V = 0.10)
45.9   (p d / 2V = 0.05)
22.9   (p d / 2V = 0.025)

STEADY—STATE
YAW RATE

INITIAL YAW RATE , r_0 — RAD. / SEC.

$|\theta_{MAX}|$ — DEGREES

Figure 18.   Effect of Initial Yaw Rate and Roll Rate on the Maximum
                  Pitch Attitude of a Cone-Cylinder Body During
                  Autorotation Development in Vertical Descent

COMPARISON OF AUTOROTATION ATTITUDE

Body Physical & Aerodynamic Characteristics From Table I

θ_{ss} —DEG.

MAGNUS AUTOROTATION MOMENT (LARGE ROLL)

AUTOROTATION MOMENT FROM FLAPS ($p = -r_{ss}$ TAN θ)
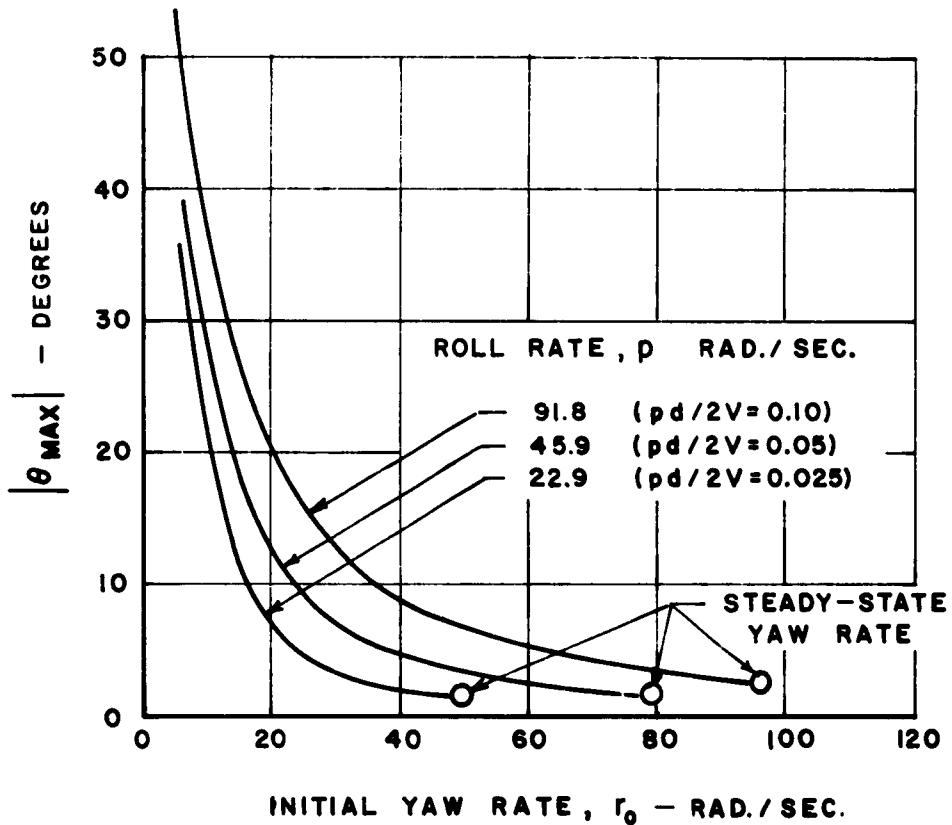
r_{ss} — RAD./ SEC.

ROLL RATE AND FLAP SPAN REQUIREMENTS

$p - \dfrac{RAD.}{SEC.}$

ROLL RATE REQUIREMENT FOR MAGNUS AUTOROTATION

c = 0.06 d

ℓ_F

r

d

FLAP SPAN REQUIREMENT

ℓ_F / d

ROLL RATE REQUIREMENT FOR BODY WITH FLAPS
$p = -r_{ss}$ TAN θ

r_{ss} — RAD. / SEC.
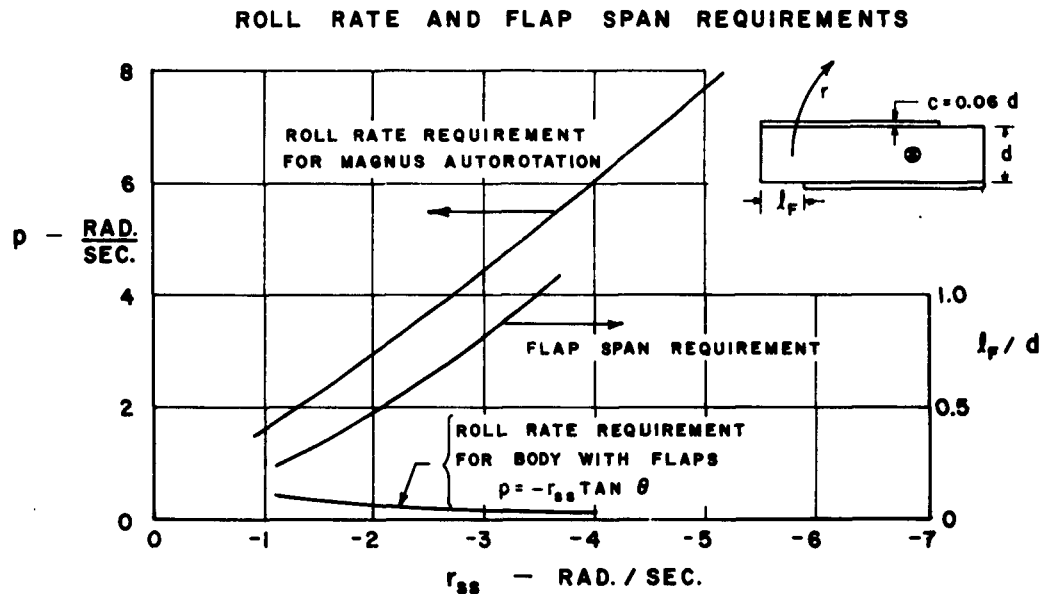
Figure 19.   Steady-State Autorotation Characteristics of a Large-Booster Configuration in Vertical Descent at Sea Level

MAGNUS AUTOROTATION
$C_{N_{p\pi/2}} = 13.15$ ($p = 2$ RAD./SEC.)
$C_{M_{z_0}} = 0$

—————— AUTOROTATION FROM FLAPS
$C_{N_{p\pi/2}} = 0$
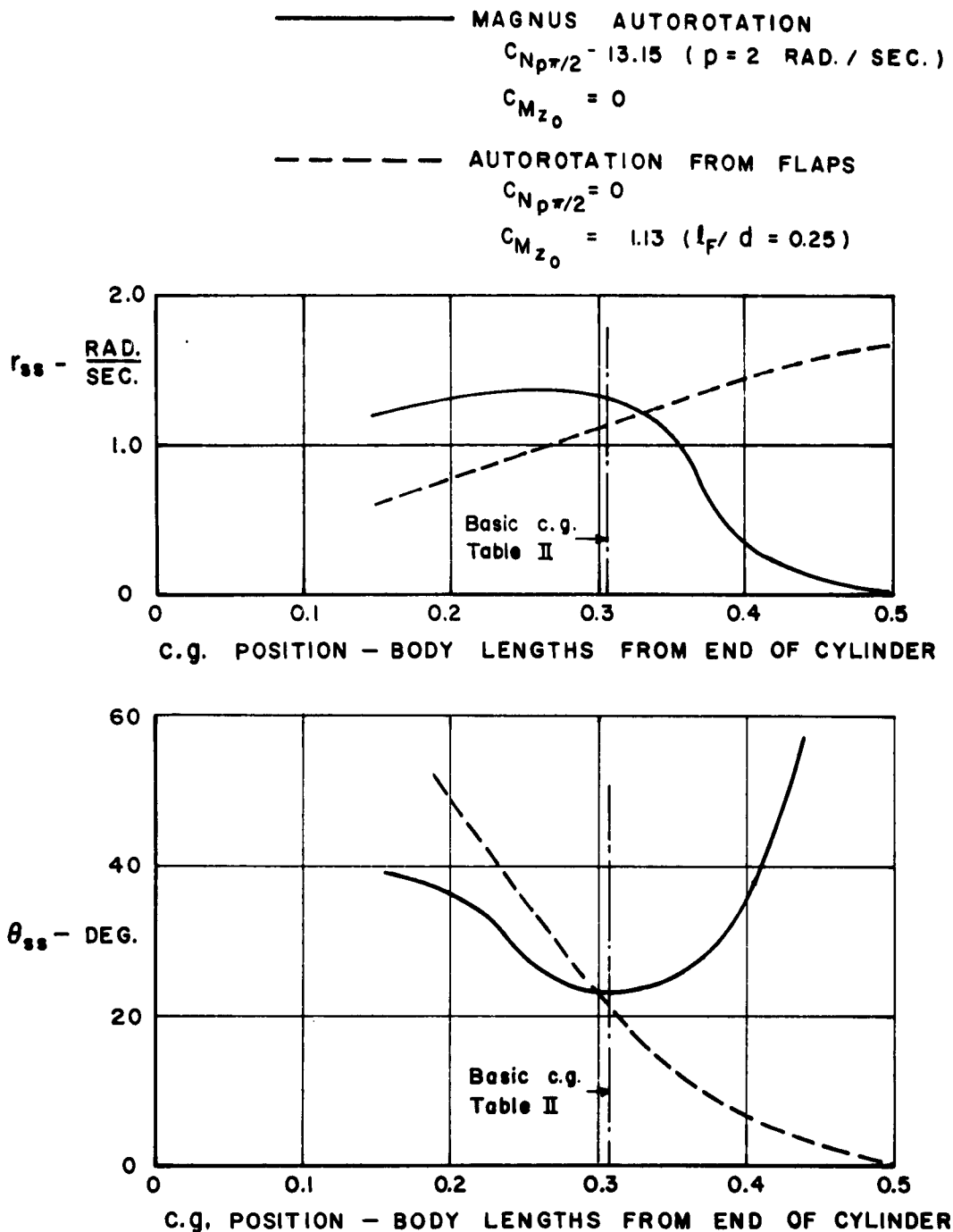$C_{M_{z_0}} = 1.13$ ($l_F/d = 0.25$)

Figure 20.   Effect of Center-of-Gravity Axial Location on the
Autorotation Characteristics of a Large-Booster
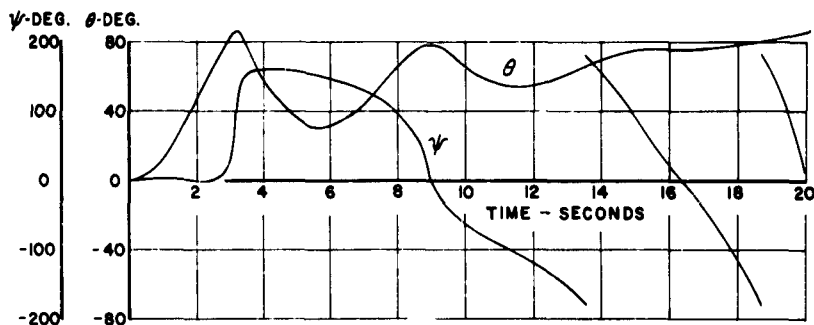Configuration in Vertical Descent at Sea Level

81

Figure 21.   Initial Low-Altitude Pitching and Yawing Motions for a
              Rolling Large-Booster Configuration. Time Histories
              of θ and ψ for $r_o = 0$, $\alpha_o = 90°$, and $pd/2V = 0.1$.

Figure 22.   Initial Low-Altitude Pitching and Yawing Motions for
              Rolling Large-Booster Configuration. Time Histories
              of θ and ψ for $r_o = 0$, $\alpha_o = 90°$, and $pd/2V = 0.2$.

Figure 23.   Initial Low-Altitude Pitching and Yawing Motions of a
              Rolling Large-Booster Configuration. Time Histories
              of θ and ψ for $r_o = 0$, $\alpha_o = 90°$, and $pd/2V = 0.3$.

82

Figure 24.   Initial Low-Altitude Pitching and Yawing Motions of a Large-Booster Configuration with Flaps.   Time Histories of θ and ψ for $r_o = 0$, $\alpha_o = 90°$, and $C_{M_{z_o}} = -3.02$.
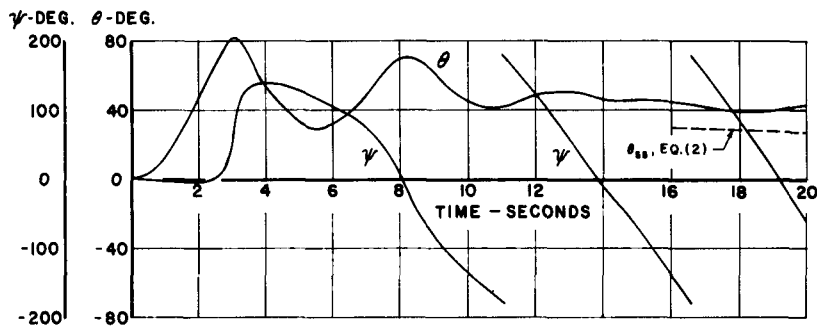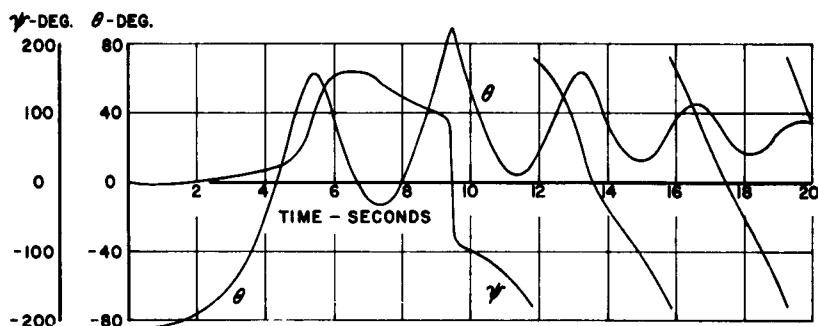

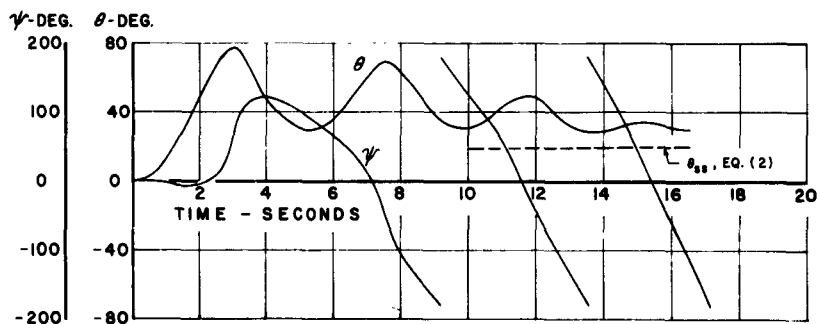Figure 25.   Initial Low-Altitude Pitching and Yawing Motions of a Rolling Large-Booster Configuration.   Time Histories of θ and ψ for $r_o = 0$, $\alpha_o = 5°$, and $pd/2V = 0.3$.

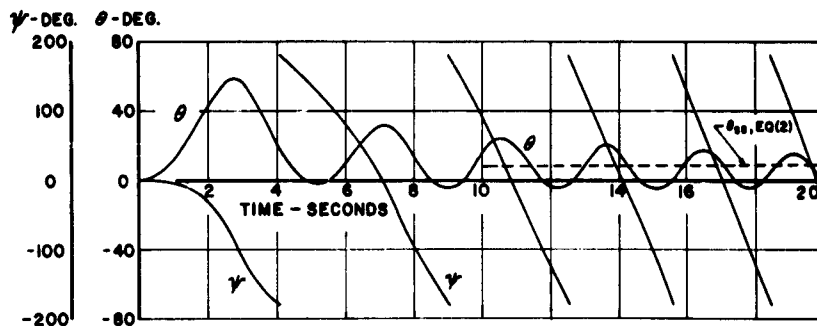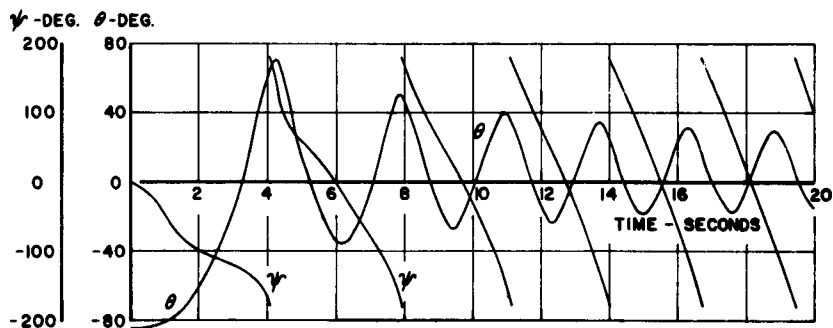Figure 26.   Initial Low-Altitude Pitching and Yawing Motion of a Large-Booster Configuration with Flaps.   Time Histories of θ and ψ for $r_o = 0$, $\alpha_o = 5°$, and $C_{M_{z_o}} = -3.02$
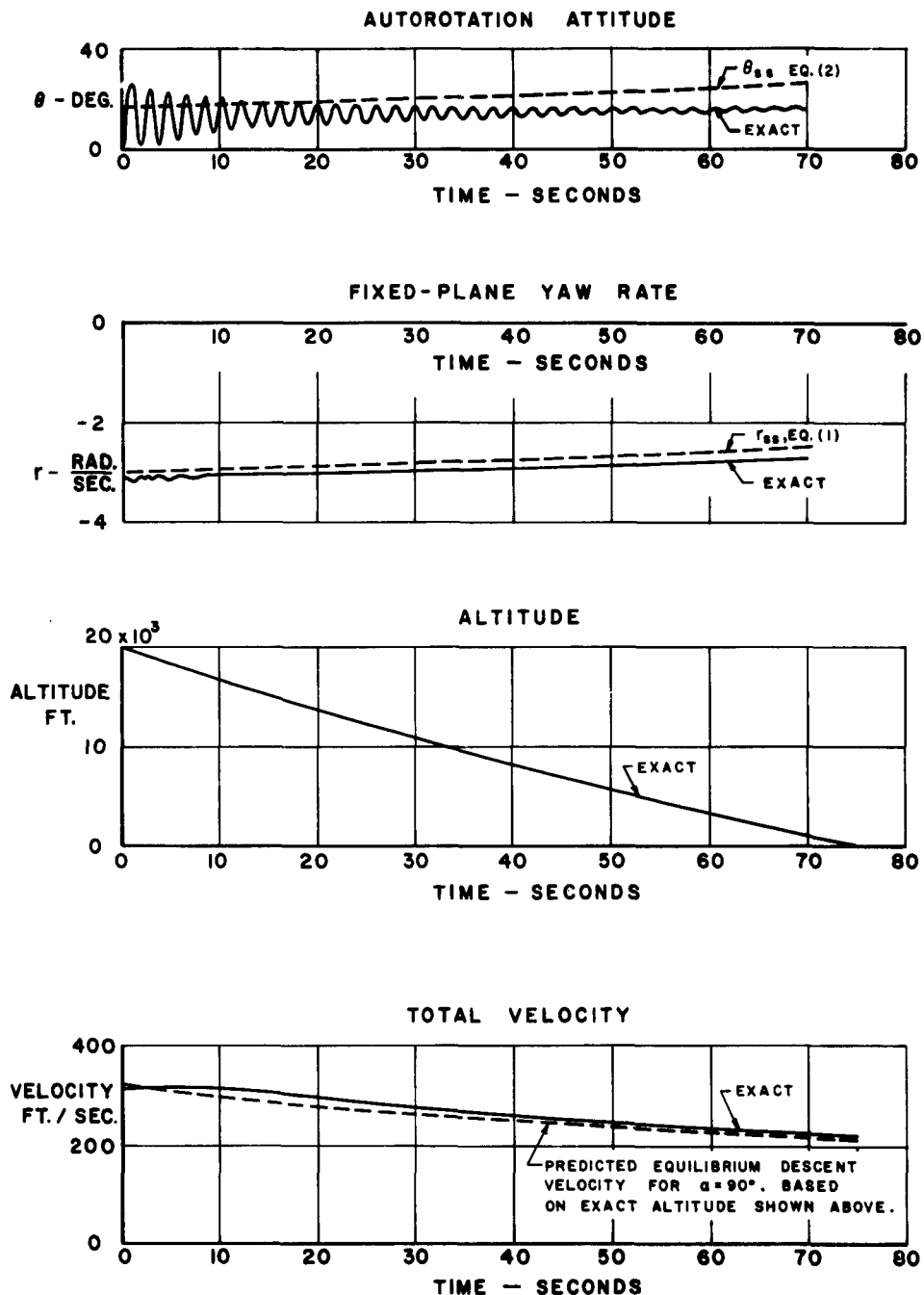
Figure 27.   Low-Altitude Autorotative Motion and Trajectory Data for a
Rolling Large-Booster Configuration in Vertical Descent with
a Large Initial Yaw Rate and a Roll Surface Speed Ratio of 0.3
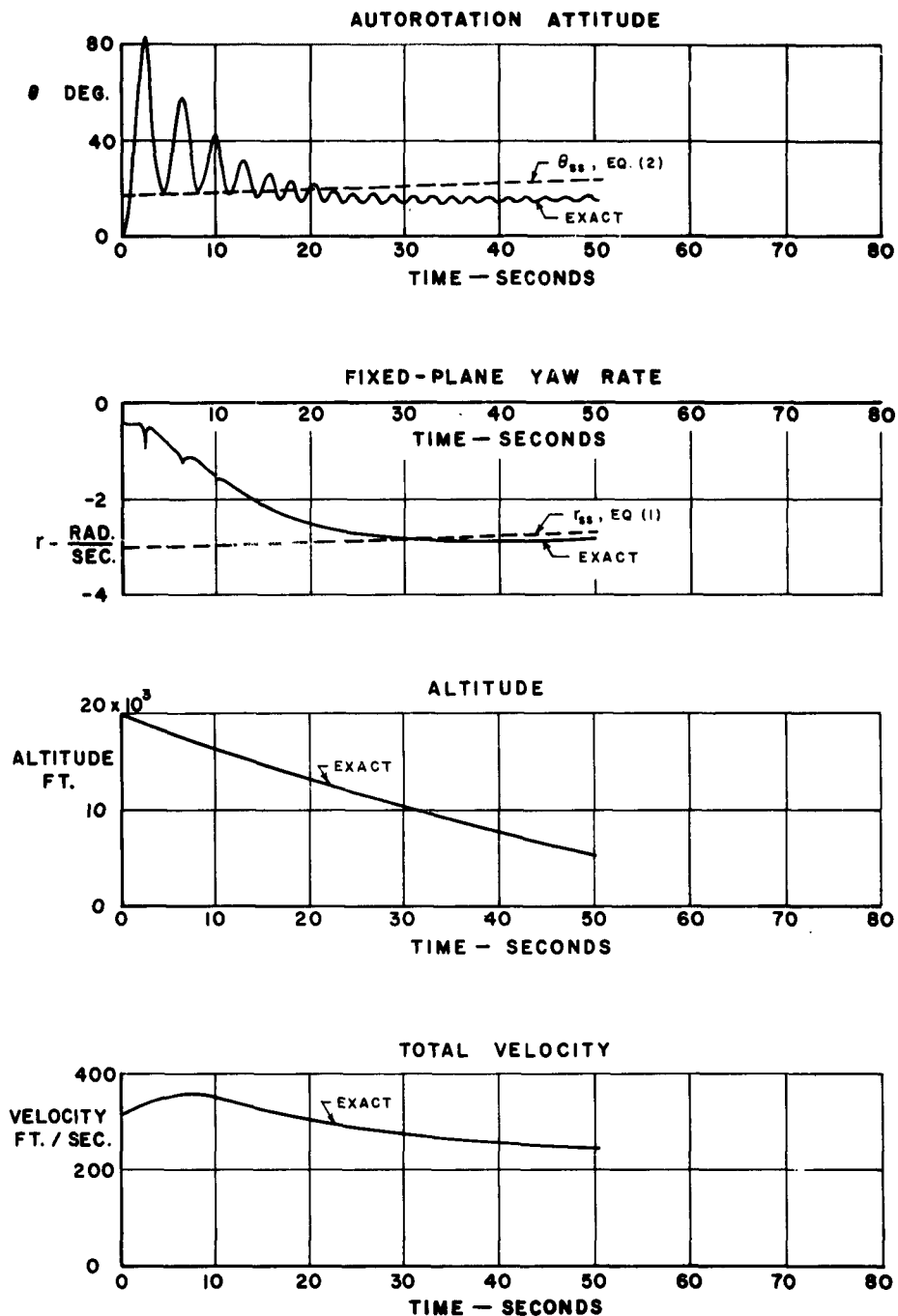
Figure 28. Low-Altitude Autorotative Motion and Trajectory Data for a Rolling Large-Booster Configuration in Vertical Descent with a Small Initial Yaw Rate and a Roll Surface Speed Ratio of 0. 3

85

VECTOR ANGLE OF ATTACK

NO AUTOROTATIVE MOMENT, $r_0 = 0$

α – RADIANS

$\left[\theta_{ss \, EQ.(4)} + \pi/2\right]$

EXACT : SIX-DEGREES-OF-FREEDOM EQUATIONS OF MOTION

TIME – SECONDS

FIXED-PLANE YAW RATE

r – RAD. / SEC.

r_{ss} , EQ. (3)

EXACT

TIME – SECONDS

TOTAL VELOCITY

VELOCITY – FT. / SEC.

EXACT : NO AUTOROTATIVE MOMENT, $r_0 = 0$

EXACT, AUTOROTATIVE DESCENT

TIME – SECONDS

ALTITUDE

ALTITUDE – 1000 FT.

EXACT, AUTOROTATIVE DESCENT

EXACT : NO AUTOROTATIVE MOMENT, $r_0 = 0$

TIME – SECONDS

Figure 29.   Re-Entry Motion and Trajectory Data for an Autorotating Large-Booster Configuration with Small Overturning Moment and an Autorotative Moment About the z Fixed-Plane Axis

86
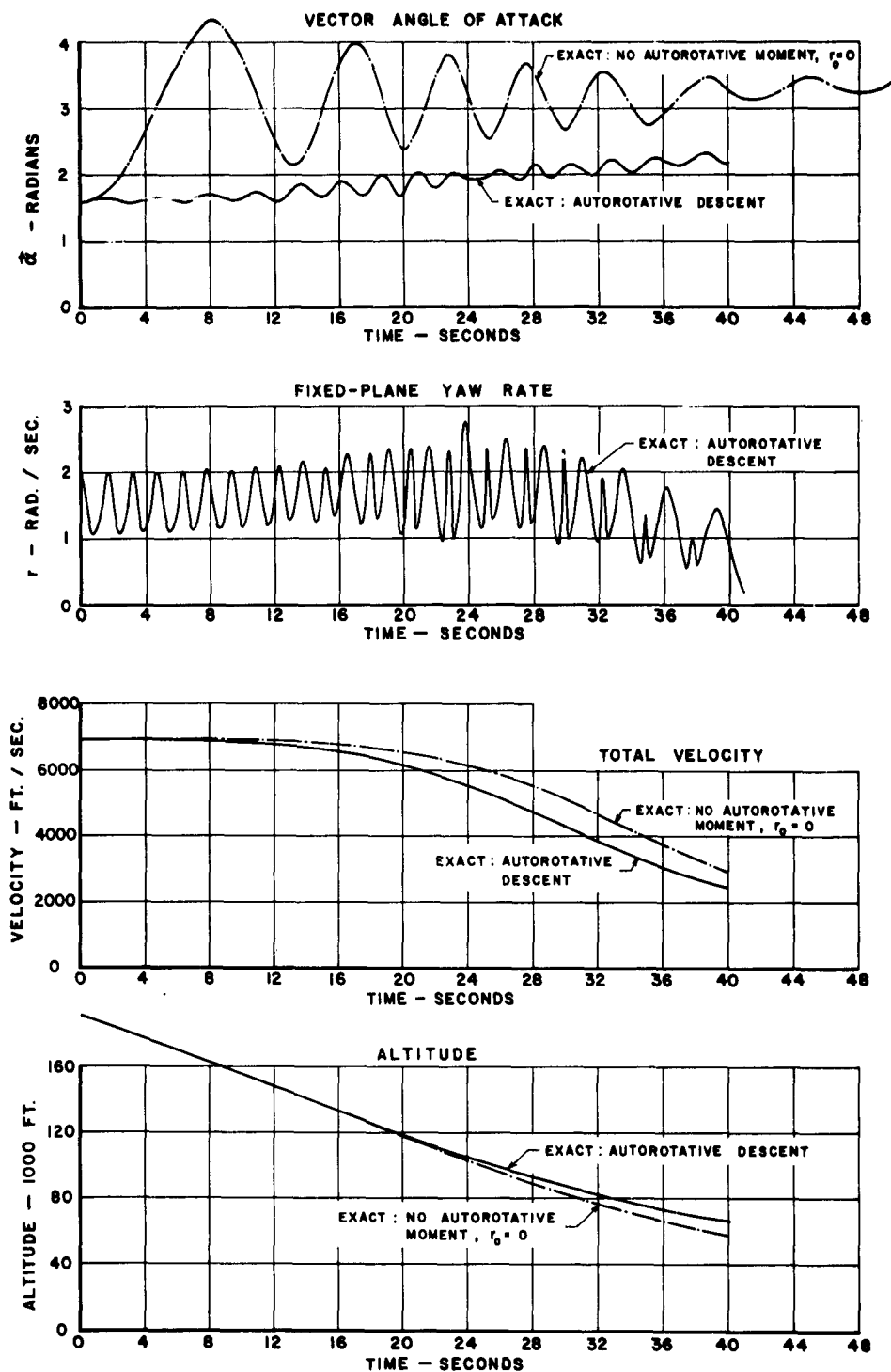
Figure 30.   Re-Entry Motion and Trajectory Data for an Autorotating
Large-Booster Configuration with Large Overturning Moment
and an Autorotative Moment About the z Fixed-Plane Axis
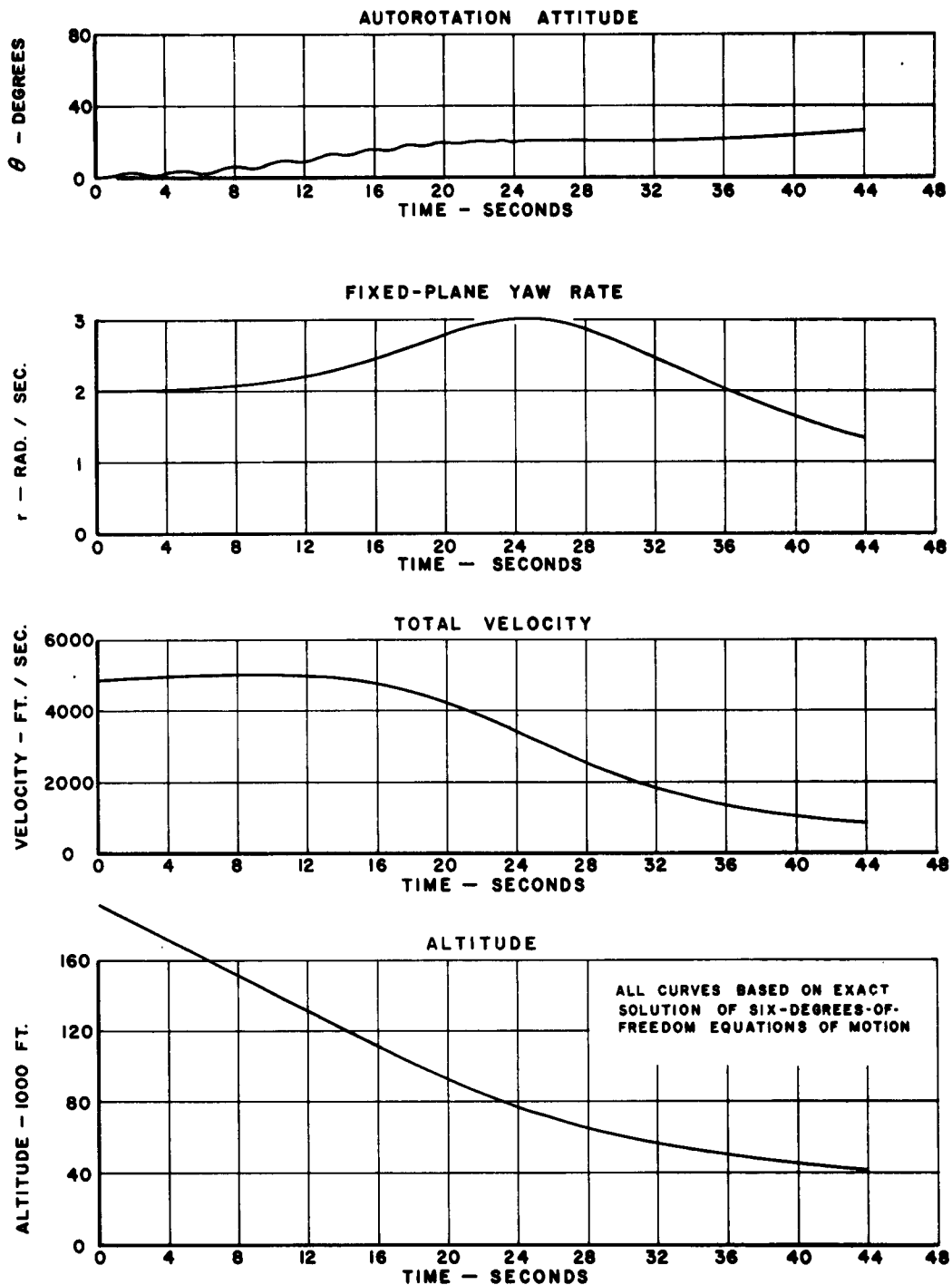
Figure 31.   Autorotative Motion During Vertical Re-Entry for a Large-
Booster Configuration with an Initial Yaw Spin Rate of
2 radians/second

88
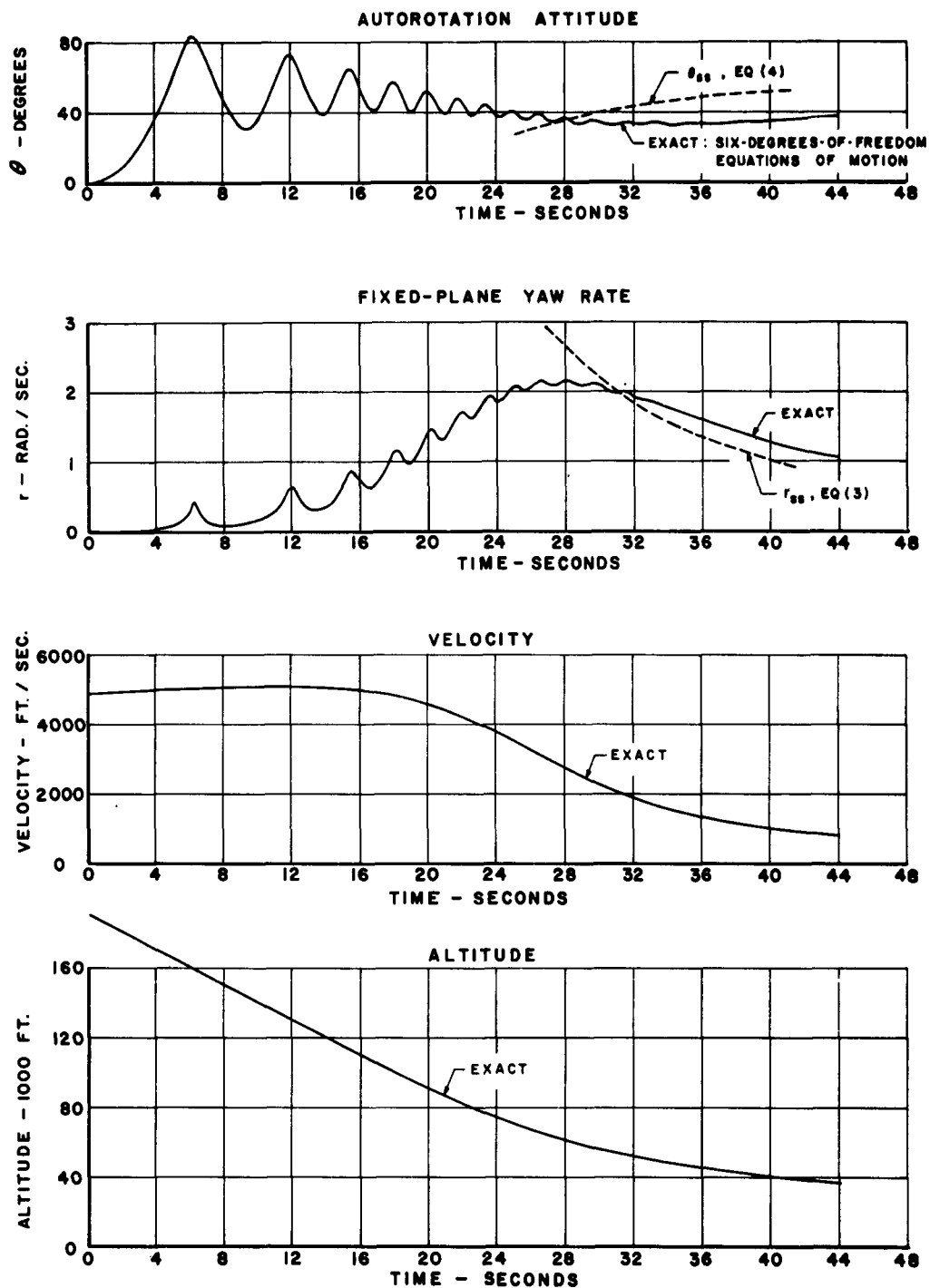
Figure 32.   Autorotative Motion During Vertical Re-Entry for a Large-Booster Configuration with Zero Initial Yaw Spin Rate

Figure 33. Effect of the Various Re-Entry Motions of a Large-
Booster Configuration on the Variation of Flight
Velocity with Altitude for a 30-Degree Re-Entry Angle

90

	INITIAL $\bar{a}$	TYPE OF RE-ENTRY MOTION	OVERTURNING MOMENT COEFFICIENT $C_{M_{\pi/2}}$	AUTOROTATIVE MOMENT COEFFICIENT $C_{M_{z_0}}$
– – – –	90°	AUTOROTATIVE	0.65	0.2
— — —	90°	AUTOROTATIVE	5.10	0.4
—·—·—	90°	TUMBLING	0.65	0
—··—··—	90°	TUMBLING	5.10	0
————	180°	STABLE AT α=180°	—	0
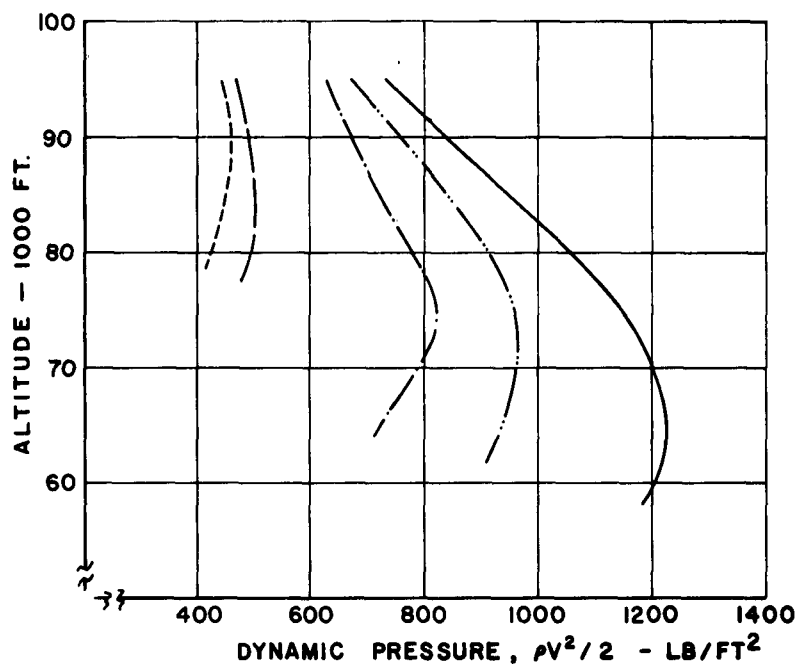
Figure 34.   Effect of Various Re-Entry Motions of a Large-Booster
Configuration on the Variation of Dynamic Pressure
with Altitude for a 30-Degree Re-Entry Angle

91

INITIAL $\overline{\alpha}$	TYPE OF RE-ENTRY MOTION	OVERTURNING MOMENT COEFFICIENT $c_{M_{\pi/2}}$	AUTOROTATIVE MOMENT COEFFICIENT $c_{M_{z_0}}$
90°	AUTOROTATIVE	5.1	0.4
180°	STABLE AT α=180°	—	0
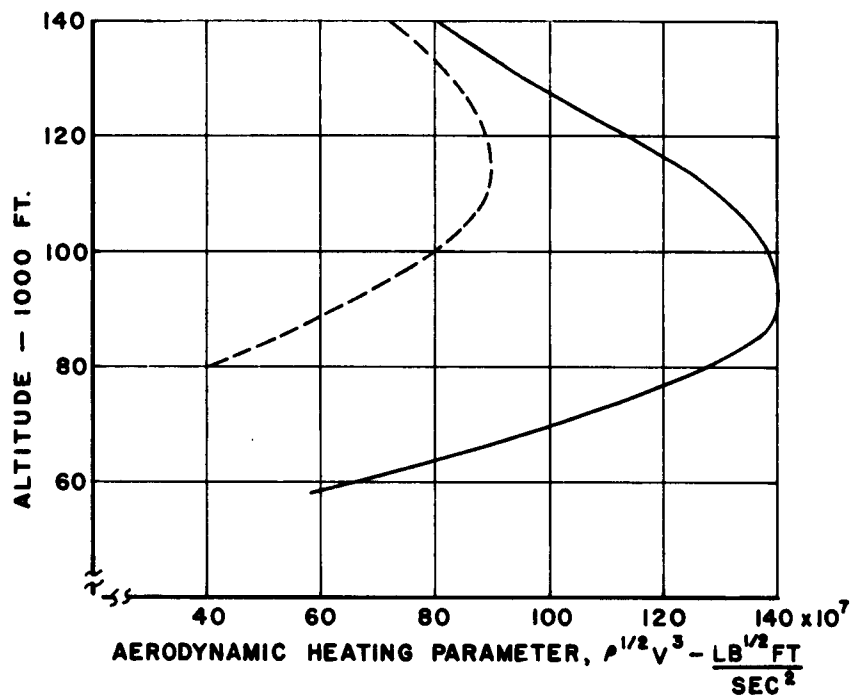
Figure 35.   Effect of Various Re-Entry Motions on the Body Stagnation Heating Rate Parameter $\rho^{1/2} V^3$
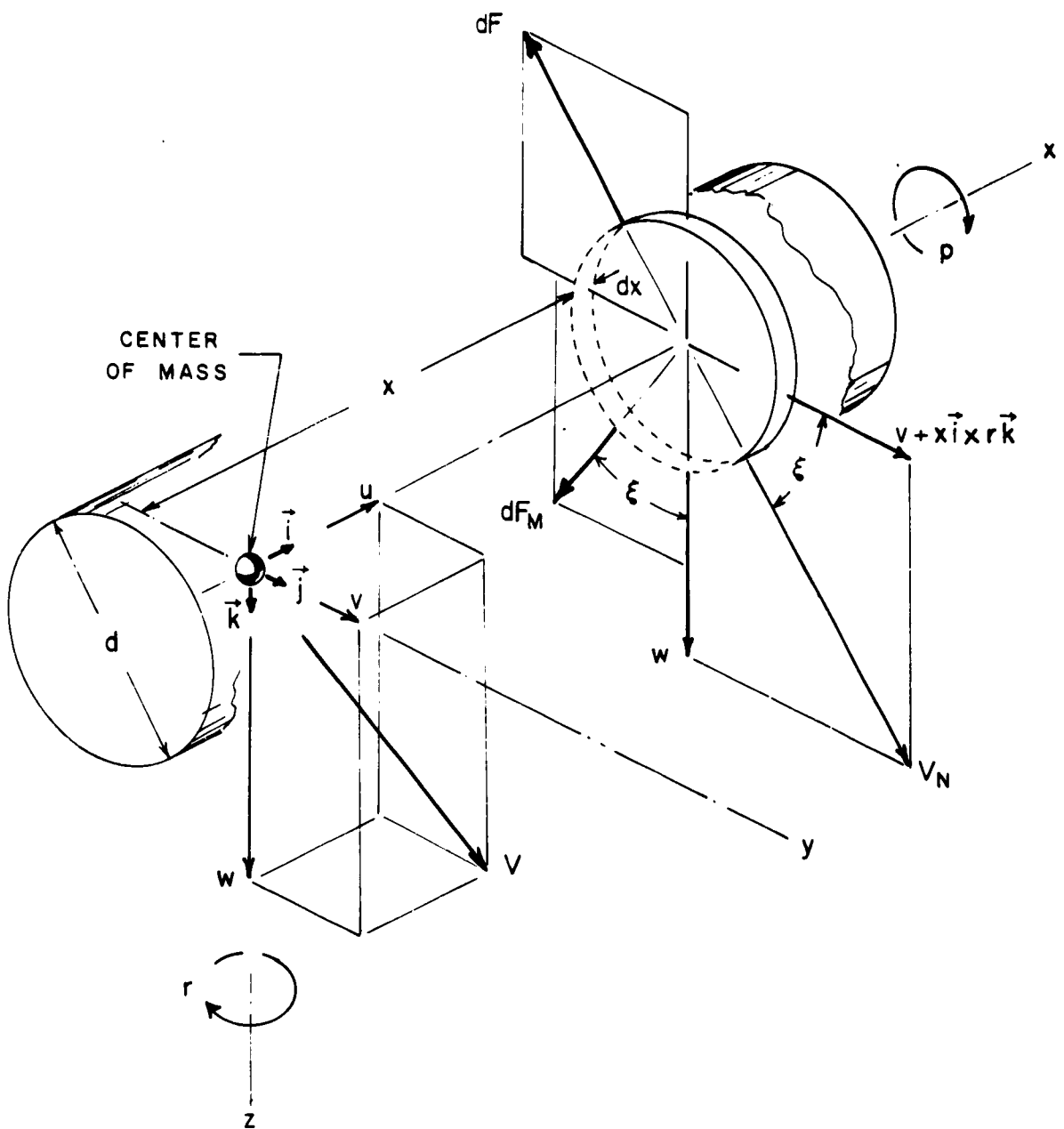
Figure 36.   Diagram for Determining Aerodynamic Moments
on a Circular Cylinder with Yawing and Rolling
Angular Velocity at Large Angle of Attack

93
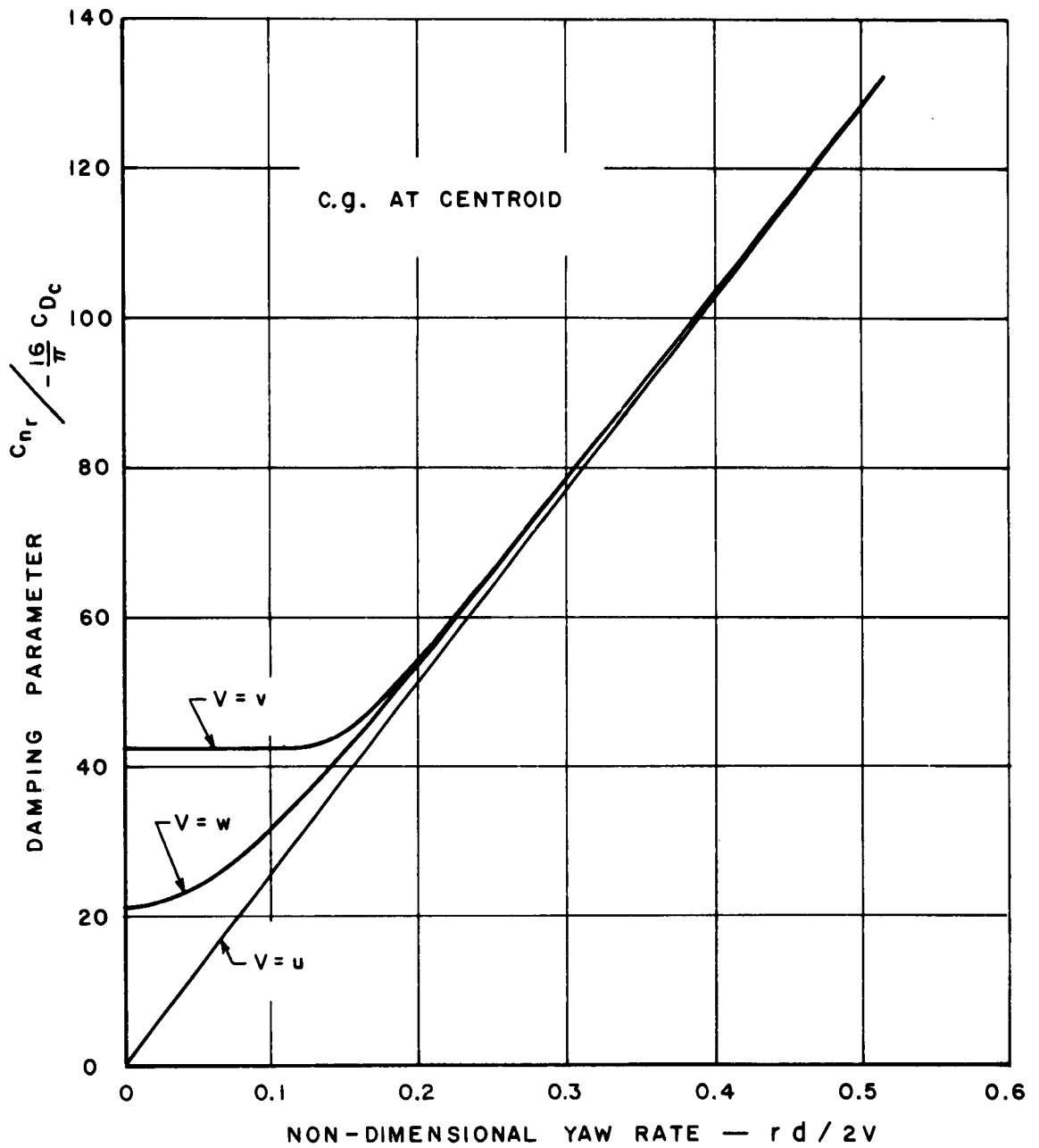
Figure 37.   Theoretical Yaw Damping for a Fineness-Ratio-
Eight Circular Cylinder

AERODYNAMIC MOMENTS DUE TO TRANSVERSE ANGULAR VELOCITY
AND ROLL SPIN AT LARGE ANGLE OF ATTACK

The aerodynamic moment derivatives due to rotation, r, about the
fixed-plane or body-fixed z axes at large angle of attack are herein derived
for a smooth cylindrical body. The flow is assumed to be separated along
the entire leeward side of the body such that the forces on a local section of
the body are due entirely to the cross flow, and thus are independent of the
axial flow. Both the local drag and Magnus forces are considered. The
moments about the y and z axes will be determined, where these axes
may be either fixed-plane or body-fixed.

The analysis is based on the assumptions normally used in strip
theory. The force model is depicted in Figure 36. The moments due to
the elemental forces dF and dF_M will be derived independently.

The scalar force dF is defined as

$$dF = \frac{1}{2} \rho\, V_N^2\, C_{D_C}\, d\, dx \qquad (1)$$

and the scalar force dF_M as

$$dF_M = \frac{1}{2} \rho\, V_N^2 \cdot C_{F_p \pi /2} \left(\frac{pd}{2 V_N} \right) d\, dx \qquad (2)$$

The incremental scalar moment dM_z due to the force vector $\vec{dF}$ can be expressed as follows:

$$dM_z = \left[x\,\vec{i} \times \vec{dF} \right] \cdot \vec{k}$$

$$= \left(x\,\vec{i} \times \left[-dF_y\,\vec{j} - dF_z\,\vec{k} \right] \right) \cdot \vec{k} \tag{3}$$

$$= -x\,dF_y$$

By letting $dF_y = dF \cos \xi = dF \left[\dfrac{v + xr}{V_N} \right]$

and $dC_{M_z} = \dfrac{dM_z}{\frac{1}{2}\,\rho\,V^2\,S\,d}$

we obtain from (2) and (3), in coefficient form

$$dC_{M_z} = \frac{-C_{D_C} \left[v + rx \right] \sqrt{w^2 + (v + rx)^2}\; x\; dx}{S\,V^2} \tag{4}$$

In a similar manner we obtain the incremental scalar moment dM_y due to the force vector $\vec{dF}$ as

$$dM_y = \left[x\,\vec{i} \times \vec{dF} \right] \cdot -\vec{j}$$

$$= x\,dF_y \tag{5}$$

and in coefficient form

$$dC_{M_y} = \frac{C_{D_C} \, w \, \sqrt{w^2 + (v + rx)^2} \quad x \, dx}{S \, v^2} \tag{6}$$

The incremental scalar moment dM_{z_M} due to the Magnus force vector $\vec{dF}_M$ can be expressed as follows:

$$\begin{aligned} dM_{z_M} &= \left[x \, \vec{i} \times \vec{dF}_M \right] \cdot \vec{k} \\ &= -x \, dF_{M_y} \end{aligned} \tag{7}$$

Letting $dF_{M_y} = dF_M \sin \xi = dF_M \dfrac{w}{V_N}$

and $dC_{M_{z_M}} = \dfrac{dM_{z_M}}{\frac{1}{2} \rho \, V^2 \, S \, d}$

we obtain from (2) and (7) in coefficient form

$$dC_{M_{z_M}} = -\frac{w}{VS} \, C_{F_p} \, \pi/2 \, \frac{pd}{2V} \, x \, dx \tag{8}$$

Proceeding as above, we find the scalar moment dM_{y_M} due to the Magnus force vector $\vec{dF}_M$ as

$$\begin{aligned} dM_{y_M} &= \left[x \, \vec{i} \times \vec{dF}_M \right] \cdot \vec{-j} \\ &= -x \, dF_{M_z} \end{aligned} \tag{9}$$

3

and in coefficient form

$$dC_{M_{y_M}} = \frac{-(v + rx)\sqrt{w^2 + (v + rx)^2}\ C_{F_p}\ \pi/2\ \frac{pd}{2V}\ x\ dx}{v^2 S} \qquad (10)$$

In the equations of motion, the aerodynamic moments are entered as partial derivatives. It is necessary, therefore, to express (4), (6), (8), and (10) in derivative form. It is also necessary to make the aerodynamic reference area and length, and the roll and yaw rate parameters consistent with the aerodynamic force system adopted in the equations of motion. Thus we now use, consistently

$$\text{reference area, S} \quad = \cdot \pi d^2/4$$
$$\text{reference length} \quad = d$$
$$\text{roll rate parameter} \quad = pd/2V$$
$$\text{yaw rate parameter} \quad = rd/2V$$

and define the derivatives C_{n_r} and $C_{M_{pr}}$ as

$$C_{n_r} = \frac{\partial\ C_{M_z}}{\partial\ \frac{rd}{2V}}$$

$$C_{M_{pr}} = \frac{\partial\ C_{M_{y_M}}}{\partial\ \frac{pd}{2V}\ \frac{rd}{2V}}$$

4

Since (8) is independent of r, we evaluate the incremental value of C_{n_r} from (4). Making the previously described substitutions, we obtain

$$\frac{\partial \, dC_{M_z}}{\partial \, \frac{rd}{2V}} = \frac{-16 \, C_{D_C}}{\pi} \, \frac{rd}{2V} \left\{ \frac{2\left(\frac{v}{rd} + \frac{x}{d}\right)^2 + \left(\frac{w}{rd}\right)^2}{\left[\left(\frac{v}{rd} + \frac{x}{d}\right)^2 + \left(\frac{w}{rd}\right)^2\right]^{1/2}} \right\} \frac{x^2}{d^2} \, d\left(\frac{x}{d}\right)$$

or in integral form

$$C_{n_r} = -\frac{16}{\pi} \, \frac{rd}{2V} \int_{\left(\frac{x}{d}\right)_1}^{\left(\frac{x}{d}\right)_2} C_{D_C} \left\{ \frac{2\left(\frac{v}{rd} + \frac{x}{d}\right)^2 + \left(\frac{w}{rd}\right)^2}{\left[\left(\frac{v}{rd} + \frac{x}{d}\right)^2 + \left(\frac{w}{rd}\right)^2\right]^{1/2}} \right\} \left(\frac{x}{d}\right)^2 \, d\left(\frac{x}{d}\right) \tag{11}$$

We leave C_{D_C} under the integral sign because it may be desired to introduce C_{D_C} as some function of (x/d) to account for three-dimensional flow effects.

A closed form solution to (11) is not possible, except for special cases. However, solutions have been obtained for the special cases $V = w$, $V = u$, and $V = v$, and these permit a great deal of insight into the equation. The case $V = w$ is particularly significant, since it represents the yaw damping in a flat spin.

5

The solution for $V = w$ was obtained by using the integration by parts formulae. The resulting solution with the integration limits substituted is

$$C_{n_r} = -\frac{16}{\pi} C_{D_C} \frac{rd}{2V} \left\{ \sqrt{\left|\frac{x}{d}\right|_2^2 + \left(\frac{V}{rd}\right)^2} \left[\frac{1}{2} \left|\frac{x}{d}\right|_2^3 - \frac{1}{4} \left(\frac{V}{rd}\right)^2 \left|\frac{x}{d}\right|_2 \right] - \right.$$

$$\sqrt{\left|\frac{x}{d}\right|_1^2 + \left(\frac{V}{rd}\right)^2} \left[\frac{1}{2} \left|\frac{x}{d}\right|_1^3 - \frac{1}{4} \left(\frac{V}{rd}\right)^2 \left|\frac{x}{d}\right|_1 \right] +$$

$$\left. \frac{1}{4} \left(\frac{V}{rd}\right)^4 \ln \frac{\left|\frac{x}{d}\right|_2 + \sqrt{\left|\frac{x}{d}\right|_2^2 + \left(\frac{V}{rd}\right)^2}}{\left|\frac{x}{d}\right|_1 + \sqrt{\left|\frac{x}{d}\right|_1^2 + \left(\frac{V}{rd}\right)^2}} \right\}$$

(12)

$$(V = w, \quad r \ne 0)$$

The solutions for $V = u$ and $V = v$ are

$$C_{n_r} = -\frac{8}{\pi} C_{D_C} \frac{rd}{2V} \left[\left|\frac{x}{d}\right|_2^4 - \left|\frac{x}{d}\right|_1^4 \right]$$

(13)

$$(V = u, \quad r \ne 0)$$

6

and

$$C_{n_r} = -\frac{16}{\pi} \, C_{D_C} \left\{ \frac{1}{3} \left[\left(\frac{x}{d}\right)_2^3 - \left(\frac{x}{d}\right)_1^3 \right] + \frac{1}{4} \left(\frac{rd}{V}\right) \left[\left(\frac{x}{d}\right)_2^4 - \left(\frac{x}{d}\right)_1^4 \right] \right\} \tag{14}$$

$$(V = v, \quad r \neq 0)$$

Care must be exercised in evaluating (14), because if x/d is large, the integral changes sign as a result of the local cross force due to rotation, r, not being in the same direction as the local cross velocity, V_N. It is easily recognized that equation (14) could be used for C_{M_q} at $\alpha = \pi/2$, if we let $r = q$ and $v = w$.

Another special case is the limiting condition $r = 0$ for $V = w$. This leads to

$$C_{n_r} = -\frac{8}{3\pi} \, C_{D_C} \left[\left(\frac{x}{d}\right)_2^3 - \left(\frac{x}{d}\right)_1^3 \right] \tag{15}$$

$$(V = w, \quad r = 0)$$

To illustrate the non-linear nature of the yaw damping derivative, C_{n_r}, as a function of $rd/2V$, calculations have been made for a fineness-ratio-eight cylinder with the center of rotation at the midpoint. The drag coefficient C_{D_C} is assumed independent of x/d such that the resulting damping can be presented as the parameter

$$C_{n_r} \,/\, -\frac{16}{\pi} \, C_{D_C}$$

7

The resulting variations of $\dfrac{C_{n_r}}{-\dfrac{16\,C_{D_C}}{\pi}}$ with $rd/2V$ for $V = w$, $V = u$, and

$V = v$ are presented in Figure 37.

At subsonic velocity, bodies of moderate fineness ratio have an average cross drag coefficient which is considerably less than the two-dimensional value. Although exact force distribution data are not available, it is reasonable to assume that the distribution of C_{D_C} along the body will be nearly elliptical. For such a distribution of C_{D_C}, it is extremely useful to have an approximate correction factor for equation (15) such that laborious numerical integrations of equation (11) can be avoided.

The simplest form of correction is an adjustment in the value of C_{D_C}. This effective value of C_{D_C}, when used in equation (15), will then account for the effect of the elliptical force distribution on the damping derivative. Such a factor has been evaluated and is found to be exactly 3/4 of the average cylinder cross drag coefficient when the transverse axis of rotation passes through the midpoint of the cylinder. Of this factor, $3\,\pi/16$ is the ratio of the damping derivative with elliptical cross force distribution to the damping derivative with constant cross force, and $4/\pi$ is the ratio of the equivalent C_{D_C} for the elliptical force distribution to the average cylinder cross drag coefficient for the constant cross force condition.

The contribution of the Magnus force to the moment about the z axis, equation (8), is seen to be independent of the yaw rate. In fact, the moment coefficient $C_{M_{zM}}$ is the basic Magnus moment coefficient which is included in the linear equations of motion in derivative form as

$$C_{M_{z_{magnus}}} = C_{M_p}\ \pi/2\ \frac{pd}{2V}\ \frac{w}{V}$$

8

The pitching moment coefficients, C_{M_y}, and $C_{M_{y_M}}$, as given by equations (6) and (10), respectively, are both a function of the yaw rate, r; and (10) is also a function of the roll rate, p.

From (6) we can evaluate C_{M_r} in the same manner as we previously evaluated C_{n_r}. The general form cannot be integrated in closed form, so only the case of V = w will be presented. The result is

$$
C_{M_r} = \frac{8}{\pi} \left|\frac{rd}{2V}\right|^2 \left\{ \left\{ \frac{1}{5} \left|\frac{x}{d}\right|^2 - \frac{2}{15\left|\frac{rd}{2V}\right|^2} \right\} \left\{ \frac{1}{\left|\frac{rd}{2V}\right|^2} + \left|\frac{x}{d}\right|^2 \right\}^{\frac{3}{2}} \right\}_{\left|\frac{x}{d}\right|_1}^{\left|\frac{x}{d}\right|_2}
\tag{16}
$$

The derivative C_{M_r} will be zero for rd/2V equal to zero, and also for $(x/d)_2 = (x/d)_1$. For most configurations, this derivative will be very small, and hence can be neglected.

From (10) we can evaluate the derivative $C_{M_{pr}}$, which will be the pitching moment resulting from the distortion of the Magnus force at the ends of the body. The distortion, of course, is proportional to the local velocity at the ends of the body. It will be noted that the form of equation (10) after differentiation by (pd/2V), is identical to (4) if we replace C_{D_C} by $C_{F_{p\pi/2}}$. Therefore, we can express $C_{M_{pr}}$ as

$$
C_{M_{pr}} = \frac{C_{F_{p\pi/2}}}{C_{D_C}} C_{n_r}
\tag{17}
$$

9

Thus, equations (12) and (15) can also be used for evaluation of $C_{M_{pr}}$ for the special case of $V = w$. This derivative will have a finite value at $r = 0$, and will be of a significant magnitude whenever the Magnus force is present.

APPENDIX II

COMPLETE SIX-DEGREES-OF-FREEDOM

EQUATIONS OF MOTION

The complete six-degrees-of-freedom equations of motion are derived in Reference 1, and are presented here for reference only.

Body-Fixed Axes

$$\dot{u} = \tilde{r}\,\tilde{v} - \tilde{q}\,\tilde{w} + 2(\lambda_1\lambda_3 - \lambda_0\lambda_2)\,g + F_x/m$$

$$\dot{\tilde{v}} = p\,\tilde{w} - \tilde{r}\,u + 2(\lambda_2\lambda_3 \; \lambda_0\lambda_1)\,g + F_y/m$$

$$\dot{\tilde{w}} = \tilde{q}\,u - p\,\tilde{v} + (\lambda_0^2 - \lambda_1^2 - \lambda_2^2 + \lambda_3^2)\,g + F_z/m$$

$$\frac{I_x}{I}\,\dot{p} = \frac{M_x}{I}$$

$$\dot{\tilde{q}} = \tilde{r}\,p\left(1 - \frac{I_x}{I}\right) + \frac{M_y}{I}$$

$$\dot{\tilde{r}} = -\tilde{q}\,p\left(1 - \frac{I_x}{I}\right) + \frac{M_z}{I}$$

$$\dot{X} = (\lambda_0^2 + \lambda_1^2 - \lambda_2^2 - \lambda_3^2)\,u + 2(\lambda_1\lambda_2 - \lambda_0\lambda_3)\,\tilde{v} + 2(\lambda_1\lambda_3 + \lambda_0\lambda_2)\,\tilde{w}$$

$$\dot{Y} = 2(\lambda_1\lambda_2 + \lambda_0\lambda_3)\,u + (\lambda_0^2 - \lambda_1^2 + \lambda_2^2 - \lambda_3^2)\,\tilde{v} + 2(\lambda_2\lambda_3 - \lambda_0\lambda_1)\,\tilde{w}$$

$$\dot{Z} = 2(\lambda_1\lambda_3 - \lambda_0\lambda_2)\,u + 2(\lambda_2\lambda_3 + \lambda_0\lambda_1)\,\tilde{v} + (\lambda_0^2 - \lambda_1^2 - \lambda_2^2 + \lambda_3^2)\,\tilde{w}$$

$$\dot{\lambda}_0 = 1/2\,(-\lambda_1 p - \lambda_2\tilde{q} - \lambda_3\tilde{r})$$

$$\dot{\lambda}_1 = 1/2\,(\lambda_0 p - \lambda_3\tilde{q} + \lambda_2\tilde{r})$$

$$\dot{\lambda}_2 = 1/2\,(\lambda_3 p + \lambda_0\tilde{q} - \lambda_1\tilde{r})$$

$$\dot{\lambda}_3 = 1/2\,(-\lambda_2 p + \lambda_1\tilde{q} + \lambda_0\tilde{r})$$

12

Fixed-Plane Axes

$$\dot{u} = rv - qw + 2(\lambda_1\lambda_3 - \lambda_0\lambda_2)g + F_x/m$$

$$\dot{v} = 2wr\frac{\lambda_1\lambda_3 - \lambda_0\lambda_2}{\lambda_0^2 - \lambda_1^2 - \lambda_2^2 + \lambda_3^2} - ru + F_y/m$$

$$\dot{w} = qu - 2vr\frac{\lambda_1\lambda_3 - \lambda_0\lambda_2}{\lambda_0^2 - \lambda_1^2 - \lambda_2^2 + \lambda_3^2} + (\lambda_0^2 - \lambda_1^2 - \lambda_2^2 + \lambda_3^2)g + F_z/m$$

$$\frac{I_x}{I}\dot{p} = \frac{M_x}{I}$$

$$\dot{q} = r\left(2r\frac{\lambda_1\lambda_3 - \lambda_0\lambda_2}{\lambda_0^2 - \lambda_1^2 - \lambda_2^2 + \lambda_3^2} - \frac{I_x}{I}p\right) + \frac{M_y}{I}$$

$$\dot{r} = -q\left(2r\frac{\lambda_1\lambda_3 - \lambda_0\lambda_2}{\lambda_0^2 - \lambda_1^2 - \lambda_2^2 + \lambda_3^2} - \frac{I_x}{I}p\right) + \frac{M_z}{I}$$

$$\dot{X} = (\lambda_0^2 + \lambda_1^2 - \lambda_2^2 - \lambda_3^2)u + 2(\lambda_1\lambda_2 - \lambda_0\lambda_3)v + 2(\lambda_1\lambda_3 + \lambda_0\lambda_2)w$$

$$\dot{Y} = 2(\lambda_1\lambda_2 + \lambda_0\lambda_3)u + (\lambda_0^2 - \lambda_1^2 + \lambda_2^2 - \lambda_3^2)v + 2(\lambda_2\lambda_3 - \lambda_0\lambda_1)w$$

$$\dot{Z} = 2(\lambda_1\lambda_3 - \lambda_0\lambda_2)u + (0)v + (\lambda_0^2 - \lambda_1^2 - \lambda_2^2 + \lambda_3^2)w$$

$$\dot{\lambda}_0 = -\frac{1}{2}\left(\lambda_2 q + \frac{\lambda_3 r}{\lambda_0^2 - \lambda_1^2 - \lambda_2^2 + \lambda_3^2}\right)$$

$$\dot{\lambda}_1 = -\frac{1}{2}\left(\lambda_3 q + \frac{\lambda_2 r}{\lambda_0^2 - \lambda_1^2 - \lambda_2^2 + \lambda_3^2}\right)$$

$$\dot{\lambda}_2 = \frac{1}{2}\left(\lambda_0 q + \frac{\lambda_1 r}{\lambda_0^2 - \lambda_1^2 - \lambda_2^2 + \lambda_3^2}\right)$$

$$\dot{\lambda}_3 = \frac{1}{2}\left(\lambda_1 q + \frac{\lambda_0 r}{\lambda_0^2 - \lambda_1^2 - \lambda_2^2 + \lambda_3^2}\right)$$

Aerodynamic Forces and Moments

$$\frac{F_X}{qS} = C_{X_0} + C_{X_2}(\alpha^2 + \beta^2) + \mu_X \Delta M$$

$$\frac{F_Y}{qS} = C_{Y_0} - \beta \left[C_{N\vec{\alpha}_0} + C_{N\vec{\alpha}_2}(\alpha^2 + \beta^2) + C_{N\vec{\alpha}_4}(\alpha^2 + \beta^2)^2 + \mu_{N_\alpha} \Delta M \right]$$

$$- \frac{pd}{2V} \, \alpha \left[C_{N_p\vec{\alpha}_0} + C_{N_p\vec{\alpha}_2}(\alpha^2 + \beta^2) + C_{N_p\vec{\alpha}_4}(\alpha^2 + \beta^2)^2 \right]$$

$$\frac{F_Z}{qS} = C_Z - \alpha \left[C_{N\vec{\alpha}_0} + C_{N\vec{\alpha}_2}(\alpha^2 + \beta^2) + C_{N\vec{\alpha}_4}(\alpha^2 + \beta^2)^2 + \mu_{N_\alpha} \Delta M \right]$$

$$+ \frac{pd}{2V} \, \beta \left[C_{N_p\vec{\alpha}_0} + C_{N_p\vec{\alpha}_2}(\alpha^2 + \beta^2) + C_{N_p\vec{\alpha}_4}(\alpha^2 + \beta^2)^2 \right]$$

$$\frac{M_X}{qSd} = \frac{pd}{2V} \left[C_{l_p} + \mu_{l_p} \Delta M \right]$$

$$\frac{M_Y}{qSd} = C_{M_{y_0}} + \alpha \left[C_{M\vec{\alpha}_0} + C_{M\vec{\alpha}_2}(\alpha^2 + \beta^2) + C_{M\vec{\alpha}_4}(\alpha^2 + \beta^2)^2 + \mu_{M_\alpha} \Delta M \right]$$

$$- \frac{pd}{2V} \, \beta \left[C_{M_p\vec{\alpha}_0} + C_{M_p\vec{\alpha}_2}(\alpha^2 + \beta^2) \quad C_{M_p\vec{\alpha}_4}(\alpha^2 + \beta^2)^2 \right]$$

$$+ \left(\frac{qd}{2V}\right) C_{M_{q_0}} + \left(\frac{qd}{2V}\right)^3 C_{M_{q_2}} + \left(\frac{pd}{2V}\right)\left(\frac{rd}{2V}\right) C_{M_{pr}}$$

$$\frac{M_Z}{qSd} = C_{M_{z_0}} - \beta \left[C_{M\vec{\alpha}_0} + C_{M\vec{\alpha}_2}(\alpha^2 + \beta^2) + C_{M\vec{\alpha}_4}(\alpha^2 + \beta^2)^2 + \mu_{M_\alpha} \Delta M \right]$$

$$- \frac{pd}{2V} \, \alpha \left[C_{M_p\vec{\alpha}_0} + C_{M_p\vec{\alpha}_2}(\alpha^2 + \beta^2) + C_{M_p\vec{\alpha}_4}(\alpha^2 + \beta^2)^2 \right]$$

$$+ \left(\frac{rd}{2V}\right) C_{n_{r_0}} + \left(\frac{rd}{2V}\right) C_{n_{r_2}}$$

14

Correspondence of the Aeroballistic Derivatives with the Aerodynamic and Ballistic Nomenclatures

	Aeroballistic	Aerodynamic	Ballistic
Normal Force	$C_{N_{\vec{\alpha}}}$	$-C_{Y_\beta}, -C_{Z_\alpha}$	$K_N \dfrac{8}{\pi}$
Magnus Force	$C_{N_{p\vec{\alpha}}}$	$-C_{Y_{p\alpha}}, C_{Z_{p\beta}}$	$K_F \dfrac{16}{\pi}$
Pitching Moment	$C_{M_{\vec{\alpha}}}$	$C_{M_\alpha}, -C_{n_\beta}$	$K_M \dfrac{8}{\pi}$
Pitch Damping	$C_{M_{\vec{q}}}$	C_{M_q}, C_{n_r}	$-K_H \dfrac{16}{\pi}$
Magnus Moment	$C_{M_{p\vec{\alpha}}}$	$-C_{M_{p\beta}}, C_{n_{p\alpha}}$	$-K_T \dfrac{16}{\pi}$
Axial Force ($\alpha = 0$)	C_X	$-C_D$	$-K_D \dfrac{8}{\pi}$
Rolling Moment	C_{l_p}	C_{l_p}	$K_A \dfrac{16}{\pi}$

Angle of Attack Definitions

$$\alpha = \frac{w}{\sqrt{v^2 + w^2}} \cos^{-1} \frac{u}{V}$$

$$\beta = -\frac{v}{\sqrt{v^2 + w^2}} \cos^{-1} \frac{u}{V}$$

TWO-MOMENT EQUATIONS OF MOTION
FOR A ROLLING AND SPINNING BODY
AT LARGE ANGLE OF ATTACK

Coordinates, Axes, and Basic Equations of Motion. For analysis
of the motions of an axi-symmetric body with roll spin, it is convenient
to use a fixed-plane axis system as depicted in Figure 12, where the
x axis coincides with the missile axis of symmetry. In fixed-plane axes,
the y axis is initially horizontal, and the rotation of the coordinate system
with respect to the inertial reference frame is selected such that it stays
horizontal. This axis system is commonly used in aeroballistics (see, for
example, Reference 22).

An extremely important and useful characteristic of this axis system
is that it provides simple relationships between the fixed-plane angular rates
and the Euler angle rates, thus permitting a direct physical interpretation of
the solution. These relationships will be used repeatedly, and are presented
below for reference:

$$p = \dot{\Phi} - \dot{\psi} \sin \theta$$
$$q = \dot{\theta} \tag{1}$$
$$r = \dot{\psi} \cos \theta$$

where Φ = roll orientation of the body with respect to the fixed-plane
reference system.

For bodies having mass symmetry $(I_y = I_z = I)$, the fixed-plane equations of motion for rotation about the y and z axes are

$$M_y = I\ddot{\theta} + p r I_x + r^2 I \tan\theta \qquad (2)$$

$$M_z = I\dot{r} - p\dot{\theta} I_x - r\dot{\theta} I \tan\theta \qquad (3)$$

where M is the aerodynamic moment.

Due to the form of these equations, it is logical to select θ and r as the two basic variables for describing the motion.

Aerodynamic Considerations. At large angle of attack, the aerodynamic characteristics of a body cannot be accurately expressed in terms of the normal linear stability derivatives. A more accurate representation can be achieved by using a power or trigometric series expansion. However, a reasonably good approximation to the aerodynamic overturning moment and Magnus moment for small variations of angle of attack in the neighborhood of $\alpha = \pi/2$ radians can be obtained by letting

$$C(\vec{\alpha}) = \left[C(\vec{\alpha} = \frac{\pi}{2}) \right]\left[\sin\vec{\alpha} \right]$$

The approximation can be improved by adjustment of $C(\vec{\alpha} = \pi/2)$ once an initial determination of the steady-state value of $\vec{\alpha}$ has been accomplished.

To simplify the analysis, it is convenient to define the values of the overturning moment and Magnus moment coefficients at $\alpha = \pi/2$ radians

as $C_{M_{\pi/2}}$ and $C_{M_{p\pi/2}}$, respectively. In these definitions, we retain the aeroballistic nomenclature for determining the direction and sign of the moments. Thus the aerodynamic moment definitions used here will be consistent with the complete six-degrees-of-freedom equations.

To proceed, it is necessary to relate the vector angle of attack to the attitude variable, θ. Because only the rotational motion of the body is being considered, and we are restricting the motions to large angles of attack, it is convenient to specify the velocity in the direction of the Z inertial axis. Thus we obtain

$$\vec{a} = \pi/2 + \theta$$

and

$$\sin \vec{a} = \cos \theta$$

We can now express the aerodynamic moments M_y and M_z in terms of θ and r to obtain the following equations of motion:

$$\ddot{\theta} + p r \frac{I_x}{I} + r^2 \tan \theta = \left[\frac{q S d}{I}\right] \left[C_{M_{\pi/2}} \cos \theta + C_{M_q} \frac{\dot{\theta} d}{2V} + C_{M_{pr}} \frac{pd}{2V} \frac{rd}{2V}\right] \quad (4)$$

$$\dot{r} - p \dot{\theta} \frac{I_x}{I} - r \dot{\theta} \tan \theta = \left[\frac{q S d}{I}\right] \left[C_{n_r} \frac{rd}{2V} - C_{M_{p\pi/2}} \frac{pd}{2V} \cos \theta + C_{M_{z_0}}\right] \quad (5)$$

The yawing moment, $C_{M_{z_0}}$, has been added to account for geometric and aerodynamic asymmetry such as would exist when small flaps or strakes are placed on the body to produce a spin propelling moment. The derivatives C_{n_r} and $C_{M_{pr}}$ are described in Appendix I, but note that here we do not include the non-linearities of C_{n_r} with rd/2V and angle of attack.

The derivatives, C_{M_q}, $C_{M_{pr}}$, C_{n_r}, and $C_{M_{z_o}}$ are not aeroballistic, and must be interpreted here as fixed-plane derivatives. For example, $C_{M_{z_o}}$ is not in general a body-fixed moment. Only when $p = -\dot{\psi} \sin \theta$ can the body axes have the same roll orientation as the fixed-plane axes. Thus for Magnus-type spins with large roll rate, $C_{M_{z_o}}$ has no practical significance.

The derivatives C_{n_r} and C_{M_q} must also be distinguished because of the direction of the velocity vector. If the velocity vector had been placed along the X inertial axis, then C_{n_r} and C_{M_q} would be identical as in aeroballistic theory. However, in the present model the body is always at large angle of attack, and the effect of the q rotation on the aerodynamic cross force is completely different from the effect of the r rotation.

Likewise, $C_{M_{pr}}$ is meaningful only when the motion is at very large angle of attack.

Linearization of the Equations of Motion. The two non-linear differential equations of motion, equations (4) and (5), can be linearized by the use of the perturbation theory. We begin by assuming that the motion of θ and r can be represented by small deviations about operating points θ_o and r_o. This leads to the definitions

$$\theta = \theta_o + \Delta \theta$$

and $\hspace{11cm}$ (6)

$$r = r_o + \Delta r$$

For a particular case, θ_o and r_o are constant, so it follows that $\dot{\theta} = \Delta \dot{\theta}$, $\ddot{\theta} = \Delta \ddot{\theta}$, and $\dot{r} = \Delta \dot{r}$. It is also useful to introduce the

19

first-order approximations

$$\tan \theta = \tan \theta_o + \left(\sec^2 \theta_o\right)\left(\Delta\theta\right)$$

$$\cos \theta = \cos \theta_o - \left(\sin \theta_o\right)\left(\Delta\theta\right)$$

(7)

Substituting (6) and (7), neglecting second-order terms, and rearranging, the following two simultaneous linear differential equations are obtained in operator form, where the operator D denotes derivatives with respect to time:

$$\left[D^2 - KL\, C_{M_q} D + (r_o \sec \theta_o)^2 + K\, C_{M_{\pi/2}} \sin \theta_o \right] \Delta\theta$$

$$+ \left[2\, r_o \tan \theta_o + p\, \frac{I_x}{I} - KL^2\, C_{M_{pr}}\, p \right] \Delta r$$

(8)

$$+ \left(r_o \tan \theta_o + p\, \frac{I_x}{I} - KL^2\, C_{M_{pr}}\, p \right) r_o - K\, C_{M_{\pi/2}} \cos \theta_o = 0$$

$$\left[-\left(p\, \frac{I_x}{I} + r_o \tan \theta_o\right) D - (K L\, C_{M_{p\,\pi/2}}\, p \sin \theta_o \right] \Delta\theta$$

(9)

$$+ \left[D - K L\, C_{n_r}\right] \Delta r - K L\, C_{n_r}\, r_o + K L\, C_{M_{p\,\pi/2}}\, p \cos \theta_o - K\, C_{M_{z_o}} = 0$$

where $K = qSd/I$ and $L = d/2V$. Equations (8) and (9) are the basic two-degrees-of-freedom linearized equations of motion.

Steady-State Solutions. The steady-state solutions to equations (8) and (9) are obtained by letting $\Delta\theta = \Delta\dot{\theta} = \Delta\ddot{\theta} = \Delta r = \Delta\dot{r} = 0$ and solving for r_o and θ_o. We cannot obtain r_o and θ_o explicitly, but the following equations will be useful for an iterative solution. From equation (9), we obtain the result

$$r_{ss} = r_o = \frac{C_{M_{p\pi/2}}\, p\, \cos\theta_o}{C_{n_r}} - \frac{C_{M_{z_o}}}{L\, C_{n_r}} \tag{10}$$

which can be used directly for approximating r_o if θ_o is small. Substituting equation (10) into equation (8), we obtain the general implicit expression for θ_o as

$$\sin\theta_o \left[\left(\frac{C_{M_{p\pi/2}}\, p}{C_{n_r}}\right)^2 \cos\theta_o - \frac{2\, C_{M_{z_o}}\, C_{M_{p\pi/2}}\, p}{L\, C_{n_r}^2} - \left(\frac{C_{M_{z_o}}}{L\, C_{n_r}}\right)^2 \frac{1}{\cos\theta_o} \right]$$

$$+ p\, \frac{I_x}{I}\, \frac{C_{M_{p\pi/2}}\, p}{C_{n_r}}\, \cos\theta_o - \frac{KL^2\, C_{M_{pr}}\, p\, C_{M_{p\pi/2}}\, p\, \cos\theta_o}{C_{n_r}} \tag{11}$$

$$- \frac{C_{M_{z_o}}}{C_{n_r}}\, p\, \frac{I_x}{I} + \frac{KL\, C_{M_{pr}}\, p\, C_{M_{z_o}}}{C_{n_r}} - K\, C_{M_{\pi/2}}\, \cos\theta_o = 0$$

An iterative solution to θ_o can be obtained rapidly from equation (11) when θ_o is small, as it normally will be.

For the two types of spinning motion which are principally of interest (Magnus-type spins with large roll rate, or slowly rolling spins where the spin propelling moment is generated by a geometric asymmetry such as a

flap), we can reduce the complexity of the analysis by assuming

1)   for Magnus-type spins

$$C_{M_{z_O}} = 0$$

2)   for spins propelled by a body-fixed flap

$$p = - r \tan \theta, \quad C_{M_{p\pi/2}} = 0, \quad C_{M_{pr}} = 0$$

Using assumption (1), we obtain for Magnus-type spins the formulae

$$r_{ss} = r_o = \frac{C_{M_{p\pi/2}} \, p \cos \theta_o}{C_{n_r}} \tag{12}$$

$$\sin \theta_{ss} = \sin \theta_o = \frac{K \, C_{M_{\pi/2}} - p^2 \, \dfrac{C_{M_{p\pi/2}}}{C_{n_r}} \left[\dfrac{I_x}{I} - K L^2 \, C_{M_{pr}} \right]}{\left[\dfrac{C_{M_{p\pi/2}} \, p}{C_{n_r}} \right]^2} \tag{13}$$

Assumption (2) leads to the results

$$r_{ss} = r_o = \frac{C_{M_{z_O}}}{L \, C_{n_r}} \tag{14}$$

and

$$\sin \theta_{ss} = \sin \theta_o = - \frac{A}{2} + \sqrt{\left(\frac{A}{2} \right)^2 + 1} \tag{15}$$

where

$$A = \frac{\left(\dfrac{C_{M_{z_0}}}{L\, C_{n_r}}\right)^2 \left(1 - \dfrac{I_x}{I}\right)}{K\, C_{M_{\pi/2}}}$$

For very flat spins, we can let $\cos \theta = 1$ and obtain a very useful approximation, which is

$$\tan \theta_0 \approx \frac{1}{A} \tag{16}$$

Characteristic Equation. The third-order characteristic equation describing the two simultaneous linear differential equations, equations (8) and (9), is of the form $D^3 + AD^2 + BD + C = 0$. Expressed in terms of the basic variables, it becomes

$$
\begin{aligned}
D^3 &+ D^2 \left(- K L\, C_{M_q} - K L\, C_{n_r} \right) \\[2mm]
&+ D \left[\left(r_o \sec \theta_o \right)^2 + K\, C_{M_{\pi/2}} \sin \theta_o + (K L)^2 C_{n_r}\, C_{M_q} \right.\\[2mm]
&\left. + 2 \tan \theta_o\, r_o \left(p\, \frac{I_x}{I} + r_o \tan \theta_o \right) + p\, \frac{I_x}{I} \left(p\, \frac{I_x}{I} + r_o \tan \theta_o \right) \right. \\[2mm]
&\left. - K L^2\, C_{M_{pr}}\, p \left(p\, \frac{I_x}{I} + r_o \tan \theta_o \right) \right. \\[2mm]
&\left. + \left[- \left(r_o \sec \theta_o \right)^2 K L\, C_{n_r} - K^2 L\, C_{M_{\pi/2}}\, C_{n_r} \sin \theta_o \right.\right. \\[2mm]
&\left.\left. + \left(2\, r_o \tan \theta_o + p\, \frac{I_x}{I} - K L^2\, C_{M_{pr}}\, p \right)\left(K L\, C_{M_{p\,\pi/2}}\, p \sin \theta_o \right) \right] \right] = 0
\end{aligned}
\tag{17}
$$

23

<u>Stability</u>. It is of interest to know under what conditions the system as given by equation (17) is stable. The fundamental problem in ascertaining system stability is one of determining the nature of the roots of the characteristic equation, in particular, the behavior of the system in the neighborhood of steady state. Since the region of stability, rather than the exact values of the roots, are of greatest interest, the Routh criterion can be employed.

The Routh criterion permits the definition of boundaries between stability and instability. In addition, the boundaries can be established for both the real roots and the real part of the complex roots. For a third-degree equation, we have the rules:

1) If only C changes from $+$ to $-$, then one real root changes from negative to positive, indicating the inception of static instability.

2) If only $AB - C$ changes from $+$ to $-$, then the real part of one complex pair of roots changes from négative to positive, indicating the inception of dynamic or oscillatory instability.

The static stability of the Magnus-type spins at steady-state can be examined by substituting the expressions for r_o and θ_o, equations (12) and (13), into the C coefficient of equation (17). We obtain after considerable algebraic manipulation

$$C = \frac{K L \, C_{M_p \pi/2}^2 \, p^2}{C_{n_r}} \left\{ \left[\frac{K \, C_{M_{\pi/2}} - p^2 \frac{C_{M_p \pi/2}}{C_{n_r}} \left(\frac{I_x}{I} - K L^2 \, C_{M_{pr}} \right)}{\left(\frac{C_{M_p \pi/2} \, p}{C_{n_r}} \right)^2} \right]^2 - 1 \right\}$$

(18)

where it will be noted that the term in $\begin{bmatrix} \end{bmatrix}$ is $\sin \theta_o$. Equating C to zero, we can therefore find stability boundaries for any pair of variables appearing in equation (18). We will show one interesting case as an example. If we let $C_{M_{\pi/2}}$, the overturning moment at $\alpha = \pi/2$, equal zero, we can obtain the boundary equation

$$C_{M_p \pi/2} = -C_{n_r} \left[\frac{I_x}{I} - KL^2 C_{M_{pr}} \right] \tag{19}$$

For C_{n_r} negative, it follows from equation (18) that

$$\left| C_{M_p \pi/2} \right| > \left| C_{n_r} \left(\frac{I_x}{I} - KL^2 C_{M_{pr}} \right) \right|$$

on the stable side of the boundary. Thus, there is a minimum Magnus moment for a statically stable spin.

The dynamic stability boundary $AB - C = 0$ for Magnus-type spins in the neighborhood of θ_o and r_o is determined in the same manner as above by substitution of equations (12) and (13) into the appropriate coefficients of the characteristic equations. The following boundary equation is then obtained:

$$AB - C = -KL(C_{M_q} + C_{n_r}) \left\{ \left[\frac{C_{M_p\pi/2} \, P}{C_{n_r}} \right]^2 + (KL)^2 C_{n_r} C_{M_q} + \left(p \frac{I_x}{I} \right)^2 \right.$$

$$-KL^2 C_{M_{pr}} \, p \frac{I_x}{I} + \sin\theta_o \left[K C_{M_{\pi/2}} + \frac{C_{M_p\pi/2} \, P}{C_{n_r}} \left(3p \frac{I_x}{I} - KL^2 C_{M_{pr}} \right) \right]$$

$$\left. + 2 \left(\frac{C_{M_p\pi/2} \, P}{C_{n_r}} \right)^2 \sin^2 \theta_o \right\} - KL \left(\frac{C_{M_p\pi/2}^2 \, p^2}{C_{n_r}} \right) \left(\sin^2 \theta_o - 1 \right) = 0$$

where $\sin \theta_o$ is given by equation (13). $\tag{20}$

25

Specific boundaries in terms of the aerodynamic variables can be obtained from equation (20) by numerical analysis.

For the non-Magnus spins described previously, we obtain a useful form of the static stability boundary for flat spins by letting $\sin \theta = \tan \theta$ and $\cos \theta = 1$, and by substituting the steady-state solutions as given by equations (14) and (16) into the coefficient C of the characteristic equation. We then obtain

$$C = -C_{n_r} \left\{ K L \left(\frac{C_{M_{z_0}}}{L C_{n_r}} \right)^2 + K^3 L \left(\frac{L C_{n_r}}{C M_{z_0}} \right)^2 \frac{\left| C_{M_{\pi/2}} \right|}{\left(1 - \frac{I_x}{I} \right)} \right\} \tag{21}$$

Thus this type of spin is statically stable (i.e., $C > 0$) as long as $C_{n_r} < 0$ and $1 - \frac{I_x}{I} > 0$.

The dynamic stability criteria for the non-Magnus spins with the same assumptions as above are given by

$$AB - C = -K L \left(C_{M_q} + C_{n_r} \right) \left\{ \left(\frac{C_{M_{z_0}}}{L C_{n_r}} \right)^2 + \left(\frac{K L C_{M_{\pi/2}} C_{n_r}}{C M_{z_0}} \right)^2 \frac{1}{\left(1 - \frac{I_x}{I} \right)} \right. $$

$$\left. + K L^2 C_{n_r} C_{M_q} + \left(1 - \frac{I_x}{I} \right) \left(2 - \frac{I_x}{I} \right) p^2 \right\} \tag{22}$$

$$+ C_{n_r} \left[\left(\frac{C_{M_{z_0}}}{L C_{n_r}} \right)^2 K L + K^3 L \left(\frac{L C_{M_{\pi/2}} C_{n_r}}{C M_{z_0}} \right)^2 \frac{1}{\left(1 - \frac{I_x}{I} \right)} \right]$$

Again, it is unnecessary to determine the dynamic stability boundary because it can be seen that sufficient conditions for stability, i.e., $AB - C > 0$, are $C_{n_r} < 0$, $C_{M_q} < 0$, and $(1 - I_x/I) > 0$.

Approximate Roots of the Characteristic Equation. By making certain assumptions about the coefficients of the characteristic equation, some simplifications may be made for the determination of the roots of the characteristic polynomial. First, it is assumed that θ_o will be small, and the contributions of the terms containing θ_o are negligible. In this analysis, we also neglect the effect of $C_{M_{pr}}$. We thus obtain, approximately, the following analytic expressions for the coefficients

$$A = - K L C_{M_q} - K L C_{n_r}$$

$$B = (K L)^2 C_{M_q} C_{n_r} + \left(p \frac{I_x}{I} \right)^2 + r^2$$

$$C = - K L C_{n_r} r^2$$

where $r \approx \dfrac{C_{M_p \pi/2} P}{C_{n_r}}$. Since $K L$ and I_x/I are very small, then if r is large, we have

$$r^2 >> (K L)^2 C_{M_q} C_{n_r} + p^2 \left(\frac{I_x}{I} \right)^2$$

27

With the above assumptions, the characteristic polynomial becomes

$$\lambda^3 - (K L C_{M_q} + K L C_{n_r}) \lambda^2 + r^2 \lambda - K L C_{n_r} r^2 = 0$$

To determine the roots of the above cubic, let

$$\lambda_1 \approx - \frac{C}{B} = \frac{K L C_{n_r} r^2}{r^2} = K L C_{n_r}$$

This approximates the real root. Factoring $(\lambda - K L C_{n_r})$ from the cubic gives the quadratic

$$\lambda^2 - K L C_{M_q} \lambda + r^2 + \text{remainder}$$

The remainder is $- (K L)^2 C_{M_q} C_{n_r} \lambda$, which we shall assume to be negligible since $(K L)$ is a small number. The characteristic polynomial is now

$$(\lambda - K L C_{n_r}) (\lambda^2 - K L C_{M_q} \lambda + r^2) = 0$$

and the roots are

$$\lambda_1 = K L C_{n_r} \tag{23}$$

$$\lambda_{2,3} = \frac{K L C_{M_q}}{2} \pm \sqrt{(K L C_{M_q})^2 - 4 r^2} \tag{24}$$

For $C_{n_r} < 0$, $C_{M_q} < 0$, and $\dfrac{K L C_{M_q}}{2} < r$, $\lambda_{2,3}$ will be complex.

If in addition, $\dfrac{K L C_{M_q}}{2} << r$, the complex roots are

$$\lambda_{2,3} = -\frac{K L C_{M_q}}{2} \pm i r \tag{25}$$

and the angular frequency is the yaw rate.